Hadron Showers in a Highly Granular Calorimeter

by

Benjamin Lutz

Hadron Showers in a Highly Granular Calorimeter

Dissertation

zur Erlangung des Doktorgrades
des Department Physik
der Universität Hamburg

vorgelegt von

Benjamin Lutz

aus Regensburg

Hamburg
2010

Gutachter der Dissertation:	Prof. Dr. Rolf-Dieter Heuer Jun.-Prof. Dr. Johannes Haller
Gutachter der Disputation:	Jun.-Prof. Dr. Johannes Haller Prof Dr. Peter Schleper
Datum der Disputation:	31.08.2010
Vorsitzender des Prüfungsausschusses:	Dr. Georg Steinbrück
Vorsitzender des Promotionsausschusses:	Prof. Dr. Joachim Bartels
Dekan der MIN Fakultät:	Prof. Dr. Heinrich Graener
Leiterin des Department Physik:	Prof. Dr. Daniela Pfannkuche

Abstract

A future electron-positron collider like the planned International Linear Collider (ILC) needs excellent detectors to exploit the full physics potential. Different detector concepts have been evaluated for the ILC and two concepts based on the particle-flow approach were validated. To make particle-flow work, a new type of imaging calorimeters is necessary in combination with a high performance tracking system, to be able to track the single particles through the full detector system. These calorimeters require an unprecedented level of both longitudinal and lateral granularity. Several calorimeter technologies promise to reach the required readout segmentation and are currently studied. This thesis addresses one of these: The analogue hadron calorimeter technology. It combines work on the technological aspects of a highly granular calorimeter with the study of hadron shower physics.

The analogue hadron calorimeter technology joins a classical scintillator-steel sandwich design with a modern photo sensor technology, the silicon photomultiplier (SiPM). The SiPM is a millimetre sized, magnetic field insensitive, and low cost photo-sensor, that opens new possibilities in calorimeter design. This thesis outlines the working principle and characteristics of these devices. The requirements for an application specific integrated circuit (ASIC) to read the SiPM are discussed; the performance of a prototype chip for SiPM readout, the SPIROC, is quantified. Also the SiPM specific reconstruction of a multi-thousand channel prototype calorimeter, the CALICE AHCAL, is explained; the systematic uncertainty of the calibration method is derived.

The AHCAL does not only offer a test of the calorimeter technology, it also allows to record hadron showers with an unprecedented level of details. Test-beam measurements have been performed with the AHCAL and provide a unique sample for the development of novel analysis techniques and the validation of hadron shower simulations. A method to identify the position of the first hard interaction in hadron showers is developed in this work. It is applied to measure hadron shower profiles without the fluctuations in the position of the first hard interaction and to estimate and correct for longitudinal leakage.

Finally, different hadron simulation models are confronted with the measured data. The Geant4 based simulation of the test-beam is explained; the detector modelling and the systematic error assumptions are verified with electromagnetic showers. The studies comprise thirteen different Geant4 physics lists and six different hadron shower models. Both the description of the spatial shower development and the modelling of the detector response and the resolution are tested.

Zusammenfassung

Um das Physikpotential eines Elektron-Positron-Beschleunigers wie des Internationalen Linear Beschleunigers (ILC) auszuschöpfen, werden exzellente Detektoren benötigt. Es wurden verschiedene Detektorkonzepte für den Einsatz am ILC evaluiert, von denen zwei auf dem "Particle-Flow"-Ansatz aufbauende angenommen wurden. Der "Particle-Flow"-Ansatz basiert darauf, die Spur einzelner Teilchen durch den gesamten Detektor verfolgen zu können. Hierfür benötigt man neben einem hochperformanten Spurdetektor eine neue Klasse von Kalorimetern, welche sich durch eine besonders feine Unterteilung der Auslesesegmente, sowohl in Längs- als auch Querrichtung, auszeichnen. Momentan werden verschiedene Technologien getestet, die eine entsprechende Segmentierung erreichen können. Diese Arbeit beschäftigt sich mit der analogen hadronischen Kalorimetertechnologie. Dabei werden nicht nur die technologischen Aspekte fein segmentierter Kalorimeter betrachtet, sondern auch die Physik von Hadronschauern untersucht.
Die analoge hadronische Kalorimetertechnologie verbindet ein klassisches Stahl-Szintillator-Schaschlikkalorimeter mit einem modernen Photosensor, dem Siliziumphotomultiplier (SiPM). Der SiPM ist ein millimetergroßer, magnetfeldunempfindlicher und kostengünstiger Sensor, der neuartige Kalorimeterdesigns erlaubt. In dieser Arbeit werden das Arbeitsprinzip und die Betriebseigenschaften der SiPMs dargestellt. Die Anforderungen an eine integrierte Ausleseelektronik (ASIC) werden diskutiert, und der Prototyp eines neuen Auslesechips für SiPMs (SPIROC) wird vermessen. Außerdem wird die SiPM-spezifische Rekonstruktion anhand eines Prototypkalorimeters mit mehreren tausend Auslesekanälen, dem CALICE AHCAL, erklärt. Zusätzlich wird die systematische Unsicherheit der Detektorkalibration hergeleitet.
Das AHCAL dient nicht nur dem Test der Technologie, sondern bietet auch die Möglichkeit die Struktur von Hadronschauern mit bisher unerreichter Genauigkeit zu messen. Die mit dem AHCAL durchgeführten Teststrahlmessungen stellen eine einzigartige Datenquelle für die Entwicklung neuer Analysemethoden und die Überprüfung verschiedener Hadronschauersimulationen dar. Im Rahmen dieser Arbeit wird eine Methode zur Bestimmung des Ortes der ersten harten Wechselwirkung in Hadronschauern entwickelt. Mit Hilfe dieser Methode werden Schauerprofile ohne die Fluktuation in der Position der ersten Wechselwirkung gemessen. Zusätzlich wird die Positionsinformation genutzt, um den Energieverlust aufgrund der begrenzten Detektortiefe abzuschätzen und zu korrigieren.
Die Ergebnisse der Hadronschauerstudien werden benutzt um die Vorhersagen verschiedener Simulationsmodelle zu testen. Dazu wird die Geant4 basierte Simulation des Teststrahls und die Modellierung des Detektors eingeführt. Um die Aussagekraft des Vergleichs zu überprüfen, werden die Detektorsimulation und die Annahmen zu den Rekonstruktionsunsicherheiten mit elektromagnetischen Schauern überprüft. Die Studien umfassen dreizehn verschiedene Geant4 Physiklisten die sechs unterschiedliche Hadronschauermodelle kombinieren. Die Vorhersagen von Schauerform, Detektorsignal und Detektorauflösung werden mit den Teststrahlmessungen verglichen.

Contents

Introduction

Mankind's picture of the physical composition of the world – and the universe – has changed radically already several times in history. For example, scientists believed that matter consists of indivisible atoms: until 1897. Then, J. J. Thomson found that cathode rays behave like particles with charge. He characterised this new particle, the electron, with the help of electric and magnetic fields, and was awarded the Nobel Prize for this work [1]. He also concluded that these particles have to come from inside the atoms. Consequently, the atoms have to be composed objects. He pictured the atom as a plum pudding with raisins, the simplest model he could imagine. With E. Rutherford's discovery of the α-particle, new experiments became possible. Thomson's picture broke down with Rutherford's explanation for the result of scattering experiments with α-particles on heavy atoms [2]. He showed that the atomic model needs to include a positively charged, heavy core.

Since the times of Thomson and Rutherford, many more particles have been discovered. Some of the experimentally observed particles came as a surprise, like the muon, which was commented by I. I. Rabi with: "Who ordered that?". Other particles, like the positron, were already expected by theoretical considerations before their experimental observation. Experimental particle physics made a big step with the development of accelerators. These quickly extended the accessible energy range and more and more particles were observed. A study of the generation and decay processes of these particles revealed several conservation laws. And finally, the observed conservation laws inspired a new theory of particles and their interactions: the Standard Model of particle physics.

Within the Standard Model, matter consists of elementary and fermionic particles: leptons and quarks. The interactions between the matter particles are mediated by bosonic force carriers which can describe the strong, the weak, and the electromagnetic force. Figure 1 gives an overview of the Standard Model particles. All particles of the Standard Model, except the Higgs boson, have been experimentally observed. The predictive power of this model is outstanding, and no significant discrepancies between the collision experiments and the model have been observed so far.

The Standard Model is mathematically formulated by a relativistic quantum field theory with local gauge invariance. The local gauge invariance directly gives the terms of the bosonic force carriers. It is necessary that all particles are massless to make this formalism work. However, the experimentally observed particles are not massless. To satisfy the principle of local gauge invariance, the Standard Model postulates the Higgs boson, which generates the particle masses via its coupling.

Despite of its great success, the Standard Model cannot be the theory of everything. Cosmological observations show, that matter described by the Standard Model sums up to about 5 % of the total energy content of the universe. Approximately one quarter of

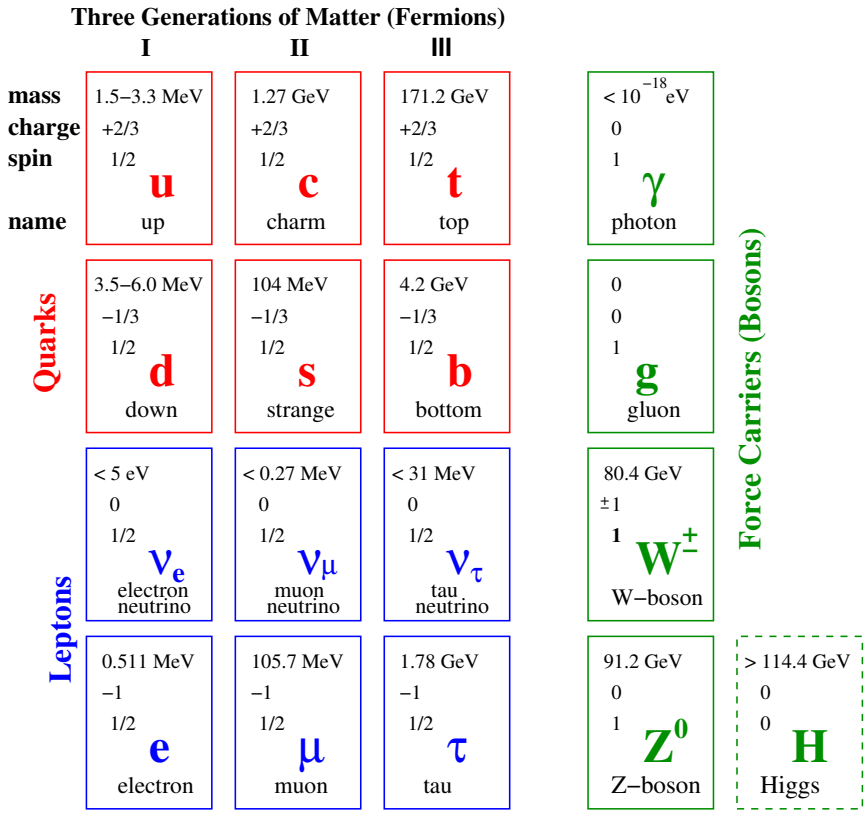

Figure 1: Particles and force carriers of the Standard Model of particle physics [3, 4].

the universe consists of dark matter, that does not follow the rules of the Standard Model. The remaining energy of the universe is attributed to dark energy [5].

With the recent startup of the Large Hadron Collider (LHC), experimental particle physics has started to explore new energy regions. Previous measurements show, that the Standard Model Higgs should be within the energy reach of the LHC, if it exists. Also popular extensions of the Standard Model like supersymmetry are likely to show evidence at the LHC. There are chances that the understanding of the world and universe is close to another big step. But whatever will be observed at the LHC, the precision of the measurements at a hadron collider is intrinsically limited due to the fact that the colliding particles are not elementary. Which of the constituents of the colliding protons, quarks or gluons, will interact is beyond the control of the experimenter.

An electron-positron collider would allow collisions with well defined initial states. The usage of elementary particles gives the experimenter control over the precise energy and the spin orientation of the colliding particles. Technologically, an electron-positron collider which exceeds previously reached energies has to be constructed as a linear accelerator. The energy of ring accelerators is limited by synchrotron radiation due to the small mass of the particles. The challenge of such a machine is the accelerating technology. The most advanced project is the proposed International Linear Collider (ILC).

To fully exploit the potential of an electron-positron collider, the detector system has to be capable of detecting the complete event structure and record particle and jet energies with great precision. Different detector technologies have been evaluated for the ILC

and two detector concepts based on the particle flow approach have been validated. The International Large Detector (ILD) is one of these detector concepts combining a high resolution tracking system with a highly granular calorimetric system. This work focuses on the analogue hadron calorimeter option suggested within this concept.

Most ILC particle flow calorimeters are developed within the CALICE[1] collaboration. Since 2006, a prototype calorimeter, the AHCAL[2], exists to test the technology and performance for a scintillator based hadron calorimeter with silicon photomultiplier (SiPM) readout. The prototype has been tested in several test-beam campaigns at CERN and Fermilab. The recorded data serve not only as test of the calorimeter, but also to validate the predictions of hadron shower simulation models.

Parallel to the tests with the AHCAL prototype, the analogue hadron technology is developed further. One of the key issues is the integration of the readout electronics into the detector. This is necessary to minimise the gaps and dead material in the detector which would be necessary with an external readout system. A microchip including a full readout chain is currently developed to achieve this objective.

This work addresses both the AHCAL detector technology and the study of hadron shower physics. The technological part includes the characterisation of the basic readout performance of the first prototype of the new microchip. Also, the calibration of the current AHCAL prototype is explained and limits for the systematic uncertainties are derived. The analysis of hadronic showers utilises the high spatial granularity of the calorimeter. For example, a method to identify the first hard interaction is developed. This method allows to recover energy lost due to longitudinal leakage and improves the calorimeter resolution. It also makes it possible to record shower profiles without the fluctuations in the first interaction. The results from the hadron studies are compared to different hadron shower simulation models to evaluate the performance of the models.

This text is structured in four main parts. First, there is a more general introduction to the International Linear Collider and the International Large Detector concept (chapter 1), the basics of calorimetry (chapter 2), and the working principle of the new photo-sensor technology (chapter 3). The general part is followed by a description of more specific topics: the AHCAL prototype (chapter 4), the CERN test-beam (chapter 5), and the simulation of the test-beam experiment (chapter 6). The third part describes and discusses the measurements of hadron showers with the AHCAL at the CERN test-beam. It comprises the event selection (chapter 7), the analysis methods (chapter 8), and the comparison of the measurements to different simulation models (chapter 9). The last part deals with the test of the next generation readout chip. It includes a description of the SPIROC[3] (chapter 10), the test-bench setup (chapter 11), and a discussion of the analogue performance of the chip (chapter 12).

[1] CALICE stands for Calorimetry at Linear Collider Experiments
[2] AHCAL stands for analogue hadronic calorimeter
[3] SPIROC stands for SiPM Integrated Readout Chip

Chapter 1

ILC and ILD

Today's most powerful particle accelerator is the Large Hadron Collider (LHC) at CERN[1]. It is designed to collide two proton beams with energies up to 7 TeV per beam and is currently taking its first data at half the design energy. The LHC is a ring accelerator that keeps the particles on a closed orbit and adds the energy consecutively with each revolution. To reach such high energies in a ring design, it is necessary to use heavy particles. For light particles like electrons, the synchrotron radiation limits the reachable energy. The power of the synchrotron radiation scales with radius R, particle mass m, and particle energy E like

$$P_{\text{sync}} \propto \frac{E^4}{R \cdot m^4}. \tag{1.1}$$

The Large Electron-Positron Collider (LEP) which was located in the same tunnel the LHC uses nowadays is most probably the highest energetic ring accelerator for electron-positron collisions ever built, due to these limitations.

But, the usage of leptons has several advantages over the usage of hadrons in collision experiments. Leptons are elementary particles in contrast to hadrons which consist of quarks and gluons. While in hadron collisions the type of the initial interaction and its energy is unknown, leptons can be collided with well defined energy and spin orientation. The heavier leptons, the muon and tau, are unstable particles and cannot be stored for sufficiently long times to efficiently operate a ring accelerator. All in all, a linear electron-positron collider is the only promising way to study lepton collisions with energies comparable to the LHC energies.

The main challenge in building a linear accelerator is the actual accelerating technology. To keep the length of the accelerator within reasonable bounds high acceleration gradients have to be realised. At the same time the machine has to transport the beam particles with high precision to keep the beam quality during the acceleration process.

1.1 The International Linear Collider

The most advanced concept for a linear electron-positron collider is the International Linear Collider (ILC). Figure 1.1 sketches the layout of the ILC as defined in the reference design

[1] CERN is the European Organization for Nuclear Research located near Geneva in Switzerland and France.

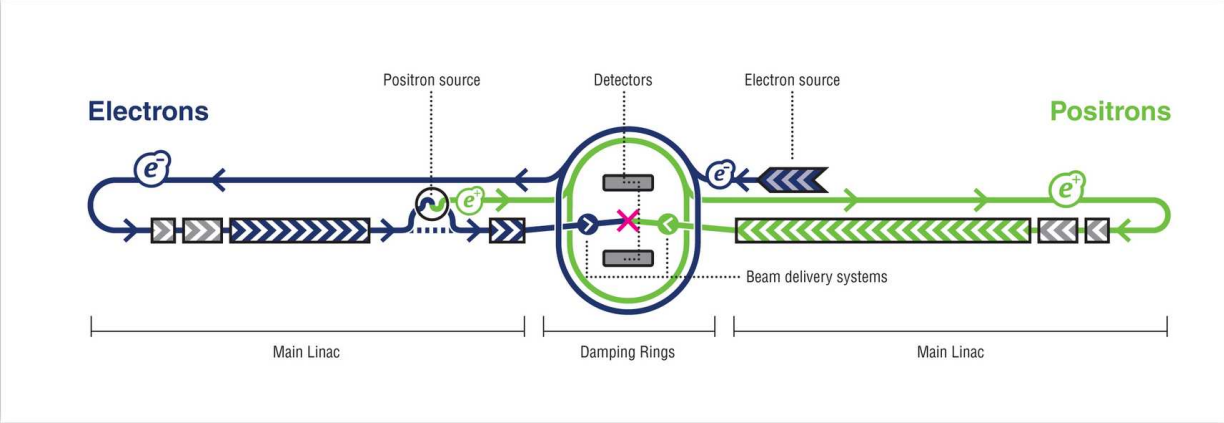

Figure 1.1: Schematic layout of the International Linear Collider as defined in the reference design report [6].

report [6] from the year 2007. As many parts of the accelerator technology are still actively developed, the design is subject to changes and re-optimisation. The technical design report which will fix the machine parameters is expected for 2012.

Polarised electrons are generated by laser light in the electron source and are accelerated to 5 GeV. This acceleration happens in three steps: direct current (DC) acceleration inside the particle gun to approximately 150 keV, radio frequency (RF) acceleration to 76 MeV in normal-conducting structures, and RF acceleration to 5 GeV in super-conducting structures. The electron beam obtains its bunch structure during the first RF acceleration.

The electrons from the source are collected in the electron damping ring to build a full ILC bunch train. The damping rings are operated at 5 GeV and with superconducting RF acceleration. To achieve a fast damping of the incoming beam jitter and the necessary reduction in beam emittance, the damping ring uses superconducting wigglers to induce synchrotron radiation.

The electrons are transported from the damping ring via the Ring To Main Linac (RTML) to the start of the main accelerator. This system also removes most of the beam halo, compresses the bunch length, and allows to adjust the orientation of the beam polarisation. During the bunch compression the electron energy is raised to 15 GeV.

In the main linac the electrons are accelerated to their final collision energy. The linac utilises superconducting niobium cavities operated with 1.3 GHz RF to reach an average accelerating gradient of 31.5 MeV/m.

The positrons are generated in photo-production. The main electron beam is sent through a helical undulator and generates circular polarised photons. These photons are sent to a titanium alloy target where they generate electromagnetic showers. The shower particles are captured and accelerated to 125 MeV in a first step. Afterwards, the shower electrons and the remaining photons are separated and dumped. The positrons are accelerated in two steps to 5 GeV and injected to the positron damping ring. The remaining acceleration process is similar to the electron acceleration.

The two accelerated beams are brought into collision with the beam delivery system (BDS). It focuses the beams to the small sizes necessary to achieve the desired luminosity,

monitors beam properties like energy and polarisation, and disposes the spent beam into the beam dumps. There is only one collision region foreseen, which has to be shared by the two detectors in a push pull configuration. The design allows to do maintenance work on the one detector, while the other is taking data.

The total system is capable of delivering beams with centre of mass energy $\sqrt{s}$ from 200 GeV up to 500 GeV. The design allows a later upgrade to 1 TeV energy and a running at 90 GeV, the Z-boson mass. The peak luminosity is $2{\cdot}10^{34}\,\mathrm{cm}^{-2}\mathrm{s}^{-1}$ and allows to collect an integrated luminosity of $500\,\mathrm{fb}^{-1}$ within the first four years of operation.

1.2 The International Large Detector

Detectors have to reach an excellent performance to fully exploit the physics potential of the ILC. The International Large Detector (ILD) is one suggested detector concept for the ILC. It emerged from the fusion of the LDC [7] and the GLD [8] detector concepts and has been validated as one of two concepts by the International Advisory Group (IDAG) in August 2009 [9]. To achieve the desired performance, a design is chosen that allows to track the individual particles of hadronic jets through the detector, and to use the sub-detector with the best performance to measure the four-momentum of the particles. This so-called particle-flow-approach requires an excellent spatial resolution of all sub-detectors.

Using particle-flow, the detector jet energy resolution σ_{jet} is given by:

$$\sigma_{\mathrm{jet}} = f_{\mathrm{ch}} \cdot \sigma_{\mathrm{tracker}} \oplus f_{\gamma} \cdot \sigma_{\mathrm{ECAL}} \oplus f_{\mathrm{h^0}} \cdot \sigma_{\mathrm{HCAL}} \oplus \sigma_{\mathrm{conf}}. \tag{1.2}$$

For a typical jet, the fraction f_{ch} of energy carried by charged particles is 60 %, the energy fraction of photons f_{γ} is 30 % , and neutral hadrons contribute with $f_{\mathrm{h^0}}$ equal to 10 %. With particle-flow, most of the jet energy is measured with the trackers that have a superior energy resolution $\sigma_{\mathrm{tracker}}$ compared to the resolution of the electromagnetic calorimeter σ_{ECAL} and to the resolution of the hadronic calorimeter σ_{HCAL}. As the method depends on the topological separation of the different particles, errors in the matching of tracker and calorimeter information can deteriorate the resolution which is reflected in the confusion term σ_{conf}.

Figure 1.2 depicts the layout of the ILD. The main tracking device is a large volume time projection chamber (TPC). A silicon pixel vertex (VTX) detector allows to efficiently tag long lived b- and c-hadrons. It is followed by a silicon strip detector which shortens the gap between VTX and TPC. Between the TPC and the calorimeters an additional silicon strip detector adds a high precision space point.

The calorimeter system consists of highly segmented sampling calorimeters. The electromagnetic calorimeter (ECAL) uses a tungsten absorber and silicon PIN-diodes with square size of $0.5{\times}0.5\,\mathrm{cm}^2$ for readout. Longitudinally, it is segmented into 30 readout planes which are grouped in three sets with different sampling ratios. An alternative readout concept with scintillator strips exists. In this case, novel silicon based photomultipliers detect the scintillation light and allow the necessary compact design. The hadron calorimeter (HCAL) uses a steel absorber. Is is longitudinally segmentation in up to 48 layers. Different readout options are currently studied: analogue, digital, and semi-digital. The analogue technology uses scintillator tiles of $3{\times}3\,\mathrm{cm}^2$ as active material which are read with

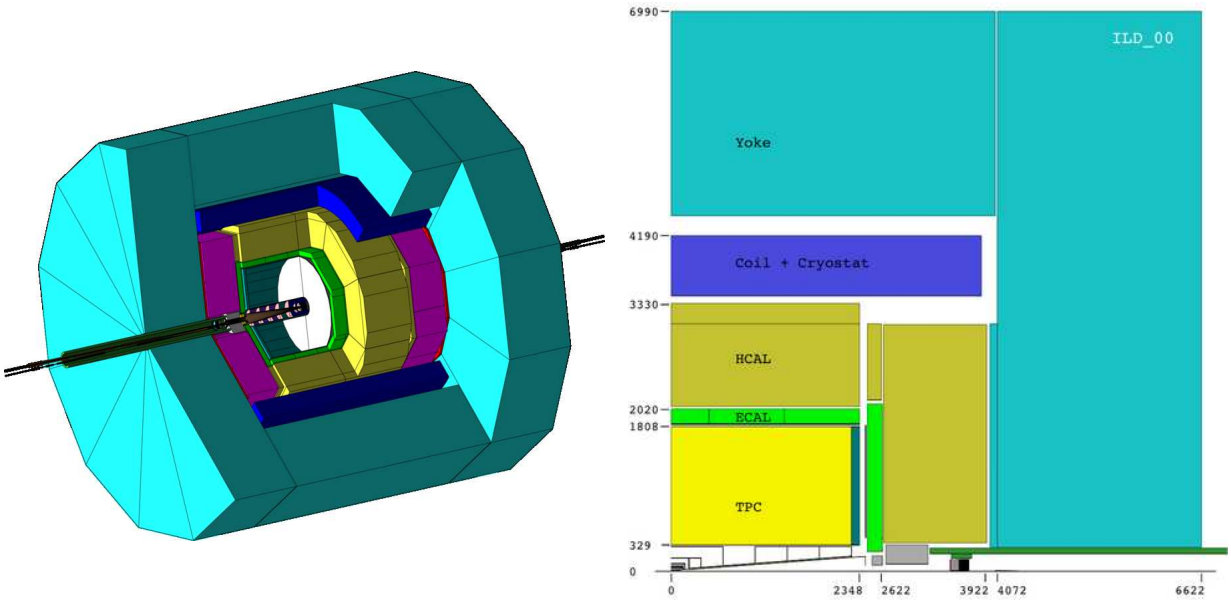

(a) (b)

Figure 1.2: (a) ILD detector model as implemented in the simulation software Mokka. All sizes are in mm. (b) Cross section through one quadrant of the ILD. Pictures are taken from [10].

silicon based photomultipliers. The digital and semi-digital variants use gaseous detectors and a lateral segmentation of $1\times1\,\mathrm{cm}^2$. The calorimeter concepts and readout technologies are studied within the CALICE collaboration. The studies with the analogue hadron calorimeter option are the main subject of this work.

The trackers and calorimeters are located inside a superconducting coil with a magnetic field of 3.5 T. The magnetic flux is returned within an iron yoke. The yoke is instrumented to detect and track muons, and to act as a tail catcher for the calorimeter system. Two options are considered for the readout technology: Scintillator strips and resistive plate chambers (RPC).

A system of three radiation hard calorimetric detectors extend the detector acceptance to very low angles: LumiCAL, BCAL, and LHCAL. These detectors also monitor the luminosity and the quality of the beam.

The decision for a single beam line with a push-pull operation emerged in the optimisation process of the ILC. The initial detector concept did not foresee this option and the necessary technical adaption of the detector is still ongoing. Currently, the following design is favoured: The complete ILD, including the final focus elements of the beam-line, will be placed on a large concrete plate which can be moved in and out of the beam line. As the detector is self shielding, no further radiation shielding is needed in addition to the separation wall between the two detectors. Other requirements like magnetic shielding are currently investigated.

The other validated concept, SiD, has similar ECAL and almost the same HCAL options, but uses a silicon based main tracker [11].

Chapter 2

Calorimetry

Calorimeters are devices to measure the energy of high energetic particles. Unlike trackers, calorimeters do not try to preserve the original particles. In contrary, most calorimeters measure the energy by observing the disintegration products of a particle stopped in a volume of matter. A multitude of different calorimeter technologies exists, but all base on the principle that the energy of the incoming particle is used up in generating a detectable signal. The processes inside a calorimeter always underlie statistical fluctuations. Therefore, the energy resolution of a calorimeter gets better the more signal quanta per energy are generated. This chapter will discuss the case of a hadronic sampling calorimeter and the relevant interactions of particles and matter.

2.1 Interaction of Particles with Matter

The interactions a particle can undergo in matter depend on the particle type. For example, neutrinos being leptons and having no charge can only interact by the weak force. But, the cross sections of weak processes are too small to efficiently use it as signal in calorimetry. Charged particles are the main source of the detectable signal in calorimeters. Therefore, the electromagnetic interaction will be described before the strong interactions, that are relevant for hadron calorimetry, will be introduced.

2.1.1 Electromagnetic Interactions in Matter

Charged particles traversing matter interact electromagnetically with the charged constituents of the matter atoms. Depending on the particle momentum, different processes are dominant. Figure 2.1 illustrates the average energy loss of positively charged muons in copper. Above the critical energy $E_{\mu c}$ of muons, radiative processes dominate and the particle energy is reduced by radiation of photons. Below the critical energy, the particle energy is mainly transferred to the electrons of the atoms and the atoms get ionised. The mean ionisation energy loss is described over a large momentum range by the "Bethe-Bloch" equation:

$$-\left\langle \frac{\mathrm{d}E}{\mathrm{d}x} \right\rangle = K \cdot z^2 \cdot \frac{Z}{A} \cdot \frac{1}{\beta^2} \left[\frac{1}{2} \ln \frac{2 m_\mathrm{e} c^2 \beta^2 \gamma^2 T_\mathrm{max}}{I^2} - \beta^2 - \frac{\delta(\beta\gamma)}{2} \right]. \tag{2.1}$$

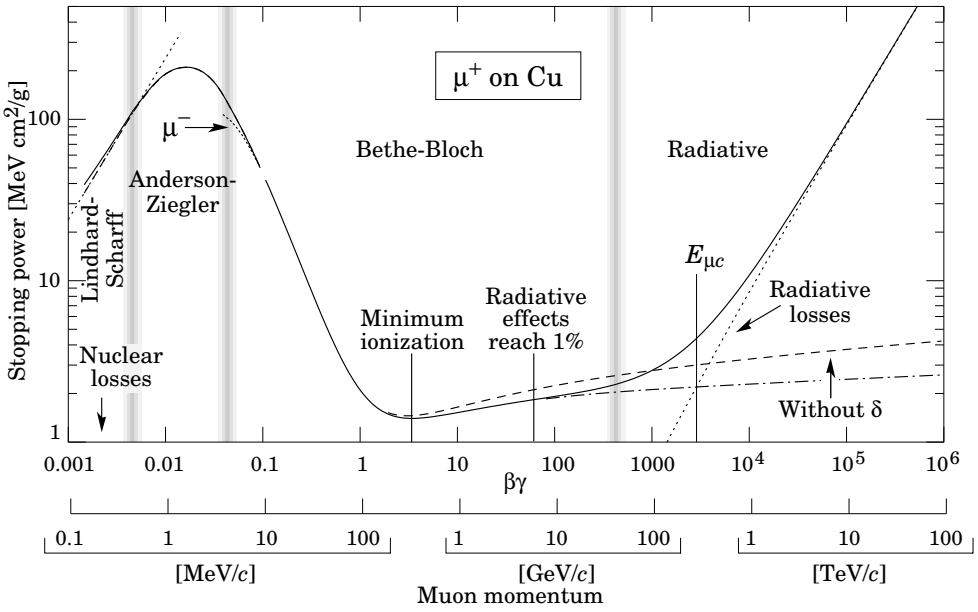

Figure 2.1: Stopping power $\langle \mathrm{d}E/\mathrm{d}x \rangle$ for positively charged muons in copper. The stopping power is plotted as a function of the particle velocity $\beta\gamma = p/Mc$. The regimes of different theoretical models are marked with horizontal bars. The picture is taken from [3].

In this regime the mean energy loss depends quadratically on the charge z of the particle and linearly on the ratio of the atomic number Z over the atomic mass A of the material. It further depends on the velocity β of the particle, the ionisation energy I of the material, and the maximal transferable kinetic energy $T_{\max}$. $K \approx 0.31\,\mathrm{MeVcm^2mol^{-1}}$ is a constant normalisation factor and $\delta(\beta\gamma)$ a parametrised correction for relativistic density effects.

Actually, the high critical energy of muons leads to a low stopping power for muons in matter and a calorimeter which can contain muons has to be very large. Therefore, muon energies are usually not measured with calorimeters in collider experiments. But the weak energy dependence of ionisation between the point of minimum ionisation and the critical energy allows to use muons to generate reference signals for detector calibration. The ionisation loss will practically stay the same over the full path of the muon, although the muon gets slowed down.

Electrons have a much lower critical energy than muons, due to their smaller mass. The high probability of photon generation due to bremsstrahlung leads to a much higher stopping power for electrons than for muons. Therefore, electrons can easily be absorbed in a calorimeter. The fractional energy loss over one radiation length is depicted in figure 2.2(a) for electrons and positrons. The radiation length X_0 is defined as the distance in which an electron looses $1 - 1/\mathrm{e} = 63.2\,\%$ of its energy.

Photons interact with matter via electromagnetic processes, too. Figure 2.2(b) shows the cross section for several processes of photons in copper. At low photon energies, the photo-electric absorption is dominant. Rayleigh scattering contributes only marginally. The probability for both processes falls off with increasing photon energy. Compton scattering of photons at the atomic electrons is present over a wide energy range and becomes dominant at a few MeV photon energy. The electron-positron pair production cross sec-

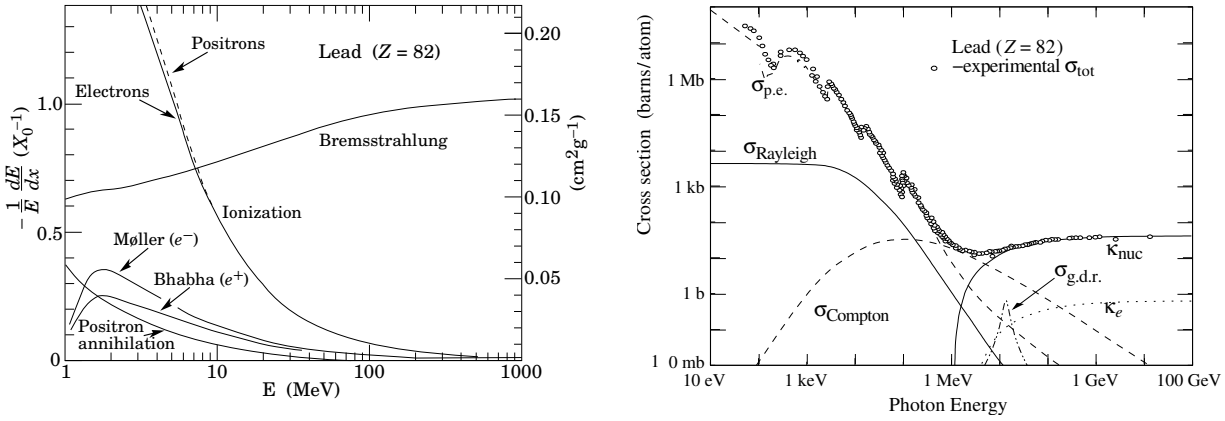

(a) (b)

Figure 2.2: (a) Fractional energy loss per radiation length in lead as function of electron or positron energy. Electron (positron) scattering is considered as ionisation when the energy loss per collision is below 0.255 MeV, and as Møller (Bhabha) scattering when it is above. (b) Total photon cross sections in copper as function of energy for different processes: $\sigma_{\text{p.e.}}$ atomic photo-electric effect; σ_{Rayleigh} Rayleigh scattering; σ_{Compton} Compton scattering; κ_{nuc} nuclear field pair production; κ_{e} electron field pair production; $\sigma_{\text{g.d.r.}}$ photo-nuclear interactions, dominantly the giant dipole resonance.
The pictures are taken from [3].

tion rises fast after the production threshold and dominates for higher energies. Due to the necessary momentum transfer, the pair production in the nuclear field dominates over the production in the electron field. Finally, photo-nuclear reactions can play a role in the absorption of photons. For example, photons can induce fission at the giant dipole resonance.

For energies above the critical energy of electrons (positrons) E_{c} bremsstrahlung and pair production dominate the interactions of electrons (positrons) and photons. The products of the reactions are again photons and electrons (positrons), or an electron positron pair, respectively. This leads to a cascade of particle multiplication, as long as the products stay above E_{c}. For lower energies, the charged particles loose their energy by ionisation. The photons below the pair production threshold transfer their energy to electrons either by Compton scattering or by the photo-electric effect. These electrons then loose their energy by ionisation again. Practically, the energy of the incoming particle is transferred to ionisation energy. For sufficiently high energies, it does not play a role, if the particle starting the cascade is an electron, positron, or photon. This allows to quantify the energy of the original particle by measuring the ionisation energy inside the absorber material.

2.1.2 Hadron Interactions in Matter

Hadrons are not elementary particles but consist of quarks and gluons. These can interact by the strong force with the quarks and gluons of other particles. In the case of a hadron passing through matter, the protons and neutrons of the nuclei can be partners for such

interactions. The nucleus itself is bound by the strong force. This implies that additionally to the already composed hadrons, multi body effects can play a role in the interaction of hadrons with matter. Altogether, this makes the interaction of hadrons with matter complicated and no full theoretical description of the processes exists so far.

Several concurring models exist to describe hadron nucleus interactions. Some use quantum chromodynamics considerations to calculate cross sections for different interactions, others are purely phenomenological. Most models are valid in a limited range of energy and different models have to be combined to describe hadron showers. More details about the modelling of hadron interactions can be found in the simulation chapter 6.

For the discussion of calorimetry, it is not necessary to know all details of the hadronic interactions. To understand the relevant effects it is enough to look at a simplified shower picture. The distance a hadron travels in average before it undergoes a strong interaction is called the nuclear interaction length λ_I. The exact value of λ_I is not only a material constant but also depends on the type of the interacting particle. In general λ_I is larger than X_0, which makes hadron showers longer and less dense than electromagnetic showers. In the interaction process new hadronic particles are generated. The average particle multiplicity mainly depends on the atomic mass. For typical absorber materials, the average multiplicity of charged particles is between 5 and 10 [12].

The pion is the lightest hadronic particle and consequently it is dominantly produced in the cascade of strong interactions. The three charge states of the pion are produced equally, such that one third will be neutral pions. Neutral pions decay practically instantaneously into two photons, or a photon and an electron positron pair. Also the η particles decay dominantly to electromagnetic particles. This implies, that a significant fraction of the energy will be deposited in electromagnetic showers.

Next to cascade particles generated in the hard interaction, protons and neutrons are released from the nucleus by spallation, evaporation and break up. Also the fragments of induced nuclear fission will have a small contribution to the shower. In the nuclear processes some of the energy is used to compensate the nuclear binding energy, or goes into the recoil of the fragments.

Between the hadronic interactions the charged hadrons will interact electromagnetically and ionise the atoms in matter. The ionisation densities can reach much larger values than for electrons, due to the large masses and low momenta the hadronic particles can reach before these are stopped or absorbed.

2.2 Signal Detection

As discussed, most energy is deposited as ionisation energy during the absorption of particles in matter. Different ways of detecting the ionisation energy exist. A popular method is the usage of scintillators and a detection of the scintillation light. Many different scintillators exist and can be chosen by different properties like light yield or time distribution of the signal. An established and widely used light detector is the photomultiplier tube. But also a set of semiconductor based photo-sensors exists. The light detection with these is discussed in chapter 3. Another method to measure the ionisation energy is to directly measure the current of ionisation charges in an electric field. To make this work a medium

which is in principal an insulator but allows some charge transport is necessary. Possible and used materials are gases, liquids, semiconductors, and diamonds.

Two different calorimeter types exit: homogeneous calorimeters and sampling calorimeters. Homogeneous calorimeters use the same medium as absorber and detector, while sampling calorimeters alternate layers of absorber with sensor layers. While homogeneous calorimeters reach a superior energy resolution for electromagnetic showers, sampling calorimeters allow to compensate the intrinsically different response of electrons and photons compared to hadrons. The usage of heavy absorbers allows to reach a compact and cost efficient design of sampling calorimeters. A segmented readout allows to obtain position and direction information.

2.3 Sampling Hadron Calorimeters

This work comprises measurements of a hadronic sampling calorimeter with highly segmented readout. Therefore, some aspects of the signals in this type of calorimeters are discussed here.

2.3.1 Spatial Development

In section 2.1 the length scales of electromagnetic showers, X_0, and hadronic showers, λ_I, have been introduced. In sampling calorimeters materials with different X_0 and λ_I are used. As long as the sampling frequency is high enough, the effective values can be calculated with the equations for composite materials:

$$\frac{1}{X_{0\mathrm{g}}} = \sum_i \frac{f_i}{X_{0\mathrm{g}\,i}}, \tag{2.2}$$

$$\Rightarrow \frac{1}{X_0} = \sum_i \frac{l_i}{X_{0i}}, \tag{2.3}$$

$$\frac{1}{\lambda_{\mathrm{Ig}}} = \sum_i \frac{f_i}{\lambda_{\mathrm{Ig}\,i}}, \tag{2.4}$$

$$\Rightarrow \frac{1}{\lambda_\mathrm{I}} = \sum_i \frac{l_i}{\lambda_{\mathrm{I}i}}. \tag{2.5}$$

The composite calculations (equations 2.2 and 2.4) use the values normalised to the material densities $X_{0\mathrm{g}}$ and λ_{Ig} in $\mathrm{cm^2 g^{-1}}$. f is the mass fraction of the component. The lengths in cm are given by $X_0 = X_{0\mathrm{g}}/\rho$ and $\lambda_\mathrm{I} = \lambda_{\mathrm{Ig}}/\rho$, where ρ is the material density. If the materials are not mixed but alternated, the density normalisation is not necessary and equations 2.3 and 2.5 can be used. In this case, l is the fractional length of the material.

A hadron can travel a significant distance before it undergoes its first hard interaction due to the rather large values of λ_I. The interaction probability is practically constant in a sampling calorimeter with reasonable sampling frequency, and the longitudinal position of the first interaction will follow an exponentially falling distribution:

$$P(z) = A \cdot \mathrm{e}^{-\frac{z}{\lambda_\mathrm{I}}}, \tag{2.6}$$

where $P(z)$ is the probability for the first interaction happening at z, and A is a normalisation constant.

Longitudinal Development

After the first interaction some part of the energy is transferred to electromagnetic showers via the generation of π^0. The shape of the electromagnetic cascade is shorter and shows much less fluctuations than the hadronic cascade, such that the event by event shape of hadronic showers depends strongly on the fraction of energy transferred to π^0. The average shower shape shows a steep longitudinal rise of the deposited energy and an exponential decay after the maximum is reached. Qualitatively, this can be explained by the particle multiplication in the cascade till the average particle energies are around the production threshold for new particles. At this point, all particles have approximately the energy of the production threshold and therefore have a similar mean free path before absorption. The longitudinal shape of electromagnetic showers can be approximated with the following empirical function [13]:

$$\frac{\mathrm{d}E}{\mathrm{d}z} = az^{\omega} \cdot \mathrm{e}^{-bz}. \tag{2.7}$$

The position of the peak energy deposition grows logarithmically with the incident particle energy. The average hadronic shower evolution is more complicated. The shower start point fluctuates and superposes cascades at different z positions. Furthermore, two cascade processes with different scales superpose with varying contributions. Finally, spallation neutrons can travel long distances before these give a signal in the detector.

Lateral Development

The cascade particles are produced under varying angles. In general the shower development is boosted in the direction of the impact particle due to momentum conservation. But with the decrease of the average particle energy, the shower grows wider. The angular distribution of different shower components vary, and two components are observed in electromagnetic showers which exponentially decrease with the radial distance to the shower centre. Several different parametrisations can be found in [13, 14]. In hadronic showers, the lateral size will be broadened by the hadronic component of the shower. Additionally, thermal neutrons are produced in the cascade and can travel long distances before generating a signal.

Time Development

The electromagnetic cascade practically develops with the speed of light, as particle generation is prompt and most of the cascade particles have relativistic energies. This is not true for hadron showers. Excited nuclear states can have considerable live times, and non-relativistic particles are produced in the cascade. For example, thermal neutrons can travel significant times through the detector before they generate a signal. These timing effects make the calorimeter response a function of the time acceptance of the readout electronics. This includes both the reconstructed shower energy as well as the spatial shape.

2.3.2 Response and Resolution

It was already discussed, that hadron showers contain processes that do not give a detectable signal. For many calorimeters, this leads to a different response to electrons and hadrons. The ratio of the visible signal produced by electrons and pions is called e/π-ratio. The fraction f_{em} of energy deposited in electromagnetic showers fluctuates from event to event. These fluctuations will give an additional smearing of the calorimeter response, if the electromagnetic and the hadronic response differ. Additionally, the mean electromagnetic fraction $\langle f_{em} \rangle$ depends on the energy of the particle, which will result in a non-linear response of the calorimeter in case $e/\pi \neq 1$.

Sampling calorimeters offer the possibility to influence the value of e/π by the choice of materials and sampling sizes. Combinations of low- and high-Z absorber materials allow to adjust the electromagnetic response. Also the ratio of absorber and active material influences e/π. The design of a calorimeter with $e/\pi = 1$ is called hardware compensation. In highly segmented calorimeters, it is also possible to use the different shapes of electromagnetic and hadronic shower components to approximate f_{em} event by event and weight the measured energy accordingly. Such techniques are referred to as software compensation.

The relative resolution σ/E of calorimeters usually follows the following form:

$$\frac{\sigma}{E} = \frac{a}{E} \oplus \frac{b}{\sqrt{E}} \oplus c, \tag{2.8}$$

where a is called the noise term, b the statistical term, and c the constant term. Electronics noise is independent of the signal energy and therefore gives the name to the first term. The statistical term comes from the fluctuations in the shower process and scales with the square root of the signal size. The more signal per incident energy is produced, the smaller this part of the resolution becomes. The constant term gives the size of fluctuation that scale with the signal. The source of such a component can be calibration uncertainties or non-linearities in the detector response, for example due to an $e/\pi \neq 1$.

2.3.3 Containment and Leakage

To fully contain the particle showers, calorimeters have to be of sufficient size. Especially, the hadronic cascade develops over large volumes and particle physics detectors have to make a compromise between shower containment and construction costs. In a 4π detector design, mainly the longitudinal shower size is relevant. Figure 2.3 shows the necessary depth for an average shower containment of 95 % and 99 % in iron. The energy carried by particles leaving the calorimeter is called leakage. The average leakage grows logarithmically with the incident particle energy E, for a fixed depth of material. This adds a non-linearity to the response of a hadronic calorimeter. Furthermore, the hadronic shower shape has large event to event fluctuations, which also reflects in fluctuations of the leakage. Such fluctuations deteriorate the detector resolution. In general, both linearity and resolution improve with increasing calorimeter depth.

Particle flow calorimeters can measure the shower shape due to their high spatial granularity. This allows to approximate and correct the longitudinal leakage event by event (see section 8.3).

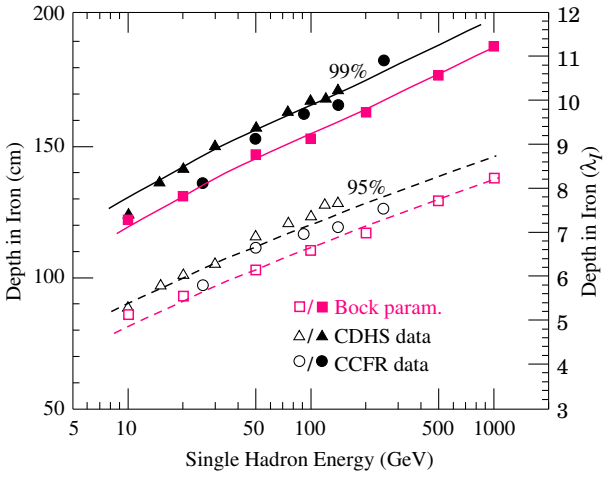

Figure 2.3: Required calorimeter thickness to contain 95 % and 99 % of the hadronic cascade in iron as function of the incident particle energy E. Experimental data from large neutrino detectors and calculations using the Bock's parametrisation [15] are shown. The picture is taken from [3].

Chapter 3

Photon Detection with Semiconductors

Photon detection and photon flux measurements play important roles in many experimental physics setups. The most commonly used devices are photomultiplier tubes (PMT), which multiply photo-effect electrons in a cascade of acceleration and secondary electron generation steps. These devices have a long history, and many different design variants ensure a broad applicability. PMTs are still the leading technology for many performance parameters like timing, gain, or noise. But, semiconductor based photo sensors become more and more competitive. In a few aspects these are even superior to classical PMTs: Semiconductor based devices allow more compact designs; the devices are insensitive to magnetic fields [16, 17]; and the photon detection efficiency can be significantly higher. Size and insensitivity to magnetic fields are important aspects for modern calorimeter design, where compact and highly granular calorimeters have to be placed inside the magnet of the detector system.

This chapter introduces the basic working principles of semiconductor photo detection. Especially, the group of Geiger-mode operated pixel devices, often called SiPM, will be discussed.

3.1 Operation Principles

The detection of photons in semiconductors is based on the generation of electron-hole pairs during the absorption of photons. The generated electrons and holes move in an electric field and the current of the moving charge is registered as signal. The electric field is generated by applying an external voltage to a *pn*-junction in a semiconductor. This allows to design complicated field configurations by doping. The detection efficiency of the sensors depends strongly on the photon energy. Optical photons have energies near the bandgap of silicon and the absorption length varies strongly with the wavelength. Photons with shorter wavelength have also a shorter absorption length and interact nearer to the surface. Therefore, the photon detection efficiency drops with shorter wavelength, as electron-hole pairs contribute to the signal only when these are generated inside the field region which usually is located below a passive protection layer.

If the electric field inside the semiconductor is high enough, electrons and holes can gain sufficient energy between collisions with the semiconductor lattice to generate further electron-hole pairs. This can be used to amplify the electrical signal. In general, holes

move slower than electrons due to their higher effective mass. Therefore, two amplification regimes exist. One where electrons take part in the multiplication process and one where both electrons and holes contribute. The timing of the electron multiplication process is faster and has less fluctuations. Consequently, many designs try to minimise the hole contribution to the signal. If hole and electron energies are above the amplification threshold, the system develops a continuous avalanche, as the two avalanches move in opposite directions and feed each other. This behaviour is called breakdown. Then, an external quenching of the avalanche is necessary.

Three groups of semiconductor based photo-sensors can be distinguished by their amplification regime:

No gain PIN diodes have a layer of not doped silicon between p- and n-doped layers. This configuration leads to a large depleted zone in which electron-hole pairs are collected. Accordingly, the quantum efficiency and the spectral sensitivity are high. But, the maximal generated charge is one electron-hole pair per photon. The signal amplitude is practically independent of the temperature.

Proportional gain Avalanche photo-diodes (APD) use a regime of linear amplification. Usually, the design combines a long drift region with a short avalanche region. This allows a good spectral acceptance and a good control of the amplification process. The maximum amplification is limited by the hole multiplication threshold.

Geiger-mode operation Several variants of photo-sensors exist, which use a working regime similar to a Geiger counter. The field design resembles the APD design, but the gain is so high that a continuous avalanche is started. This avalanche is quenched externally, often by a high ohmic resistor in the bias line. In this case, the signal induced voltage drop over the resistor brings the bias below the breakdown voltage and the avalanche stops. The size of the signal is defined by the geometrical design and the operation voltage, but not by the initially generated charge. This operation mode allows very high signal gains and a good control of the avalanche fluctuations. To achieve a sensitivity to the photon flux, several such Geiger counters can be combined in an array. Then, the number of active counters is related to the number of incident photons.

The gain of the avalanche multiplication depends on the temperature. This is due to the temperature dependence of the lattice vibrations. With increasing temperature the mean free path of the electrons and holes reduces, as the probability to interact with a phonon increases. Consequently, the electrons and holes accelerate less before they loose their energy in collisions and the gain of the device decreases.

The operation voltage influences not only the gain of the device, but also the size of the sensitive region inside the semiconductor. This leads to a change in detection efficiency with operation voltage and consequently to a change of sensitivity of the device.

3.2 Geiger Pixel Devices

The group of Geiger-mode operated devices is an actively developing field. Many different producers exist and no common naming convention exists. Hamamatsu, one of the biggest

photo-sensor producers in the world, offers their products under the name Multi Pixel Photon Counters (MPPC). But more frequently, these devices are called silicon photomultiplier and throughout this thesis the abbreviation "SiPM" will be used. SiPM is also used by the Moscow Engineering Physics Institute (MEPhI) and Pulsar as the brand name for their device series. Other producers and brand names are: SensL - SPM; Photonique - SSPM; Amplification Technologies - DAPD; Voxtel - SiPM; ST-Microelectronics - SPAD; CPTA - MRS.

All these devices use arrays of Geiger-mode pixels and resistive quenching of the avalanche. Different pixel geometries are used to optimise different aspects of the devices, like spectral sensitivity, surface fill factor, and optical crosstalk between pixels. The dynamic range of the devices depends mainly on the number of pixels and usually the producers offer a series of sensors with different pixel numbers.

Here the MEPhI/Pulsar SiPM is shown as a representative of the group of Geiger Pixel sensors. Figure 3.1(a) shows a photograph of the SiPM mounted on a ceramic plate. The top view of a single pixel can be seen in figure 3.1(b). In this picture, the quenching resistor and the bias lines are visible. Figure 3.1(c) schematically describes the semiconductor structure of the device. The resulting field configuration is shown in figure 3.1(d).

3.2.1 SiPM Characteristics

The CALICE collaboration collected vast experience with two types of SiPM: The MPPC in the scintillator based electromagnetic calorimeter, and the MEPhI/Pulsar SiPM in the analogue hadronic calorimeter and the tail catcher and muon tracker. The MRS and other devices are foreseen to be used in the next generation analogue hadronic prototype. Several properties influence the characteristic signal and response of the SiPM:

Pixel gain The pixel gain is the charge that one single diode releases when it is activated by a photon. It is usually expressed in units of elementary charges. The gain depends on the operation voltage, such that the gain can be varied within some range.

Photon detection efficiency The quantum efficiency, which is the probability to generate an electron-hole pair from an absorbed photon, is usually above 70 %. But, the probability for photon detection is lower due to passive areas on the detector surface, especially for devices with a large number of pixels. Also the probability to start a Geiger-avalanche after electron-hole pair generation is not unity. Typical values for the overall photon detection efficiency are around 15 % to 30 % for devices with 1000 to 500 pixels.

Optical crosstalk During the avalanche, photons are generated. These photons can travel to other pixels and activate these. This effect is often called inter-pixel or optical crosstalk ϵ. The size of the effect depends on the gain and on the geometrical layout of the pixels. Several producers improve the crosstalk by adding optical barriers.

Dark count rate Thermal noise is an intrinsic feature of all semiconductors. In the case of the SiPM, the thermal noise can initiate an avalanche and generate large signals. The noise scales with bias voltage and temperature. Typical dark count rates are of

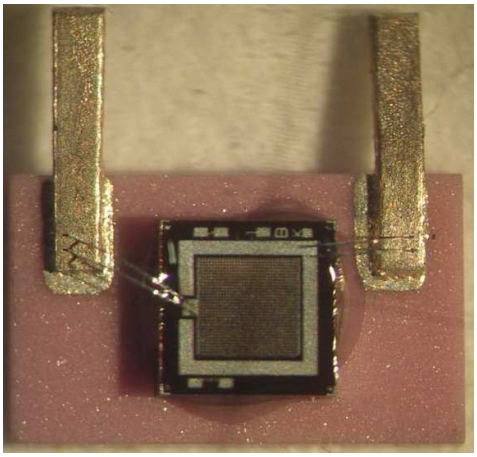

(a)

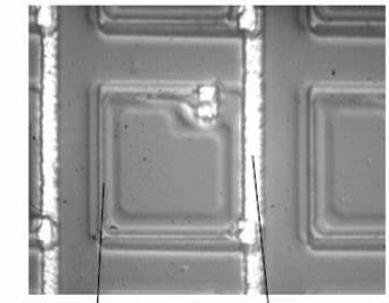

(b)

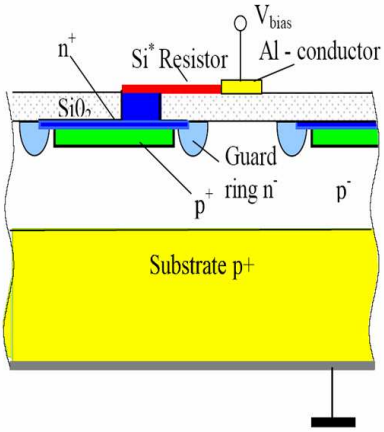

(c)

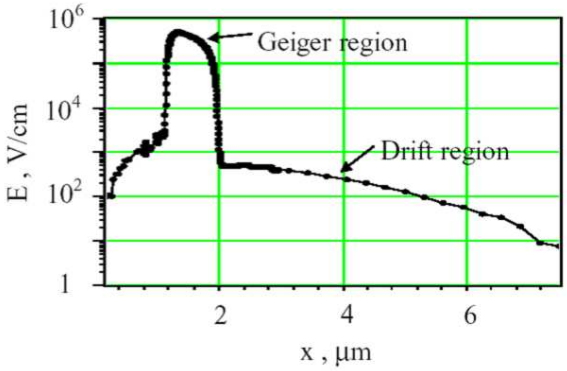

(d)

Figure 3.1: (a) MEPhI/Pulsar SiPM, mounted onto ceramic plate. (b) Photograph of SiPM pixel. The quenching resistor and the aluminium bias line are visible. (c) Schematics of a SiPM pixel semiconductor structure. (d) Electrical field inside a SiPM pixel. x position increases from top to bottom in (c). [18]

	MEPhI/Pulsar SiPM	Hamamatsu MPPC	unit
area	1×1	1×1	mm^2
pixel	1156	1600	
gain g	0.5	0.275	Me
photon detection efficiency	15	25	%
dark rate (max)	1 (3)	0.3 (0.6)	MHz
pixel dead time	> 100	4	ns
inter-pixel crosstalk	25	5	%

Table 3.1: Properties of two different SiPM devices. Photon detection efficiencies (PDE) include crosstalk and after pulses. Values are collected from [18, 19, 20, 21, 22].

order MHz. Due to the optical crosstalk, there is a significant probability for coherent firing of several pixels, which increases the average amplitude of the noise signal.

Number of pixels The number of pixels influences the dynamic range of the devices. An increased pixel number leads to better linearity, but is at concurrence with the pixel gain and photon detection efficiency.

Pixel dead time The recovery time of a pixel depends on the pixel capacity and the size of the quenching resistor. The dead time influences, if a pixel can fire only once or several times during one measurement. Depending on the duration of the light pulse, the effective number of SiPM pixels can be increased for short recovery times.

Typical values for some of the properties are shown in table 3.1. The values depend on the exact working point and can be adjusted within some limits by changing the operation voltage. The scintillator SiPM systems used in the AHCAL have been adjusted to a light yield of approximately 14 pixel per minimum ionising particle. The resulting distribution of the SiPM gain is shown in figure 3.2(a).

3.2.2 Response

Due to the limited number of pixels, the SiPM exhibits saturation. The mean signal A of a SiPM expressed in units of electron charges is related to the number of incoming photons N_γ by:

$$A = g \cdot N_{\text{eff}} \cdot \left[1 - \mathrm{e}^{-\frac{\eta_{\text{PDE}} \cdot (1+\epsilon) \cdot N_\gamma}{N_{\text{eff}}}}\right], \tag{3.1}$$

where N_{eff} is the effective number of pixels and g is the gain of a single pixel. η_{PDE} denotes the photon detection efficiency and ϵ the optical crosstalk probability. Figure 3.2(b) shows the response for different N_{eff} and ϵ. The pulse height spectrum of a SiPM shows a typical multi-peak shape due to the Geiger operation of the single pixels. This spectrum allows to easily measure g. Figure 4.3(a) displays such kind of spectrum including the gain fit (see section 4.4.1). The SiPM response can be linearised, if the response curve is known. An example for such linearisation is described in section 4.4.

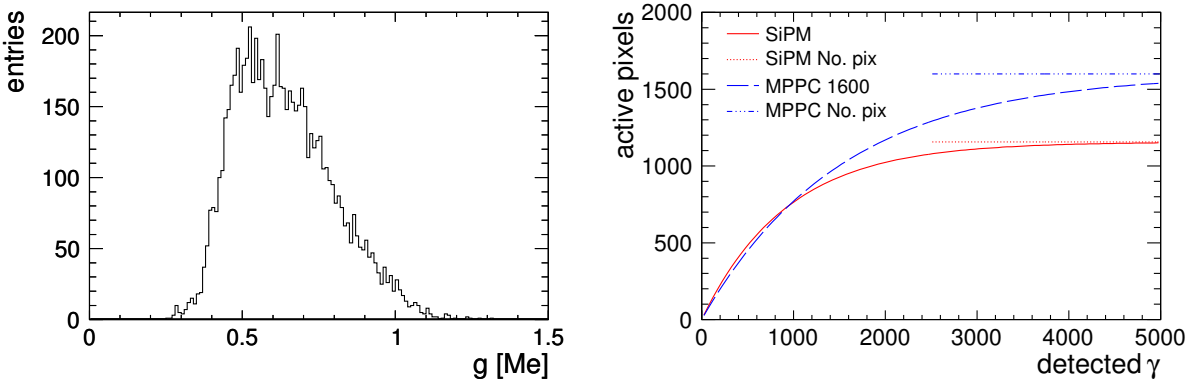

(a) (b)

Figure 3.2: (a) Histogram of the pixel gain of the SiPM used in the AHCAL prototype. The scale uncertainty is ±5%.
(b) Theoretical response curve of two MEPhI/Pulsar SiPM (solid red) and MPPC (dashed blue). The number of activated pixels is drawn as function of detected photons, to show the response independent from gain and photon detection efficiency. Values for number of pixels and optical crosstalk are taken from table 3.1. The SiPM curve shows a steeper rise due to the larger optical crosstalk and a lower saturation level due to the smaller number of pixels. To guide the eyes, the saturation levels are included as broken lines.

3.2.3 Signal Shape

Figure 3.3 shows the pulse shapes of different silicon photomultipliers at different light intensities. Two MEPhI/Pulsar devices with different quenching resistors and the 1600 pixel version of the MPPC are shown. At low amplitudes, the single pixel signals are visible as individual peaks.

The time distribution of the signal is defined by the time distribution of the photons. With increasing light intensity the signal shape changes depending on the dead time of the pixels. The MEPhI/Pulsar device with 8.5 MΩ has a dead time which is much longer than the time distribution of the light signal. Therefore, the signal saturates at the physical number of pixels. Additionally, the signal becomes shorter. This is also due to the saturation of the device. The pixels can fire only once, but with increasing intensity the probability to fire the pixels still increases and the pixels fire earlier. In the limit of extreme saturation all pixels fire coherently, and the signal form corresponds to the single pixel signal. The MPPC has a pixel dead time smaller than the light distribution. Accordingly, the pixels can fire more than once. But within one dead time interval, the pixels can fire only once. This limits the amplitude of the signal and leads to a broadening of the signal when the device saturates.

The short dead time of the MPPC increases the number of effective pixels. Under this extreme illumination more than 5000 pixel charges are measured while the device has only 1600 physical pixels. In contrast, the MEPhI/Pulsar devices saturate at their physical number of pixels of 1156.

The different quenching resistors lead also to a different shape of the signal tail. A comparison of the highest light intensity for the two different quenching resistors shows, that the higher quenching resistor leads to a larger time constant in the tail of the signal. The main peak is only slightly influenced by the quenching resistor. The reason for this is that charge carriers are generated and annihilated within the capacity of the sensor during avalanche and quench.

Electronics for SiPM readout have to be sufficiently stable against the shape changes of the device. This can be achieved by choosing an integration time larger than the width of the main peak. The tail is usually flat enough to show no significant changes in amplitude.

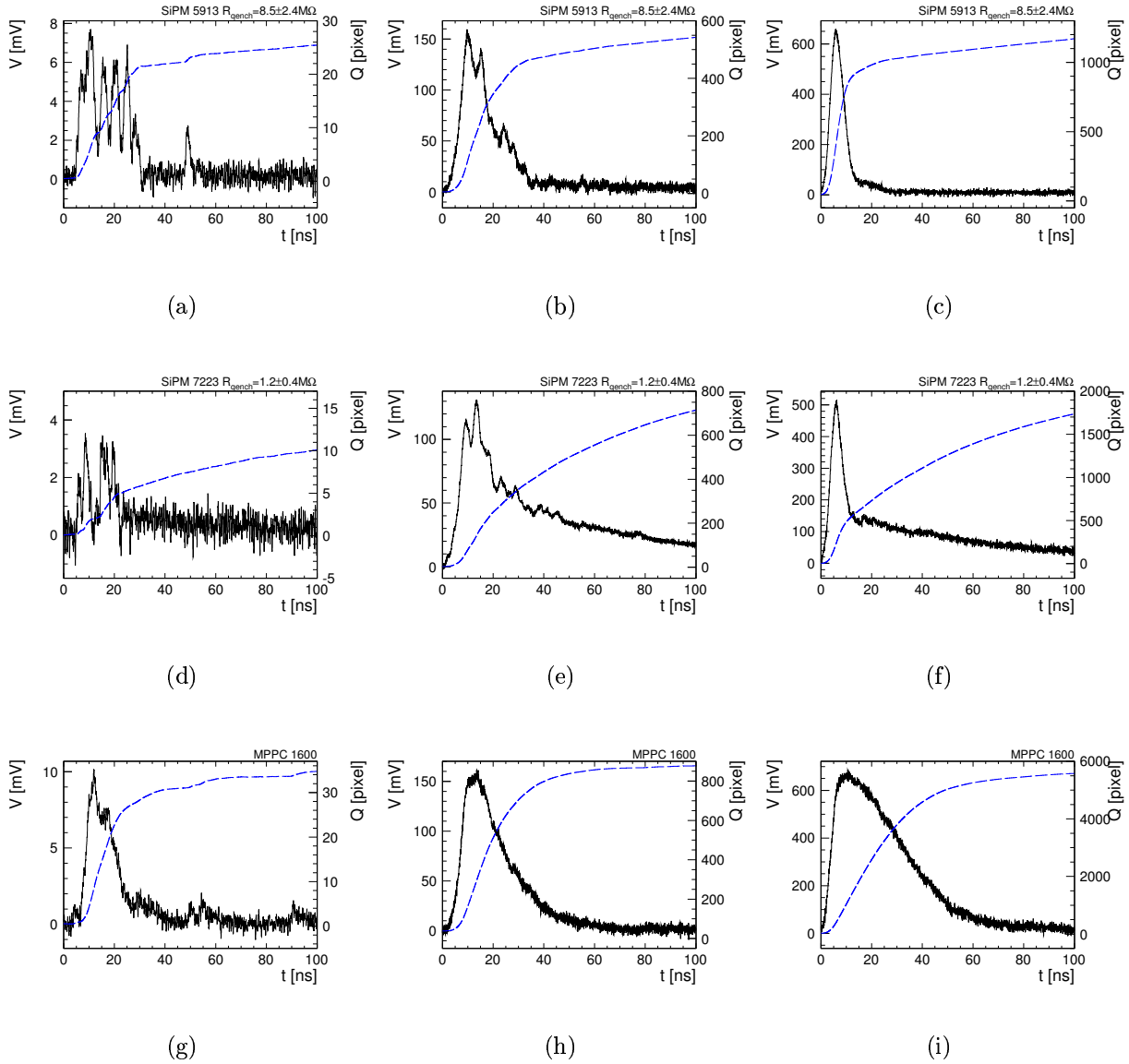

Figure 3.3: SiPM pulse shapes for different device types and light amplitudes measured with a high bandwidth oscilloscope. The light signal is generated by illuminating a scintillator with an ultraviolet LED. The scintillation light is coupled with a wave length shifting fibre to the SiPM. The dashed, blue line shows the integrated charge as function of time. The charge of a single pixel is measured with an integration time of 50 ns, and the integral charge should be read at the same time. The light intensity increases from left to right. The MEPhI/Pulsar devices saturate at their physical number of pixels. The MPPC shows a significantly larger effective number of pixels than the physical number. See the text for further explanations.
(a) – (c) MEPhI/Pulsar SiPM with 8.5 MΩ quenching resistor.
(d) – (f) MEPhI/Pulsar SiPM with 1.2 MΩ quenching resistor.
(g) – (i) MPPC with 1600 pixels.

Chapter 4

The Analogue Hadronic Calorimeter Physics Prototype

The analogue hadronic calorimeter (AHCAL) is a steel-scintillator sandwich calorimeter. It has an active area of 90 cm times 90 cm and a depth of roughly 120 cm which corresponds to 5.3 nuclear interaction length λ_I. This chapter will give only a short overview of the technology and layout. A detailed description of the detector can be found in [23]. Instead, the calibration procedure and the resulting systematic errors are discussed in detail.

4.1 Layout

The calorimeter has 38 scintillator layers subdivided into different cell sizes. The central core of 30 cm times 30 cm consists of square tiles with 3 cm border length for the first 30 layers. It is surrounded by a 3 cells wide frame built from tiles with 6 cm border length. In the last 8 layers the inner core is also made of such 6 cm tiles. Twenty tiles with 12 cm side length extend the 4 sides of the scintillator square to a total of 90 cm diameter. The partition of the scintillator into readout channels is depicted for the two variants in figure 4.1. The layout leads to a total of 216 readout channels in the fine and 141 readout channels in the course variant, respectively.

The 5 mm thick scintillator tiles are housed in modules which can easily be slid into or removed from the absorber. Each module consists of two 2 mm thick steel plate covers, two layers of reflective foil, and a printed circuit board (PCB). Readout cables and optical fibres are routed on top of the printed circuit board. The figure 4.2 shows a profile of the module layer structure.

The absorber stack is made from hot-dip galvanised steel plates. The plates and the covers of the modules build the absorber. The design sampling ratio is 20 mm steel and 5 mm scintillator. The production uncertainties for steel plates lead to unexpected and significant variations in the practically achieved thicknesses. Therefore, the depth of the steel plates is individually measured for each layer. The plates can be sorted into three groups of similar depth within an accuracy of 0.1 mm. Table 4.1 summarises the results of this measurement [24].

The absorber plates are mounted on sliding rails connected at the back to a 20.5 mm thick steel plane. This plane is part of a rotating table which sits on a movable stage for

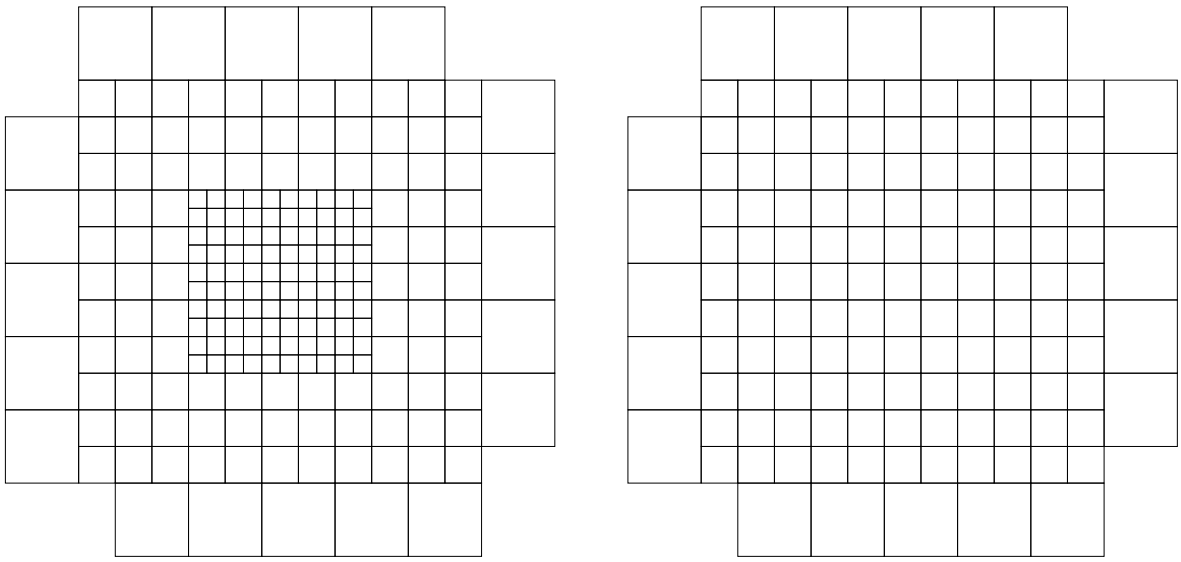

(a) (b)

Figure 4.1: The AHCAL readout segmentation: (a) Fine module with 216 readout channels. (b) Coarse module with 141 readout channels.

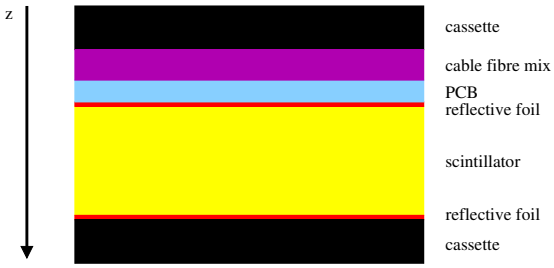

Figure 4.2: Profile of an AHCAL readout module.

layer	1	2	3	4	5	6	7	8	9	10
	17.4	17.4	17.4	17.6	17.4	17.6	17.6	17.4	16.7	17.4
+10	17.4	17.4	17.4	17.4	17.4	17.4	17.4	17.6	17.4	17.4
+20	17.4	17.4	17.6	17.6	17.4	17.4	17.6	16.7	17.4	16.7
+30	17.4	17.6	17.6	17.6	17.6	17.6	17.6	17.6		

Table 4.1: The AHCAL absorber thickness. All values are in mm, the measurement uncertainty is ± 0.1 mm.

x and y translation. This allows to freely chose the impact position in the (x,y)-plane and the impact angle of the beam in a test-beam environment.

4.2 Readout System

The scintillation light is collected with a wavelength shifting fibre (WLS) which runs in a groove trough the scintillator. The light is detected with a silicon photomultiplier (SiPM) at the end of the fibre. The opposite end of the fibre is closed by a mirror, to achieve a high light collection efficiency. The electrical signal of the SiPM is routed with coaxial cables to an application specific integrated circuit (ASIC). The ASIC includes an amplifier, a shaper, and a track and hold stage for each of the 18 connected channels. The ASICs sit on electronic boards attached to the side of the scintillator module. The signals are multiplexed and send to custom made VME cards (CALICE readout card – CRC), where the signal is digitised. A detailed description can be found in [25].

4.3 LED Calibration System

Each module has an LED calibration system attached to the opposite side of the readout electronics. LED light pulses are transferred with optical fibres to each scintillator tile. The LED system is capable of producing light intensities from single photons up to strong SiPM saturation. The calibration system is used to determine the SiPM gain, SiPM saturation level, and the inter-calibration of the ASIC operation modes. A detailed description can be found in [26].

4.4 Calibration and Reconstruction

Two steps are necessary to calibrate a sampling calorimeter. First, the single cells have to be equalised, including their readout chain. Then, the sum of all signals is a measure for the visible energy. In a second step, the visible energy has to be related to the total deposited energy. While the first step depends on the chosen readout technology, the second depends on the exact physics processes taking place. How to use the fine granularity of the detector to improve the total energy calibration is subject of several studies conducted within CALICE. The details of the individual cell calibration will be discussed here.

The use of SiPMs as photo-sensor adds additional requirements on the calibration procedure of the calorimeter. The calibration must not only equalise the response of the many different cells in the detector but also compensate the intrinsic saturation of the SiPM. Additionally, it is important to have an absolute reference of the calibration for the envisaged comparisons between measurement and simulation.

4.4.1 Calibration Parameters

A set of parameters has to be known before the calorimeter channels can be calibrated. The different variables and their measurement are described in this section.

Pedestal

The ASIC output has a non zero baseline. The exact offset varies from channel to channel. Additionally, the detector grounding configuration can lead to small changes in the baseline value. Therefore, the pedestal is measured regularly during data taking. Typically, five hundred pedestal events are taken for each ten thousand data events. These pedestal events are recorded as random trigger events while no beam extraction is ongoing. This ensures that no optical signal, except signals from very rare coincident cosmic muons, are present in the pedestal sample.

Additionally, a low frequency random trigger takes pedestal events during the recording of beam events. These were used to monitor for signal induced pedestal shifts. It could be verified that none are present. Furthermore, no significant contribution of shower signals for the pedestal events taken during beam extraction could be found.

Currently, the pedestal value is calculated as the mean of all random trigger events during reconstructions. This "on the fly procedure" is not ideal in two aspects. First, the statistical error of the pedestal is not constant over the run and can be relatively large for the first few thousand events. Second, it is not possible to follow short term pedestal variations, as these might have only a small statistical weight in the mean. An alternative method avoiding this varying statistics is currently in preparation and will become available in future.

Nevertheless, the influence on the reconstruction is considered negligible. On the one hand, the run length of 100k to 250k events ensures that only a small fraction of events with low statistic pedestal are recorded. On the other hand, the run duration of usually not more than two hours gives a short enough period to have only very small global changes. Additionally, the runs selected for this analysis have been checked manually for pedestal stability.

MIP

The most important quantity for the single cell calibration is the response to minimum ionising particles (MIPs). The energy deposition of a MIP is defined by the absorber material type and density, and its thickness. Both, thickness and material composition, are virtually identical for all cells in the calorimeter. Therefore, the signal of a MIP can be used not only for the equalisation of the cell response but also gives a good probe for the matching of the energy scales of simulation and measurement.

A broad beam of muons with known energy is used to record calibration spectra for each cell. The cells which were traversed by a muon are identified with a geometrical search for the muon path through the detector. The resulting spectrum is fitted with a Landau convoluted with a Gaussian. The Landau part of the function corresponds to the ionisation energy distribution while the Gaussian reflects the smearing due to the amplifier noise, to the relative thick absorber, and to the small amount of firing pixels of the SiPM at this amplitudes. The most probable value of the convoluted function is defined as the magnitude of a MIP.

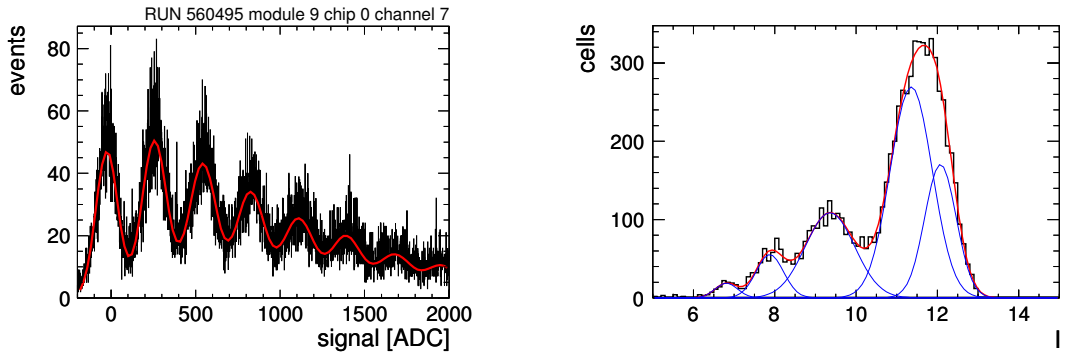

(a) (b)

Figure 4.3: (a) Gain calibration spectrum including multi-Gaussian fit. (b) Distribution of inter-calibration values.

Gain

The gain of a SiPM is defined as the size of the charge signal of a single firing pixel. It is measured by illuminating the sensor with small light fluxes, such that only a few pixels fire at once. Figure 4.3(a) displays a typical gain calibration spectrum. Each peak corresponds to a certain order of simultaneously firing pixels. The spectrum is fitted with a multi-Gaussian function to measure the exact peak distance. The result is depicted as a red line in the figure. A detailed description of the procedure can be found in [25].

During the measurement, the ASIC is operated in a special high gain, low noise mode to reach a signal to noise ratio sufficient for the SiPM gain determination.

Inter-Calibration

The ASIC is operated in two different modes. A mode with high gain and short shaping, called calibration mode, is used to measure the SiPM gain. All other measurements are performed in the so-called physics mode, which ensures a full coverage of the SiPM dynamic range. An inter-calibration of the two modes is necessary to transport the result of the gain measurement to the scale of the physics mode. As the shaping of the ASIC is changed between the two modes, the inter-calibration is not only a property of the electronics, but depends in addition on the shape of the SiPM signal. A test-bench measurement shows an inter-calibration value of 11.29 ± 0.03 [25]. The actual values with SiPM can vary from 6 to 13. Figure 4.3(b) shows the distribution of the measured values. The structure can be well described by five Gaussian distributions originating from different SiPM production series with specific quenching resistors.

Data are recorded in both ASIC operation modes for a set of different LED light intensities. The ratio of the two measurements gives the inter-calibration factor. An automatised selection of the points is performed to find those measurements which have a good enough signal to noise ratio and which are inside the dynamic range of the calibration mode.

Saturation Function

The SiPMs have a limited number of pixels. In our case, the dead time of the pixels has been chosen such that the pixels cannot fire more than once per event. This leads to a non linear response of the SiPM. An ideal SiPM would follow equation 4.1, where N is the total number of pixels and x the input light intensity. The x scale is chosen such, that the slope of the response function becomes unity in the origin (eq. 4.2).

$$f(x) = N \cdot \left(1 - \mathrm{e}^{-\frac{x}{N}}\right) \tag{4.1}$$

$$f'(0) = 1 \tag{4.2}$$

The responses of all SiPMs have been measured before those have been mounted on the scintillator tiles. The ideal function does not describe these curves satisfactorily. Therefore, an extended function is used to fit the measured curves. Equation 4.3 shows the function which matches the measurements well. The difference to equation 4.1 is the introduction of a second component. The pixels are split into two groups, where N_1 is the number of pixels of the first. N still denotes the total number of pixels. The condition 4.2 still has to hold, but the exact contribution of the two groups to the slope in the origin are left as an additional free parameter α. Practically, this form allows two groups of pixels with different sensitivity to light, one saturating faster than the other.

$$f(x) = N_1 \cdot \left(1 - \mathrm{e}^{-\frac{\alpha}{N_1} \cdot x}\right) + (N - N_1) \cdot \left(1 - \mathrm{e}^{-\frac{1-\alpha}{N-N_1} \cdot x}\right) \tag{4.3}$$

Saturation Level

The individual saturation functions have been measured before the SiPMs were mounted on the scintillator tiles. This gives an additional uncertainty on the response of the full scintillator-SiPM-system. Not all SiPM pixels might be illuminated, due to the imperfect matching of the round wavelength shifter fibre and the square SiPM surface, especially in the case of misalignments. Figure 4.4 shows an example picture where the light cone of the wave length shifter fibre is not centred on the SiPM surface.

The number of pixels which can detect light are reduced in this situation. Therefore, the total number of pixels N from the saturation function measurement has to be replaced with an effective number of pixels $N_{\text{eff}} = s \cdot N$. The scaling factor s can be measured with the help of the LED calibration system. The response of the scintillator-SiPM-system is scanned with high light intensities and fitted with an exponential function. s is determined as the ratio of this measurement to the result of a fit with the same function to the data taken before the SiPM was mounted on the scintillator. A detailed description and discussion of the measurement procedure can be found in [27]. For the CERN 2007 data taking period, an average value of 0.8 was measured for s.

The scaling has to be incorporated into the saturation function, as it is measured without this effect. It is assumed that the scaling affects both types of pixels equally,

Figure 4.4: Example of a not fully centred light cone on the SiPM surface.

resulting in:

$$\begin{aligned} f^*(x) &= s \cdot N_1 \cdot \left(1 - \mathrm{e}^{-\frac{\alpha}{s \cdot N_1} \cdot x}\right) + s \cdot (N - N_1) \cdot \left(1 - \mathrm{e}^{-\frac{1-\alpha}{s \cdot (N-N_1)} \cdot x}\right) \\ &= s \cdot \left[N_1 \cdot \left(1 - \mathrm{e}^{-\frac{\alpha}{N_1} \cdot \frac{x}{s}}\right) + (N - N_1) \cdot \left(1 - \mathrm{e}^{-\frac{1-\alpha}{N-N_1} \cdot \frac{x}{s}}\right)\right] \\ &= s \cdot f\left(\frac{x}{s}\right) \end{aligned} \tag{4.4}$$

4.4.2 Temperature Dependency

The SiPM breakdown voltage varies with temperature, as it is typical for a semiconductor device. This means that the gain calibration g and the MIP calibration M change with the temperature, too. The temperature dependence of these two quantities has been studied carefully in [27]. The values for the data taking period at CERN are $\frac{\mathrm{d}g}{\mathrm{d}T} = -1.7\frac{\%}{K}$ for the gain and $\frac{\mathrm{d}M}{\mathrm{d}T} = -3.7\frac{\%}{K}$ for the MIP calibration value. Due to a relatively large spread of the individual measurements, it is considered advantageous to use the mean value instead of the individual results.

The temperature of each detector module is monitored by five temperature sensors which are read out regularly during data taking. During reconstruction, the calibration constants are corrected for the temperature difference between calibration and measurement. A linear dependence on the temperature is assumed for both MIP and gain:

$$g_i(T_i) = g_{\mathrm{ref},i} + \frac{\mathrm{d}g}{\mathrm{d}T} \cdot (T_i - T_{0_i}) \tag{4.5}$$

$$M_i(T_i) = M_{\mathrm{ref},i} + \frac{\mathrm{d}M}{\mathrm{d}T} \cdot (T_i - T_{0_i})\,, \tag{4.6}$$

where T_i denotes the temperature during data taking and T_{0_i} denotes the temperature during calibration. Currently, the temperatures are taken as the temperature of the sensor nearest to cell i. More sophisticated extrapolations might be considered in future.

4.4.3 Reconstruction

The reconstruction implements equation 4.7 for single cell calibration:

$$E_i = f_i^{-1}\left((A_i - p_i)\cdot\frac{I_i}{g_i}\right)\cdot\frac{g_i}{I_i}\cdot\frac{1}{M_i} \tag{4.7}$$

The pedestal p_i is subtracted from the raw signal A_i for each channel i. As the result of the last step is in ADC units, the number of pixels has to be calculated from it before it can be desaturated. Therefore, the result is divided by the SiPM gain in physics mode $\frac{g_i}{I_i}$. Now, the signal is desaturated with a numerical inversion $f_i^{-1}()$ of the scaled saturation function 4.4. The result in units of pixels is calculated back to ADC units and normalised to the signal of a MIP M_i. Both, M_i and g_i are corrected according to equation 4.5 and equation 4.6, respectively.

4.4.4 Missing Calibration and Dead Cells

The calibration of each cell depends on several measurements, as described in 4.4.1. The choice to use average values for the saturation scaling, and the temperature dependencies of gain and MIP, ensure that all channels have a valid measurement for this quantities. Also the saturation curve determination is available for all channels, as it was done beforehand. All other measurements are taken during the test-beam data taking period and have some probability to fail for individual channels. The sources for such failures can be of different nature as well as a missing calibration information can have different consequences.

Pedestal A serious problem with the readout system has to be present to make the pedestal measurement impossible. Only one such problem occurred during the seven weeks of data taking at CERN in 2007. The very few affected runs are not considered for analysis.

MIP The muon data are available with sufficient statistics over the full AHCAL surface. The geometrical identification of the muon track gives a high purity of signal events such that a failure of the fitting method is quite unlikely. This leaves technical problems with the SiPM or the readout channel as the main source of missing muon calibrations. A total of 98.2 % of the channels have a valid MIP calibration. The remaining 1.8 % are considered to be dead channels. Most of the dead channels seem to be related to imperfect soldering junctions inside the module which opened under the strong transportation vibrations as repair tests with one module showed. The remaining dead channels can be attributed to failing readout electronics or SiPMs which stopped to operate.

Inter-calibration The inter-calibration measurement depends on the operation of the LED system. This gives additional sources for failures compared to the MIP measurement, like broken LEDs or light distribution fibres. Due to problems with the LED calibration electronics, four modules could not be calibrated during the test-beam data taking and have been calibrated in a dedicated setup after the return to DESY. In total, values for 97.9 % of the channels could be obtained. A default value of 10 is assigned to the remaining 2.1 % of the channels.

Gain The gain measurement is based on the LED system. Other than the inter-calibration measurement, it depends on a careful adjustment of the light intensity. Additionally, it is sensitive to pedestal shifts which might be present during the running of the LED system. Finally, the quality of the SiPM can complicate the measurement. A reasonable signal to noise ratio is necessary to resolve the peaks which can be impossible to reach due to low pixel gain or a high SiPM noise rate. 96.5 % of all channels have a valid gain measurement, when the calibrations made at DESY are included. The remaining channels are calibrated with a default value of 400 ADC units.

Dead cells Channels might become inoperable between the MIP calibration measurement and the physics data taking. Therefore, the SiPM noise spectrum of the channels is monitored to identify channels which give no signal anymore. These channels are included into the list of dead channels determined by the MIP measurement.

4.4.5 Systematic Errors

All calibration measurements have inherent uncertainties and will influence the uncertainty of the cell calibration. One has to distinguish between two forms of calibration uncertainties: The statistical uncertainty of the measurement, and an uncertainty on the method of the measurement.

The Influence of Limited Statistics in the Calibration Measurement

In general, the statistical uncertainties are uncorrelated between different channels. Therefore, one could expect that for a several thousand channels system the statistical uncertainty of the calibrations average out and do not contribute. This is unfortunately not true for all kind of observables. The case of the MIP calibration constant will be discussed here. It is the only calibration constant where significantly large statistical calibration errors are present. This is due to the use of muons, which traverse only one out of the 216 cells of fine readout module, while all other methods calibrate all channels in parallel.

Figure 4.5(a) shows the distribution of the relative statistical error, as it is determined during the calibration fit. The tail to large values comes from cells with low statistics in the muon selection. The influence of this uncertainty depends strongly on the kind of measurement, especially as the AHCAL is not a 4π-detector. Usually, the beam is sent to a central place of the detector, to contain most of the shower in the volume with the highest segmentation and to avoid lateral leakage. Therefore, some cells contribute more to the signal than others. Accordingly, the expected uncertainty varies strongly with the number of cells that significantly contribute to the analysed observable. In the case of the MIP statistical error, this dependence is illustrated in figure 4.5(b). For each point, a histogram of the total statistical error for N randomly picked measurements from distribution 4.5(a) is generated. The band is the central $\frac{2}{3}$-range of the resulting distribution. Additionally, the mean, the median, and the most probable value of the distributions is plotted. If all cells in a measurement would contribute with the same weight, N would equal the number of active cells. This is usually not the case when analysing particle showers which can

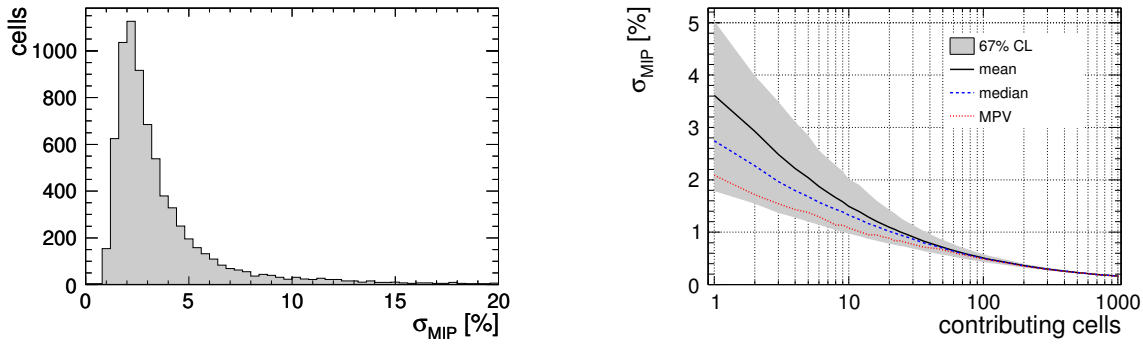

(a) (b)

Figure 4.5: (a) Distribution of the statistical MIP calibration errors. (b) Dependence of the total statistical uncertainty of the MIP value on the number of relevant cells. See text for further explanations

contain some cells which have a high activity but many others which are just above the detection threshold.

An extreme case is the analysis of electromagnetic showers in the AHCAL. Radially, the shower development is defined by the Moliere radius, which is approximately 2.5 cm for the AHCAL. Considering the cell size of 3 cm square and a beam width of typically less than 2 cm, most of the signal will appear in one to maximum four towers of adjacent cells, depending on the exact beam impact position. The longitudinal fluctuations are restricted in addition. Electrons or positrons practically always start to shower in the first layer and the shower deposits nearly all energy within 10 layers. This can be seen in figure 4.6, where the shower profiles and the integrated signal versus depth are shown for electrons or positrons with different energies. Altogether, this means that the same 10 to 40 cells will dominate the measurements of integrated observables like the energy sum. Observables like the energy per layer might be even dominated by single cells. In this case the statistical uncertainty of the calibration measurements can give a significant contribution to the total systematic uncertainty of the measurement.

Hadron showers are much broader and deeper than electromagnetic showers. Additionally, the start of the shower fluctuates significantly. This gives a much larger number of cells with significant contribution to the observables in hadronic showers compared to electromagnetic showers. In the very most cases, this allows to assume that the statistical uncertainty on the calibration constant does not give a significant contribution to the total error.

Calibration Method Uncertainties

The measurement of the parameters described in section 4.4.1 will inevitably have some systematic difference between the calculated and the actual value. The size and form of the mismatch between the two values will depend on the method used. Additionally,

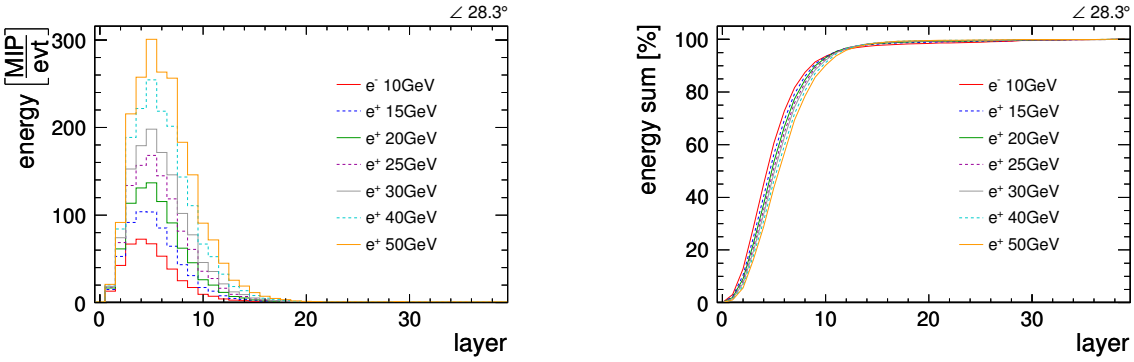

(a) (b)

Figure 4.6: Test-beam measurements at CERN. Calorimeter layers are rotated for 28.3 degree from nominal position. (a) Profiles of electromagnetic showers in the AHCAL for different beam energies. (b) Integrated signal versus calorimeter depth for different incident beam energies.

these errors cannot be expected to be uncorrelated between cells, like the statistical errors described before.

A general approach to describe the error would be a Tailor expansion:

$$X_{\text{measured}} = \xi_0 + \xi_1 \cdot X_{\text{real}} + \cdots + \xi_i \cdot (X_{\text{real}})^i \,, \tag{4.8}$$

where the observed value X_{measured} is developed in terms of the real value X_{real}. An exact determination of the coefficients ξ_i is not feasible. Some assumption on the dominant error has to be made. In the case of the pedestal, the signal shape is dominated by the electronics noise which is independent of the actual pedestal value or SiPM properties. Therefore, it is assumed that the dominant systematic error is a constant shift ξ_0. Due to the small pedestal width and the relative high signals, this error is expected to have no impact on the total systematic error. For all other calibration parameters, it is assumed that the linear term ξ_1 contributes dominantly to the systematic error, such that the following simplified description can be used:

$$X_{\text{measured}} = \xi \cdot X_{\text{real}} \tag{4.9}$$

The form of equation 4.7 leads to a mathematical equivalence of the systematic error ξ_{gI} on $\frac{g}{I}$, the gain in physics mode, and the scaling parameter s in equation 4.4. Additionally, the measurement of s includes the inverse of the same systematic uncertainty on $\frac{g}{I}$. It is very unlikely that there are common systematic effects which would cancel already in the measurement of s, as s is the ratio of the saturation levels measured with two different sets of electronics and independently developed fitting methods. Consequently, the systematic errors of gain g and inter-calibration I cancel when calibrating the single cells, leaving only the systematic errors on the scaling parameter itself and the uncertainty on the MIP. The MIP method uncertainty can be estimated from the difference between independent measurements. Here an uncertainty of 3 % is assumed [28].

Two more points have to be discussed before a final strategy for the systematic error estimation can be chosen: the usage of average values instead of single cell calibrations and the influence of the temperature correction. Average values are used for the scaling parameter s, the temperature slopes of gain and MIP ($\frac{\mathrm{d}g}{\mathrm{d}T}$ and $\frac{\mathrm{d}M}{\mathrm{d}T}$), and in the case of missing calibrations for inter-calibration I and gain g. Errors introduced by the last point are not different to method uncertainties for g and I, which have been discussed already.

In the case of the gain temperature dependence, a systematic error will not be cancelled in the same way, as the temperature might differ between inter-calibration measurement and the time of data taking. However, these effects are very small due to two reasons. For one thing, the spread of the single values is only 0.3 %/K [27], which is an upper limit for the systematic error due to averaging. For another thing, the temperature difference is small between scaling parameter measurement and data taking, which have been interleaved. A different situation applies for $\frac{\mathrm{d}M}{\mathrm{d}T}$. The MIP calibration measurement was performed only once at the beginning of the data taking period, which leads to larger temperature differences. Additionally, the spread between the single channels is larger. The size of the remaining systematic effect was estimated in [27] to be around 11 % which is in agreement with the differences observed for CERN and FNAL calibrations [28].

The choice of averaged values for the saturation scaling s is unfortunate in this case, as it mitigates the compensation of systematic errors on $\frac{g}{I}$. Systematics common to all channels will still be compensated, but not effects on smaller scales. It was already stated in section 4.4.1, that the effective number of pixels can vary due to a mismatch between wavelength shifter fibre and SiPM. The main effect is due to geometrical mismatch of the round wavelength shifter fibre and the square SiPM surface. There is some variation of the exact number due to additional misalignment, but the size is limited within the mechanical precision. Figure 4.7(a) depicts the measured values for s. The mismatch and the misalignment can explain the peak around 85 %; but, the long tail to small values cannot be explained by geometrical effects. The source for the tail can be twofold: Either the method to measure s fails for these channels, or $\frac{g}{I}$ has a large systematic error which is compensated. Without an alternative method to distinguish the SiPM saturation level it is not possible to verify the s measurement method. But, systematic errors on the gain in physics mode $\frac{g}{I}$ with the form of equation 4.9 will give a correlation between s and $\frac{g}{I}$.

The mean scaling factor $\langle s \rangle$ is plotted against $\frac{g}{I}$ in figure 4.7(b) to test for such correlation. To avoid influences of systematic effects in the measurement of s, a loose cut on the light yield of the cells and the maximum MIP value are applied. Such effects could be caused by limitations in dynamic range and thus would be correlated with the gain of the SiPM, too. A clear relation between $\langle s \rangle$ and $\frac{g}{I}$ is visible. The deviations from linearity can be explained by the different production groups of SiPM. Figure 4.8(a) shows that there is almost no correlation between the raw gain measurement g in calibration mode and the scaling. Figure 4.8(b) verifies that the cause of the correlation is indeed the measurement of the inter-calibration. The mean scaling is plotted against I rather than $\frac{1}{I}$, as it makes it easier to identify the jumps in the relation as transitions between the different SiPM production series visible in figure 4.3(b). That this groups of SiPMs have slightly different parameters can also be seen when looking at the average SiPM gain for the different inter-calibrations (figure 4.8(c)). Combining these observations, it can be concluded that systematic errors on the inter-calibration measurement method give a significant contribution to the spread of the scaling factor.

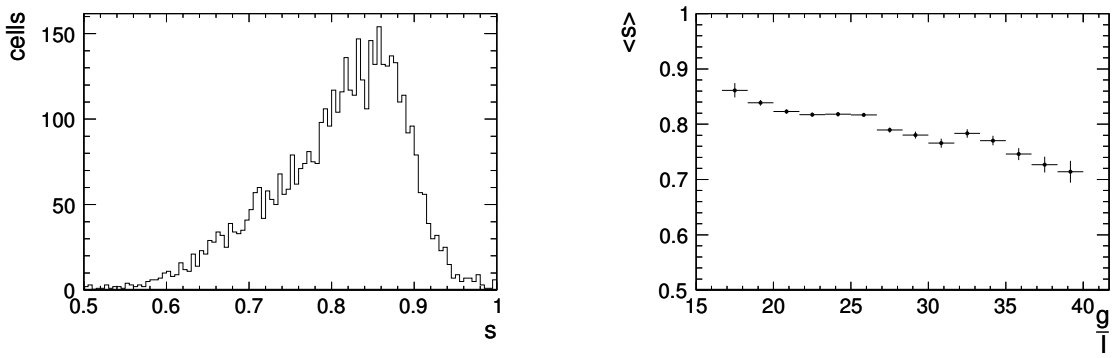

(a) (b)

Figure 4.7: (a) Distribution of the saturation scaling factors s. (b) Mean scaling factor $\langle s \rangle$ versus SiPM gain in physics mode $\frac{g}{I}$.

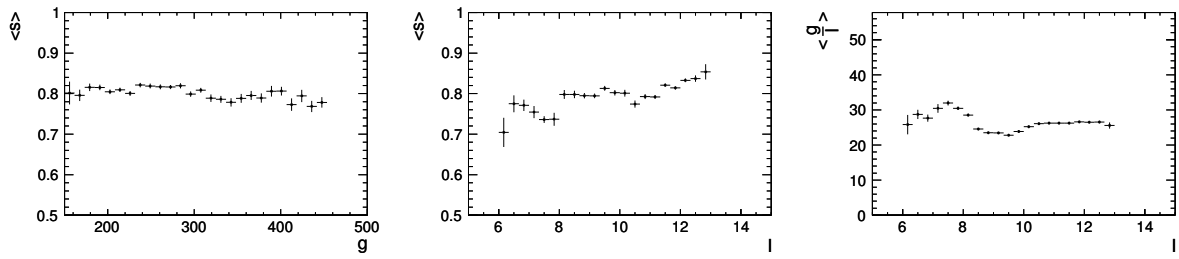

(a) (b) (c)

Figure 4.8: (a) Mean saturation scaling factor $\langle s \rangle$ versus SiPM gain in calibration mode g. (b) Mean scaling factor $\langle s \rangle$ versus inter-calibration I. (c) Mean SiPM gain in physics mode $\left\langle \frac{g}{I} \right\rangle$ versus inter-calibration I.

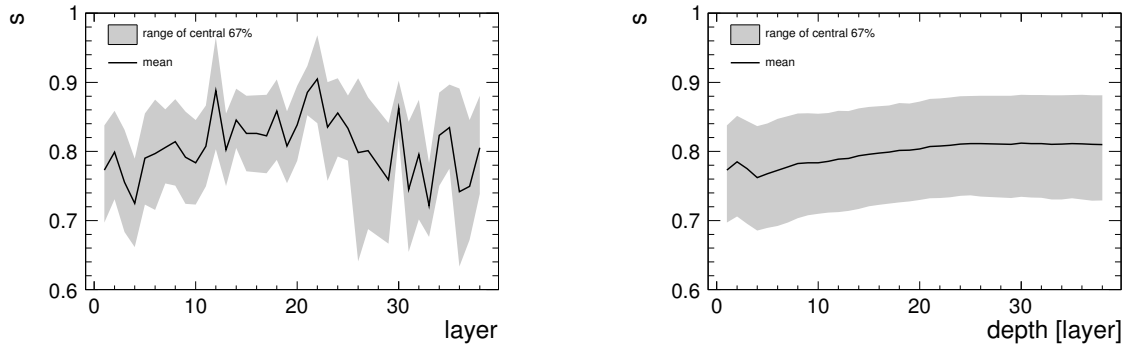

(a) (b)

Figure 4.9: (a) Saturation scaling factors versus AHCAL layer number. (b) Scaling factors versus calorimeter depth.

The exact size of the systematic uncertainty is hard to quantify. The unknown method uncertainties for the scaling parameter measurement are reduced by choosing the average value, but at the same time the influence of systematic uncertainties from the intercalibration measurements are not cancelled anymore. The observed spread of the distribution is therefore a combination of both errors. For this analysis, following strategy has been chosen: The central range of 67 % of the entries is defined as the range for the systematic error on $\langle s \rangle$. This choice will most probably overestimate the systematic error, as it assumes full correlation of the error for the cells in the signal. Nevertheless, the distribution of the scaling parameter over the different detector layers shows some significant grouping of cells with common shifts in the scaling factor. Figure 4.9(a) shows this distribution. The effective scaling parameter used within an analysis depends on the place of the signal in the detector. This effective scaling factor is displayed in figure 4.9(b) for signals reaching a certain depth in the calorimeter. In the case of electromagnetic showers, which deposit practically all energy within 10 layers, a reduced scaling factor of 0.78 ± 0.07 should be used instead of the value of $0.81^{+0.07}_{-0.08}$ for the full detector.

The complete set of systematic uncertainties is summarised in table 4.2. A verification of these assumptions can be found in section 6.3.

parameter	description	systematic error	
		full detector	EM analysis
M	MIP	$\pm 3\%$	$\pm 5\%$
$\frac{\mathrm{d}M}{\mathrm{d}T}$	MIP temperature dependence	$\pm 11\%$	
s	saturation scaling	$^{+9\%}_{-10\%}$	$\pm 9\%$
I	inter-calibration	cancels	
g	gain	cancels	
$\frac{\mathrm{d}g}{\mathrm{d}T}$	gain temperature dependence	not significant	
p	pedestal	not significant	

Table 4.2: Systematic error assumptions for the different calibration parameters.

Chapter 5

The CERN Test-Beam

Two test-beam campaigns have been conducted by the CALICE collaboration at CERN so far: One with partially completed detectors in summer 2006 and a second with fully equipped AHCAL and TCMT detectors during summer 2007. Since 2008, the setup is installed at Fermilab where additional data have been recorded. This chapter describes the CERN test-beam environment and the CALICE detector setup. It focuses on the 2007 data taking period, where the data relevant for this work have been collected.

5.1 The CALICE Experimental Setup

The CALICE experimental setup consists of three main detectors, the electromagnetic calorimeter (ECAL), the analogue hadronic calorimeter (AHCAL), and the tail catcher and muon tracker (TCMT). Together, these detectors comprise a cross-section of typical particle physics detector's calorimeter system. The detectors were running together for approximately 85 % of the total beam time. The ECAL was removed for the remaining 15 % of the beam time, to allow AHCAL only studies. Next to the main detectors, the setup includes several scintillator counters for triggering and beam quality monitoring, drift-chambers to record the incoming particle track, as well as a threshold Cherenkov counter for particle identification. Figure 5.1 sketches the layout of the test-beam experimental setup.

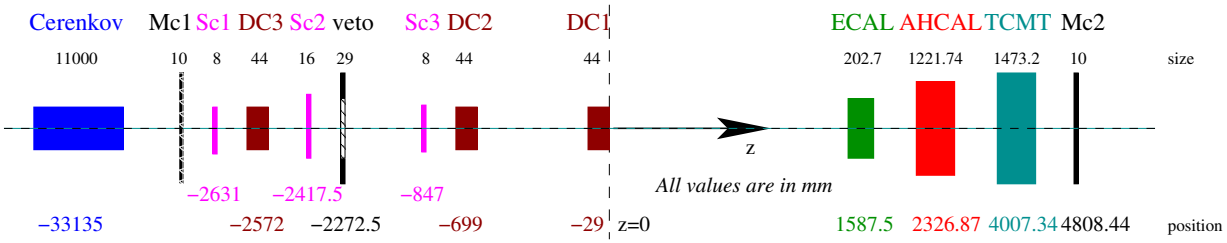

Figure 5.1: Sketch of the CERN 2007 test-beam installation. Scintillation counters are denoted as Sc, Mc, and veto. DC stands for drift chamber. Positions are measured from the exit window of the drift chamber DC1 to the centre of the objects. All dimensions are in mm.

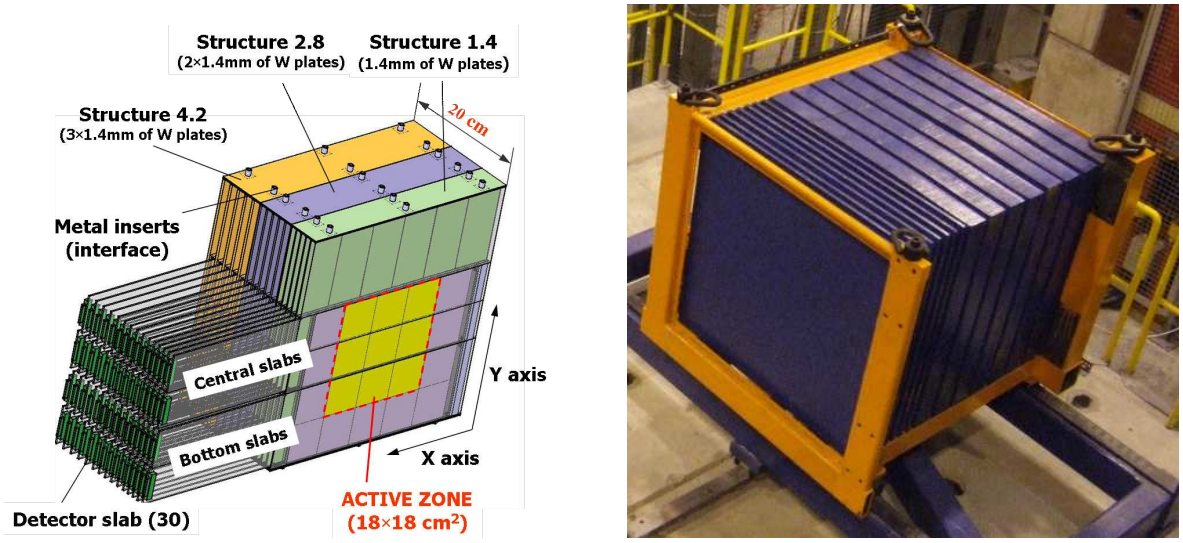

(a) (b)

Figure 5.2: (a) Sketch of the ECAL layout. (b) TCMT absorber stack with two different sampling structures.

5.1.1 The Silicon-Tungsten Electromagnetic Calorimeter

The Silicon-Tungsten electromagnetic calorimeter is a sandwich calorimeter of 24 radiation lengths. Longitudinally, it is segmented into three groups of ten layers each. The first ten layers have a tungsten absorber of 1.4 mm, the next group uses 2.8 mm tungsten, and the last group is equipped with 4.2 mm tungsten. The shower signal is detected with PIN diodes, which are laterally segmented into square pads with one centimetre border length. Figure 5.2(a) sketches the layout. A detailed description of the mechanical design can be found in [29]. The design is optimised for the detection of electromagnetic showers. The readout layers include additional materials that give a small difference between even and odd layers for electromagnetic shower development. This leads to a rather complicated structure for hadron shower development, due to the different ratio of radiation length X_0 to nuclear interaction length λ_I in the absorber and the readout layers. A detailed inventory of the ECAL material budget in terms of hadron shower development can be found in [30]. The total depth corresponds to approximately one nuclear interaction length, and approximately two thirds of the incoming hadrons start to shower already within the ECAL. Compared to the hadron shower development, the ECAL prototype has only a small lateral area of $20\times20\,\mathrm{cm}^2$, which makes lateral leakage likely for hadron showers. Considering the complicated longitudinal structure and the limited lateral size, this research concentrates on data recorded without the ECAL installed.

5.1.2 The Tail Catcher and Muon Tracker

The tail catcher and muon tracker (TCMT) is a sandwich calorimeter made of a steel absorber stack and plastic scintillator strips. It has in total sixteen readout layers of one

square metre size subdivided into twenty strips each. The orientation of the strips is alternated between consecutive layers. Each second layer of same orientation is shifted by hafl the width of a strip. The scintillation light is collected by wavelength shifter fibres and detected by the same kind of SiPM as installed in the AHCAL. The absorber stack has two different sampling structures. A picture of the empty absorber stack is shown in figure 5.2(b). The first eight absorber plates continue approximately the sampling structure of the AHCAL. The next eight absorbers are significantly thicker and correspond with ten centimetre thickness to the planned design of the ILD muon system. This structure allows to study the impact of the superconducting coil on the calorimeter resolution, which would be placed in the region of the TCMT fine sampling. In this work, the TCMT is used to identify muons leaving the AHCAL and classify events into events with and without leakage out of the AHCAL.

5.1.3 The Trigger System

The trigger system consists of a series of square scintillator counters centred around the nominal beam axis: two of ten centimetres border length, one of twenty centimetre border length, and three with one metre border length. The central one square metre trigger serves as a veto and has a cutout of twenty centimetres in the centre. It is coated with a two millimetre lead sheet to convert photons and segmented into four readout areas. The order of the triggers is outlined in figure 5.1. The first one square metre trigger can be removed from the beam line to reduce multiple scattering of beam particles. Mainly the two triggers with ten centimetre border length are used in coincidence as beam trigger. This restricts the trigger to events within the drift chamber acceptance. Two additional trigger configurations are used for muon beams: either a coincidence of the two outer square metre counters to record particles over the full calorimeter area; or the twenty centimetre sized scintillator to restrict the beam to the active area of the ECAL. The veto is not used in the trigger decision, but the status is recorded for later offline cleanup.

5.1.4 Auxiliary Detectors

The quality of the beam is monitored with additional auxiliary detectors, which can be used during the analysis to select beam events according to position, particle type, or multiplicity.

Multiplicity Measurement

The $20 \times 20\,\mathrm{cm}^2$ scintillator trigger has two independent readouts. One is used to generate the trigger signal. The second is used to record the amplitude of the scintillation light. The system yields a high enough signal to noise ratio to separate events with exactly one minimum ionising particle in the trigger from events where multiple particles crossed the scintillator area. Section 7.2 describes the calibration and performance of the multiplicity detector.

Drift Chambers

Three drift chambers record the particle track shortly before the impact into the detectors. These are delay wire chambers which allow position resolutions of approximately 0.2 mm. The working principle and operation instructions can be found in [31]. The calibration of the chambers in the CALICE test-beam setup is described in [32].

Cherenkov

The CERN beam line includes a threshold Cherenkov counter for particle identification. The radiator is a gas volume of eleven metre length. It can be filled with either nitrogen or helium, depending on the particle types that should be separated. Separation between electrons and heavier particles is only possible with helium gas. Nitrogen gas has to be used when pions or kaons should be separated from heavier particles at momenta lower than approximately 40 GeV, as the pressure limit of the system is reached for Helium gas. Threshold curves and theoretical efficiency of the specific Cherenkov system are plotted in figure 5.3.

Hodoscope

Some data was taken with an additional scintillating fibre hodoscope with multi anode photomultiplier readout. The hodoscope was placed directly in front of the calorimeters to measure an additional space point of the incoming particle track directly before the impact. Currently, no reconstruction code exists for this device. Data has been selected for this analysis without hodoscope installed, to avoid uncertainties from additional material in the beam line.

5.2 Particle Generation

The CALICE setup was installed at the CERN SPS North Area beam line H6. This beam line provides secondary and tertiary beams of electrons, muons, and hadrons. Particles are generated by sending a high energy proton beam from the SPS onto a beryllium target. The protons of typically 400 GeV generate secondary particles in the target. Particles of a certain energy are directed with magnets to the H6 beam line, where these can be either used directly or sent onto a second target to generate tertiary beams of lower energy. The choice of beryllium gives high hadron yields due to the large ratio of radiation length to nuclear interaction length $\frac{X_0}{\lambda_I}$.

5.2.1 Beam Quality

The quality of the beam can be influenced by the steering of the beam line magnets, collimators, and absorbers. Dipole magnets together with collimators are used to select the beam momentum and restrict the momentum spread. The beam shape is defined by quadrupole magnets together with collimators. Absorbers decelerate electrons stronger than pions and act as particle type filters when used together with the momentum selection.

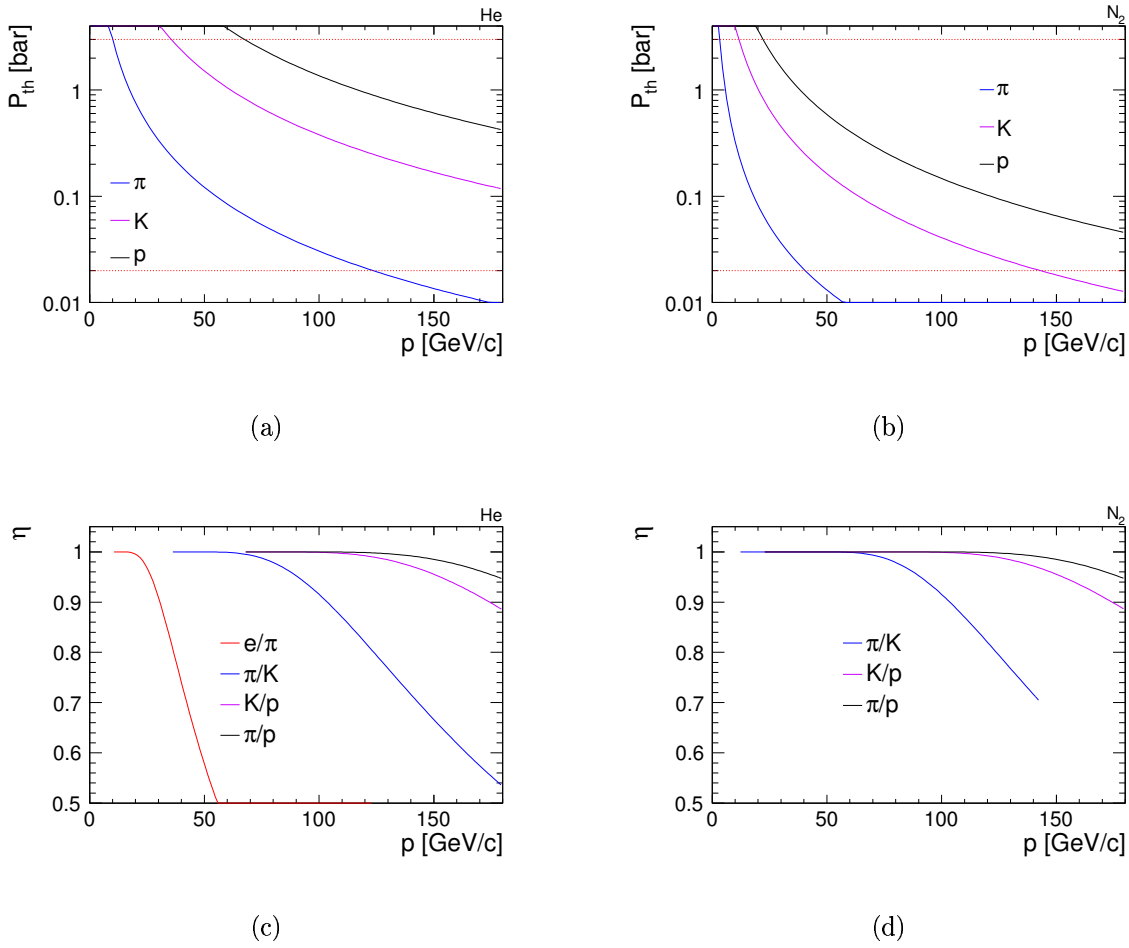

Figure 5.3: Cherenkov threshold pressure P_{th} versus particle momentum p when using helium (a) or nitrogen (b). The red dotted lines indicate the pressure limit of the CERN threshold Cherenkov. Theoretical detection efficiency η for the lighter particle when running at the threshold of the heavier particle in case of helium (c) and nitrogen (d). Lines are drawn in the range where P_{th} is within the pressure limits. Plots were generated using formulae from [33].

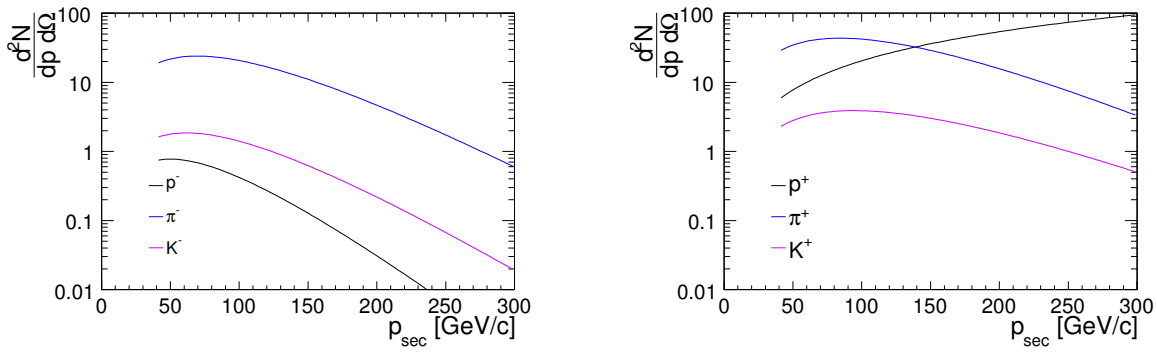

(a) (b)

Figure 5.4: Particle production rates versus secondary particle momentum p_{sec} for particles produced by 400 GeV protons on a beryllium target. Plots are generated using formulae and values from [34]. (a) Negative secondaries. (b) Positive secondaries.

Particle Composition

Particles are generated with different rates in the beryllium target depending on charge, type, and momentum of the generated particles. Figure 5.4 shows the hadron production rates versus momentum of the secondary particles measured at CERN [34]. Either positive or negative particles are selected for transport to the beam line. This selection gives the first possibility to modify the particle content of the final beam. Negative beams are preferred to generate pure pion beams, as the anti-proton production rate is much lower than the production rate for protons. Next to the hadrons, electrons and positrons are generated in the target.

After the main target, the beam is split to three beam lines: P0, H8, and H6. The limited aperture of the beam path to the beam lines gives a coupling between the momenta of the particles in H8 and H6. To allow more freedom in momentum selection, the H6 line includes a second target that can be used to produce lower energy beams. The target is followed by a second momentum selection. Instead of the target, a thin lead absorber can be used to decelerate electrons such that hadrons and electrons can be separated by momentum selection. A second lead absorber can be inserted just before the last dipole magnet to filter tertiary beams. The combination of momentum selection and absorbers is sufficient to reach rather pure hadron or electron beams. Only at lower energies, the Cherenkov detector becomes essential to achieve a good separation of electrons and hadrons.

Some of the pions decay during the transport through the beam line, therefore the beam always contains a certain fraction of muons. If the decay happens before the last momentum selection, these muons will have the same momentum as the other particles. Otherwise, the muons will have a momentum of at least 57 % of the mother particle, due to kinematic constraints. It is possible to generate rather mono-energetic muon beams by stopping all other particles with a closed collimator before the last momentum selection.

Momentum and Its Spread

The beam momentum is defined by a certain bending magnet in the beam line. The current of this magnet is recorded during data taking, which allows to calculate the exact beam momentum during analysis. The calculation of momentum and momentum uncertainty is described in [35]. The beam momentum is given by

$$p = \frac{I_{\mathrm{B5}}}{4.72 \frac{\mathrm{A}}{\mathrm{GeV}}}, \tag{5.1}$$

where I_{B5} is the current through the bending magnet 5. The size of the beam momentum spread is defined by the collimator restricting the particles during momentum selection. The full width beam momentum spread $\frac{\Delta p}{p}$ can be calculated by

$$\frac{\Delta p}{p} = \frac{\sqrt{C_3^2 + C_8^2}}{19.4 \frac{\mathrm{mm}}{\%}}, \tag{5.2}$$

where C_i is the full width opening of the collimator i. Accordingly, the Gaussian width is given by

$$\sigma_p = \frac{\Delta p}{2\sqrt{2 \ln 2}} \approx \frac{\Delta p}{2.35482}. \tag{5.3}$$

Beam Position and Shape

The beam position and shape can be monitored with the drift chambers. The chambers are at fixed places and their exact position was measured at the beginning of the data taking. This qualifies the tracking system as good absolute reference. During data taking, profiles at each chamber have been measured and used to steer the beam position. Full track information is available after reconstruction, combining the individual measurements. It has to be noted that inefficiencies of the chambers and the reconstruction algorithm bias the reconstructed profile. Figure 5.5 depicts this effect. While the single chambers give an almost smooth profile, the reconstructed tracks show a significant substructure and flattening in the peak of the distribution. This effect is especially dominant for the broad beam profile in x-direction. Depending on the necessary accuracy to measure the beam profile, it might be beneficial to use the single distributions. For this work, it is assumed that the bias is symmetric enough not to influence the mean position significantly. The beam width might be overestimated when fitting with a Gaussian distribution, but in general the beam width has only a small influence on the reconstructed signal.

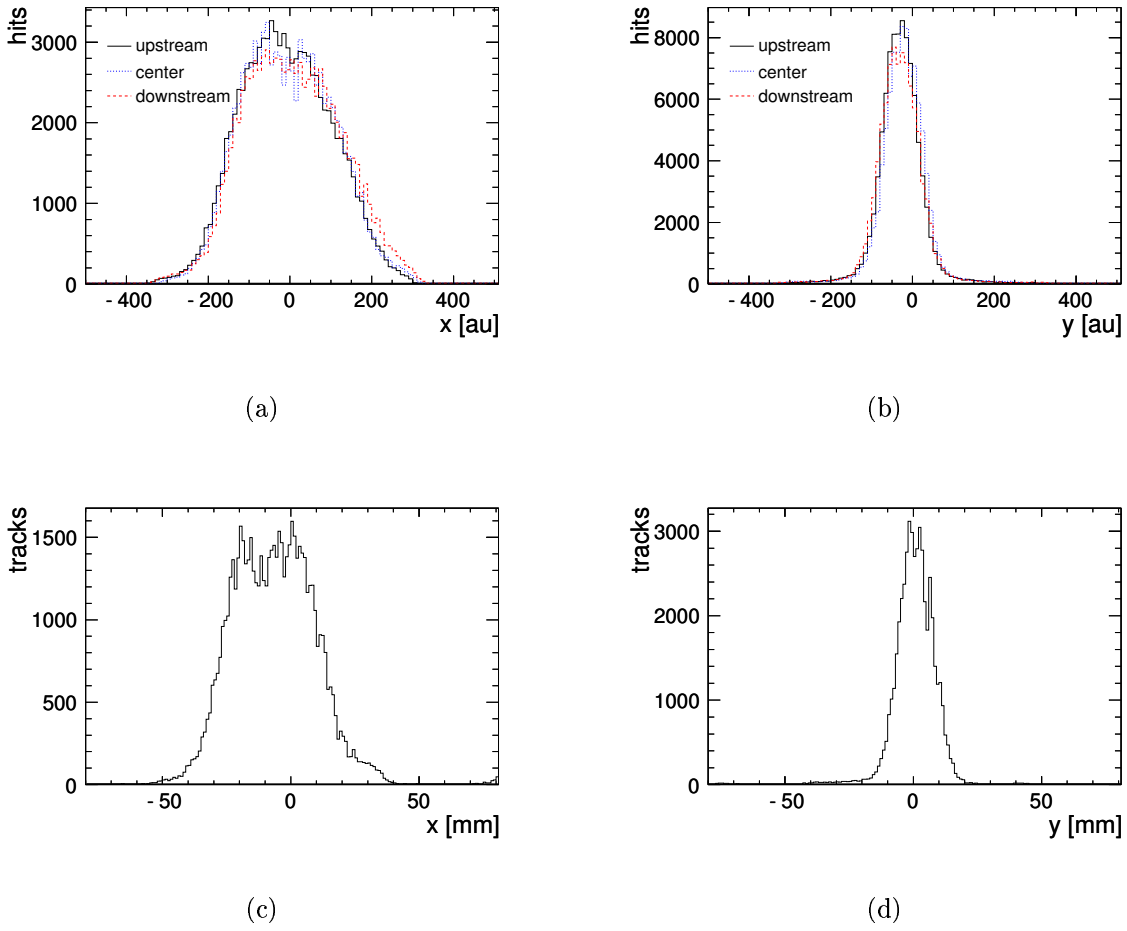

(a) (b)

(c) (d)

Figure 5.5: Drift chamber profiles of a 20 GeV π^- beam. Profile of particle position measured in the single drift chambers (a) and (b). Profile of the full track position at $z = 0$ (c) and (d).

Chapter 6

Simulation

Realistically predicting the performance of large scale detectors is important when designing particle physics experiments. The experiments are not only complex and expensive. Also modifications to the detectors are hardly possible after installation. This makes it important to understand the implication of all design choices already in the planning phase.

While electromagnetic simulations are well understood on the scales relevant for particle physics experiments, several alternative approaches exist to describe the interaction of hadrons with matter. This makes the test-beam measurements conducted by CALICE a valuable source for studying the performance of the different hadron models.

The CALICE collaboration simulates its detectors in the framework of Geant4 [36, 37]. The models for hadron simulation offered by this framework are described in section 6.1.

An accurate simulation does not only rely on the proper modelling of the physics processes in particle interactions, but also requires an equally good description of the detector geometry and response. The geometry of the CALICE detectors is modelled using the programme Mokka [38, 39]. Section 6.2 describes the details of the beam-line and detector modelling.

The chapter concludes with a verification of the detector simulation in section 6.3. The validation is performed by comparing measurement and simulation of electron showers.

6.1 Hadron Physics Simulation

The challenge in the simulation of hadron interactions is to predict the interaction of a multi body projectile with a multi body target. The incoming hadron consists already of a bound state of quarks. This projectile interacts with the nucleus, which is built of nucleons, which themselves consist of quarks. Additionally, the phase space of possible end states is manifold, as practically all hadrons with masses less than the collision energy can be generated. This makes it hard to find a single approach describing the complete behaviour of hadron interactions.

Different aspects of the system will dominate depending on the collision energy. This can be illustrated by a simplified picture of a projectile with De Broglie wavelength $\lambda = \frac{h}{p}$. The higher the energy of the projectile, the smaller the structures that are important in the interaction. Quark level interactions will dominate at high energies, while at lower

energies the system of nucleons governs the reaction. Accordingly, different hadron physics models exist which describe different energy regimes.

Geant4 includes both theory driven hadron models as well as parametrised models. The models relevant for this work are:

LEP & HEP The parametrised models LEP (low energy parametrised) and HEP (high energy parametrised) are essentially a translation of the GHEISHA [40] code into C++. Neither of them is a detailed hadronic model. The produced particles depend on parametrised fits to data. The two models are not considered state-of-the-art, especially as these do not conserve energy on an event by event basis. Nevertheless, the models are still used in many physics lists, mainly in two cases: Either to fill the gap between the validity interval of the other models, or for particle species the other models cannot describe. The LHEP physics list which is made only from these parametrised models is included in the comparison only as reference.

FTF In this model the incident particle interacts with one or several nucleons of the nucleus. The nucleus is modelled of protons and neutrons, following a harmonic oscillator or the Woods-Saxon density distribution for light and heavy nuclei, respectively. The interacting nucleons are chosen considering the impact parameter, the inelastic and diffractive cross sections, and the interaction centre of mass energy. The diffractive processes are simulated using the Fritiof [41, 42] approach, which gives the name to this model. In this approach a momentum exchanging string is formed between two quarks, one from each of the scattering particles. This string is described by its four momentum and the two quarks at the end.

A longitudinal fragmentation model is used to split the strings into hadrons and new strings until the energy in the strings gets too low for further splitting. In this model the string stretches due to the motion of its constituents. The string can break up by generating either quark-antiquark or diquark-antidiquark pairs. Half of this newly created pair forms a hadron with one of the string quarks, and the other half builds a new string with the remaining string quark. The longitudinal momentum of the string is split in this process following the Lund fragmentation function. A more detailed description can be found in [43].

After this step, the system consists of an excited nucleus and some number of secondaries. The interaction of the secondaries with the nucleus and the de-excitation of the nucleus need to be handled by further models. The acronym FTFB denotes the usage of the BIC model for the interaction of secondaries. Afterwards, the excited nucleus is handled with the Geant4 precompound model [44]. In the FTFP model only the precompound model is used to de-excite the nucleus.

QGS Another string model is the quark-gluon-string model. Its technical structure is quite similar to the Fritiof model, such that the Geant4 implementation uses common code parts for both models [43]. It differs from FTF in two aspects: In the way the strings are built and in the fragmentation function. The QGS model assumes that the hadron nucleon interaction is mediated by one or more Pomerons [45]. The Pomerons are then treated as pairs of colour triplet strings attached to partons of the interacting hadrons. The strings are fragmented in the same way as in the case of FTF, except that a different fragmentation function is used [43].

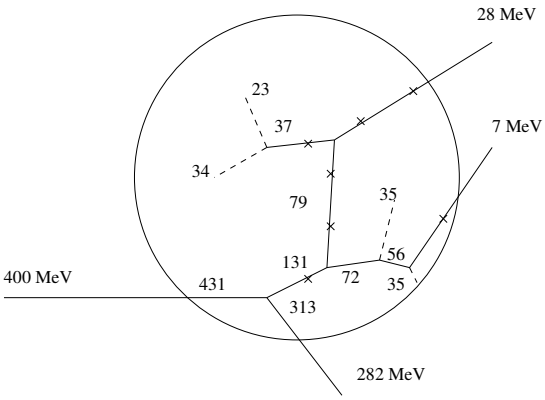

Figure 6.1: Schematic picture of the intra-nuclear cascade model. An incoming hadron of 400 MeV interacts with a nucleon and starts a cascade of further hadron-nucleon interactions. Crosses mark the places where the Pauli exclusion principle prevented the generation of new particles. The picture is taken from [46] and is a reproduction of Bertini's original work.

Like for the FTF models, a variant which uses BIC for the interaction of secondaries exists under the name QGSB. Additionally, a model called QGSC exists which uses CHIPS instead of the precompound model to de-excite the nucleus.

BERT The Bertini intra-nuclear cascade describes the interaction of a medium energetic projectile with the nucleons within a nucleus. The model is valid for protons, neutrons, and pions with kinetic energies between 200 MeV and 10 GeV. The nucleus is considered as a Fermi gas of nucleons. The incoming particle is tracked through the nucleus and can interact with the nucleons. The free path of the particle is calculated making some assumptions on the nucleon density of the target and using parametrised nucleon-nucleon cross-sections. The momentum of the struck nucleon, the type of the reaction, and the resulting products and their four momenta are calculated. Pauli's exclusion principle is taken into account by accepting secondaries only when these have sufficient energy to occupy a free state. In this case the Fermi gas model allows only particles with energies higher than the Fermi energy of the nucleus. Particles with energies higher than a cutoff energy are transported through the nucleus similar to the incoming particle. Figure 6.1 gives an schematic representation of such an intra-nuclear cascade.

The nucleus gets exited in the process of the nucleon-nucleon reactions. The Bertini model includes an exciton model which is characterised by the number of excited particles and holes. After all particles that can escape the nucleus have done so, the nucleus is de-excited applying several mechanisms. Pre-equilibrium evaporation using target excitation data, Fermi break-up by a simple explosion model in the case of extreme excitation, and fission based on a phenomenological model are applied. This is followed by the equilibrium evaporation using the Weisskopf model. More details about the Bertini cascade implementation in Geant4 can be found in [46].

BIC The binary cascade uses the same cascade principle as the Bertini model, where an incoming particle and the reaction products are tracked through a Fermi gas of

nucleons. It incorporates the Fermi exclusion principle in the same way Bertini does. Likewise, it includes an excitation model to handle the de-excitation of the nuclear fragment after the cascade.

The main difference is the description of the hadron-nucleon scattering. In contrast to the Bertini cascade, the collision partners are not directly transferred into the end state during inelastic scattering, but resonances of Δ and N are created. These are subsequently decayed using the branching ratios from the PDG [3]. The Geant4 implementation is described in [47].

CHIPS The chiral invariant phase space model is a quark level nuclear fragmentation model. Excited nuclear matter is described by quasmons which can be considered as an intermediate state of excited hadronic matter, in which the quarks are asymptotically free. The quark content of the quasmons is calculated with a statistical model assuming a critical temperature. The critical temperature takes into account that additional energy will be rather used to generate quark antiquark pairs instead of heating the system further. The quasmons can either decay by internal quark fusion leading to the emission of hadrons, or in the case of the presence of neighbouring nucleons by a double quark exchange with the neighbours. The exchange of quarks in both directions is necessary to obey colour charge conservation.

The generation of the exited nuclear state has to be modelled for the different incoming particles. Photo-nuclear, nucleon-antinucleon fusion, and pion capture at rest have been supported since quite some time. Actually, the CHIPS model is used in most physics lists to describe photo-nuclear reactions. In the QGSC model, it is used as back-end for the nuclear fragmentation of the exited nucleus left by the string model. But, the CHIPS model also has the potential to describe the full energy range as it combines quark and nucleon scales. Recently the model was extended such that it can be used over the full energy range. More details can be found in [44, 48, 49, 50].

6.1.1 Physics Lists

Different models describe different aspects of the interaction of particles with matter. It is necessary to combine several models to have a full description of the interaction of different species of particles with matter over the full energy range. For this purpose, Geant4 offers several "physics lists" [51]. The composition of the lists chosen for hadron simulation is explained in this section.

All studied lists use the same code to simulate electromagnetic physics. Most physics lists contain two or three hadron physics models to cover the full energy range. The only exception is the CHIPS physics list. A smooth transition between the models is reached by randomly selecting one of the two models in the transition region. The probability for the lists is varied linearly in the transition region. Table 6.1 includes the physics lists studied in this work. It tabulates which model is used for the different particles and energies. Usually, pions are used in our beam-tests. Pions are also the most frequently produced hadrons in high energetic showers. Therefore, the composition of the lists for pions has the largest influence on the results. Figure 6.2 gives a graphical representation of the model ranges for pions for all lists with transitions.

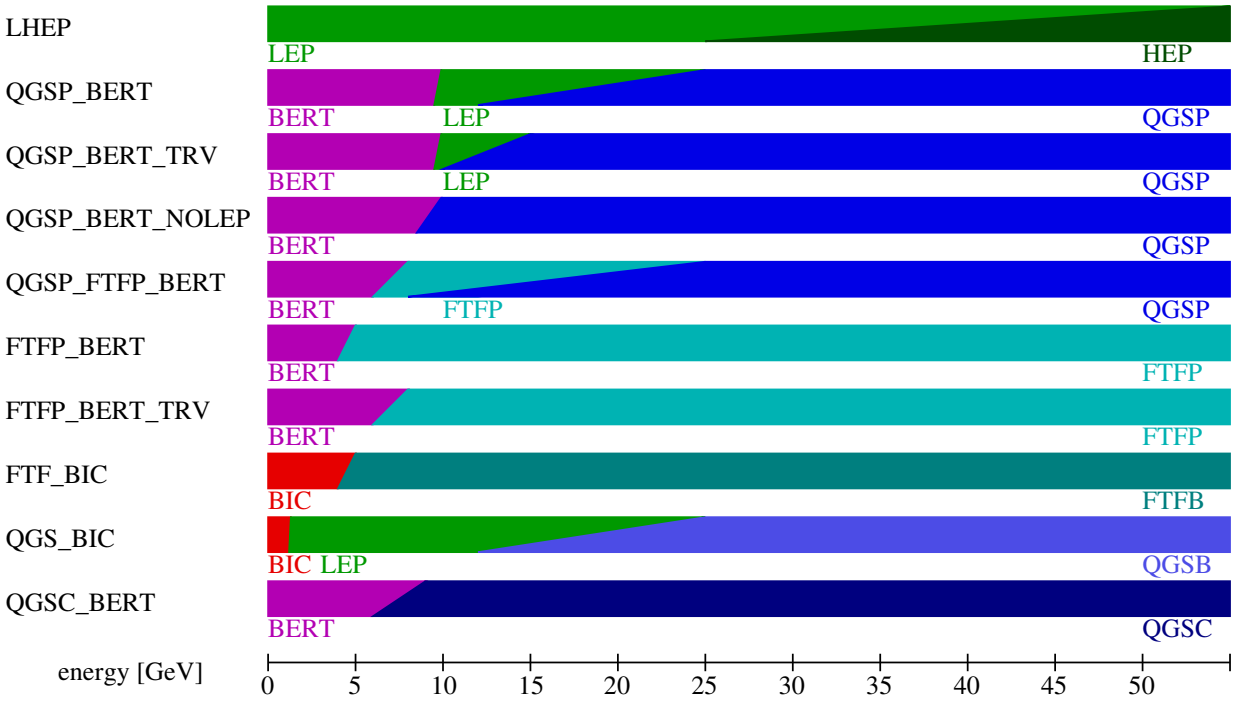

Figure 6.2: Composition of the studied Geant4 physics lists for pions. All physics lists that combine at least two models are shown. The energy range up to 55 GeV is displayed, which includes all transitions of the physics list. The last model is used for all higher energies, too.

Most simulations generated for this work are done using Geant4 version 9.3, released in December 2009. Exceptions are the QGSC_CHIPS and CHIPS physics lists. A bug in version 9.3 prohibits the usage of this version for these physics lists. Instead QGSC_CHIPS is simulated using Geant4 version 9.3beta. The CHIPS physics list is simulated with the most recent version 9.3.p01, as it is not present in the beta version.

physics list	particle	model									
		BERT	BIC	CHIPS	FTFB	FTFP	HEP	LEP	QGSB	QGSC	QGSP
CHIPS	all			all							
FTF_BIC	$\pi^{\pm}$ $K^{\pm}$ p n		< 5		> 4						
	$\bar{p}$ $\bar{n}$ Λ						> 20	< 25			
FTFP_BERT	$\pi^{\pm}$ $K^{\pm}$ p n	< 5				> 4					
	$\bar{p}$ $\bar{n}$ Λ						> 20	< 25			
FTFP_BERT_TRV	$\pi^{\pm}$ $K^{\pm}$ p n	< 8				> 6					
	$\bar{p}$ $\bar{n}$ Λ						> 20	< 25			
LHEP	$\pi^{\pm}$ p n						> 25	< 55			
	$K^{\pm}$ $\bar{p}$ $\bar{n}$ Λ						> 20	< 25			
QGS_BIC	$\pi^{\pm}$		< 1.3					$1.2 - 25$	> 12		
	$K^{\pm}$							< 25	> 12		
	p n		< 9.9					$9.5 - 25$	> 12		
	$\bar{p}$ $\bar{n}$ Λ						> 20	< 25			
QGSC_BERT	$\pi^{\pm}$ $K^{\pm}$ p n	< 9								> 6	
	$\bar{p}$ $\bar{n}$ Λ						> 20	< 25			
QGSC_CHIPS/QGSC†	all			†						all	
QGSP_BERT	$\pi^{\pm}$ $K^{\pm}$ p n	< 9.9						$9.5 - 25$			> 12
	$\bar{p}$ $\bar{n}$ Λ						> 20	< 25			
QGSP_BERT_NOLEP	$\pi^{\pm}$ $K^{\pm}$ p n	< 9.9									> 8.5
	$\bar{p}$ $\bar{n}$ Λ						> 20	< 25			
QGSP_BERT_TRV	$\pi^{\pm}$ $K^{\pm}$ p n	< 9.9						$9.5 - 15$			> 10
	$\bar{p}$ $\bar{n}$ Λ						> 20	< 25			
QGSP_FTFP_BERT	$\pi^{\pm}$ $K^{\pm}$ p n	< 8				$6 - 25$					> 12
	$\bar{p}$ $\bar{n}$ Λ						> 20	< 25			

† *The physics lists QGSC_QGSC and QGSC_CHIPS are predecessors of the recently developed CHIPS physics lists. The QGS string model is used with interface to CHIPS over the full energy range. The QGSC variant still uses LHEP models for the radioactive capture and fission. The CHIPS variant uses native CHIPS for proton nucleus reactions below 290 MeV.*

Table 6.1: Composition of the studied physics lists for different hadronic projectiles. The energy range is given in GeV when a model is contained in the physics list. The table is compiled from the output of the Geant4 program.

6.2 Modelling of the Test-Beam Experiment

It is important to model the particle beam and the detectors with sufficient accuracy to obtain meaningful Monte Carlo predictions. This section gives an overview of the different steps used to simulate a realistic beam distribution and detector response. Some steps have been reviewed for this work and are explained in more detail.

6.2.1 Beam Modelling

The beam-line is implemented in the geometrical model of Mokka/Geant4 from the entrance window of the Cherenkov counter downstream. All trigger scintillator counters, drift chambers, vacuum pipes including their beam windows, and air sections are implemented using the dimensions from figure 5.1. Also, the Cherenkov gas volume is simulated with the pressure and gas type used. It was necessary to extend the used Mokka version 7.02, to allow the adjustment of the Cherenkov properties. The changes will be available in future Mokka versions.

Particles are simulated using the Geant4 particle gun placed in front of the Cherenkov entrance window at $z = -38.64\,\mathrm{m}$. This choice is better than the earlier convention to put the gun 60 metres upstream of the experimental area, as the vacuum pipe in front of the Cherenkov is not included in the beam line modelling. In the latter case, the beam would undergo significant more multiple scattering in the simulation than in reality. Figure 6.3(a) shows the simulated position distribution at the last drift chamber for the old and the new particle gun position. The position distribution originates solely from multiple scattering, as a point-like 20 GeV pion source was used. The size of multiple scattering depends on the beam momentum. Figure 6.3(b) shows the width of the multiple scattering distribution σ_{MS} for the energies studied in this work. The particle momentum and a Gaussian momentum spread of the particle source are calculated from the magnet currents and collimator openings using equations 5.1 and 5.3.

The beam position distribution is simulated using a Gaussian position smearing at the particle gun. No angular smearing is simulated, assuming that the angular distribution at the detector is dominated by multiple scattering in the downstream beam-line. To calculate the mean gun position and the width of the Gaussian distribution, the drift chamber profiles are fitted for each data run. The broadening due to multiple scattering is simulated with a point source and subtracted from the measured profile. Studies have shown that the exact beam profile has almost no impact on the simulation results [52, 53]. Therefore, it is assumed that the bias from the drift chamber reconstruction and the non-Gaussian drift chamber profiles will not lead to a significant bias of the simulation.

The trigger acceptance is simulated by checking that the beam particle has deposited energy in the corresponding scintillator counters. No further digitisation is used for the trigger system.

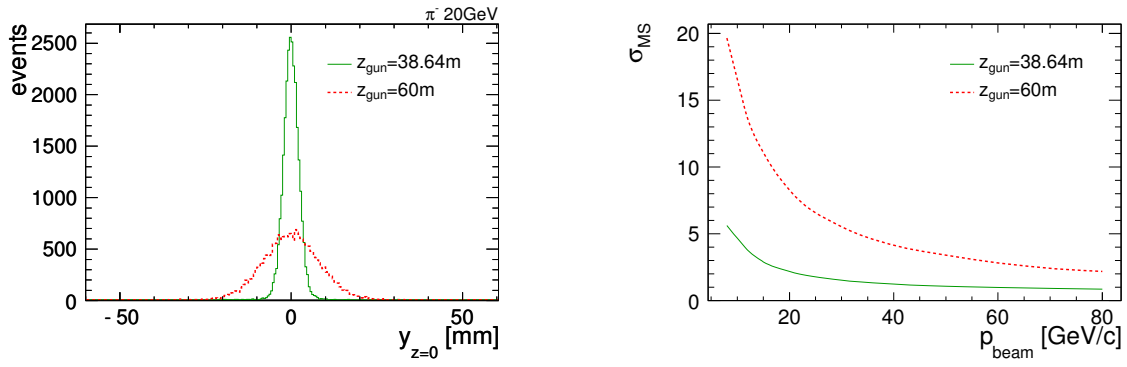

(a) (b)

Figure 6.3: Simulated beam width at the drift chambers for point like particle sources at the old and the new particle gun position. 20 GeV pions are simulated from two positions, $z = 38.64\,\mathrm{m}$ and $z = 60\,\mathrm{m}$. Unrealistic multiple scattering is simulated in case of $z = 60\,\mathrm{m}$, due to a missing vacuum pipe in front of the Cherenkov in the simulation model.

6.2.2 Detector Modelling

All CALICE detectors are modelled in Mokka[1] [38, 39], and specialised routines for the digitisation of the ECAL, AHCAL, and TCMT exist. This section describes the modelling and digitisation of the AHCAL. A digitisation procedure following the same basic ideas exists for the TCMT, which is used in the later analysis for event identification. Its implementation is not as advanced as the AHCAL digitisation, but is expected to be sufficiently accurate for the purpose of this work.

Material Budget and Composition

First of all, the detector model has to describe the material budget and the composition of the detector. The AHCAL detector geometry is implemented in Mokka. A careful review of the implementation has been performed during this work. Several improvements of the detector description were achieved. The thickness of the cassette covers and the absorber plates have been remeasured and the simulation is adjusted to more realistic values. Likewise, the thickness of the scintillator tiles is confirmed in the measurement of a small random sample. The air gaps between absorber plates and readout modules are adjusted such that the measured total detector length is reproduced. Additionally, the description of the detector rotation is revised. A detailed description of the current Mokka implementation of the AHCAL can be found in [54]. In this work the AHCAL geometrical description as in Mokka version 7.02 is used.

[1] Mokka is a Linear Collider simulation software based on the Geant4 toolkit. It includes the detector models for full detector and test-beam simulations.

Saturation Effects in Plastic Scintillators – Birks' Law

The scintillation process saturates for high ionisation densities, due to shielding effects in the scintillator material. Especially in plastic scintillators, this effect is sizable. The Geant4 implementation of Birks' Law [55] is used to model this effect. This implementation bases on the assumption that the scintillation light output $\frac{\mathrm{d}S}{\mathrm{d}r}$ can be expressed as

$$\frac{\mathrm{d}S}{\mathrm{d}r} \propto \frac{\mathrm{d}E}{\mathrm{d}x} \cdot \frac{1}{1 + k_{\mathrm{B}} \cdot \frac{\mathrm{d}E}{\mathrm{d}x}}, \tag{6.1}$$

where $\frac{\mathrm{d}E}{\mathrm{d}x}$ is the ionisation density. The parameter k_{B} depends on the scintillator material. In the case of the AHCAL, the value for polystyrene ($0.00842\,\mathrm{gcm}^{-2}\mathrm{MeV}^{-1}$) is taken from [56].

Time Acceptance of the Readout Electronics

The acceptance of the electronics is limited in time. This is due to the choice of track and hold together with a shaping of the electronic signal. The hold is optimised to give the highest response for prompt signals at t_0. As hadronic showers contain particles from nuclear de-excitation processes and thermal neutrons, the signal exhibits a long tail in time. Depending on the arrival time, such signals will experience a reduced electronics gain or will not be recorded at all. A readout electronics' effective acceptance time t_{cut} of 150 ns was calculated from the form of the shaped output signal.

The signal shape of the SiPMs can vary for different production series as described in 3.2.3. Such variations of the input signal shape can transfer to variations in the output signal shape. Measurements of the optimal hold time give a maximum variation of the peak position of 15 nanoseconds. The influence of such variations has been studied by looking at the time distribution of the energy deposits in the simulation. Figure 6.4(a) displays this distribution for 20 GeV pions. Most energy is deposited within a few tens of nanoseconds. Figure 6.4(b) shows that the fraction of the signal before t_{cut} changes only slightly with the cut, leaving only a few per mill uncertainty on the reconstructed energy.

Technically, the time cut is already applied inside Mokka. This is necessary in order to allow an efficient output file format which stores only the total energy per Mokka cell and event.

Digitisation

The output of Mokka is the deposited energy in the active volume, the scintillator, subdivided into logical volumes of one square centimetre. The digitisation transfers this output in several steps into signals equivalent to raw data. The digitised simulation can be used as input to the reconstruction chain, like raw data. The single steps are:

1. **Ganging:** The simulation is performed with cells of one square centimetre size. These small cells have to be combined to the three cell sizes of the AHCAL. This is done in the ganging step.

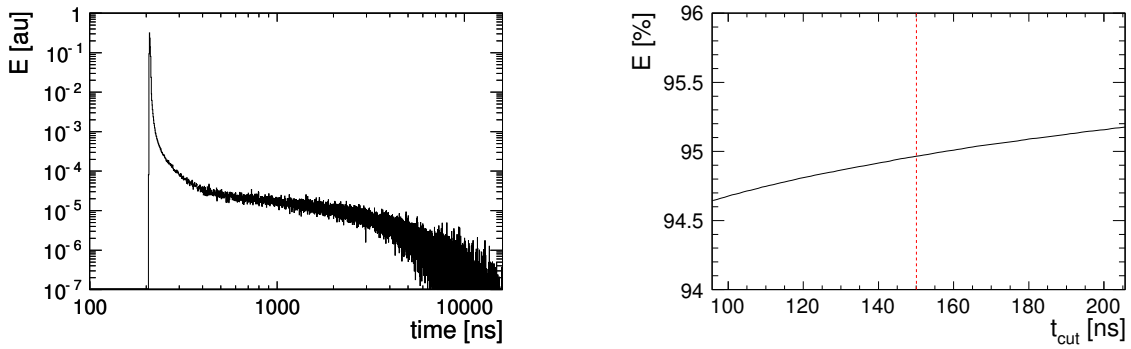

(a) (b)

Figure 6.4: (a) Time distribution of the energy deposits in 20 GeV pion showers. (b) Fraction of the total reconstructed energy versus time cut t_{cut}. The red dotted line corresponds to the electronics time cut.

2. **Light crosstalk:** The borders of the tiles are not fully reflective. This effect is simulated by transferring a total of 10 % of the deposited energy to the neighbouring tiles. The energy is distributed according to the fraction of circumference the neighbour connects to.

3. **Scale matching between simulation and measurement:** The result of the simulation is given as absolute energy deposition E in the scintillator. It is necessary to match this scale to the scale of the detector calibration. To achieve this the energy is expressed in multiples of the energy deposition of a minimum ionising particle. The most probable value of the energy deposition of simulated muons M_{sim} is fitted and the amplitude in units of MIP is calculated: $A_{\text{MIP}} = \frac{E}{M_{\text{sim}}}$

4. **SiPM non-linearity:** The saturation behaviour of the SiPM is simulated using

$$A_{\text{pix}} = f\left(A_{\text{MIP}} \cdot \frac{M \cdot I}{g}\right), \tag{6.2}$$

where f is the scaled fit to the SiPM response using equation 4.4. M, g, and I are the MIP, gain, and inter-calibration values of the cell (see sec. 4.4.1). The unit of the output is pixels.

5. **Statistical fluctuations:** The limited number of pixels leads to significant statistical fluctuations in the signal. This is simulated by randomising A_{pix} with a Poissonian distribution. Afterwards the amplitude is transferred to the scale of the readout electronics: $A_{\text{ADC}} = A_{\text{pix}} \cdot \frac{g}{I}$.

6. **Noise:** The noise of the SiPM and the readout system is added to the signal of the cell. This is achieved by adding the pedestal subtracted amplitude of random trigger events to the amplitude of the cell. The random trigger events are taken from the same run that is simulated.

During digitisation, the calibration values of MIP and gain are extrapolated to the temperature of the measurement, as done in the reconstruction.

Systematic Errors

The digitisation uses inversions of the same formulae used in the reconstruction. Also, the calibration values are identical between reconstruction and digitisation. Therefore, all systematic errors described in section 4.4.5 are cancelled after the digitised simulation is reconstructed. Practically, this means that the simulation does not contain systematic errors from the calibration procedure but the data does. Accordingly, the calibration systematics have to be taken into account exactly once when comparing simulation and measurement.

The simulation has other uncertainties, which are relevant for the comparison of simulation and measurement:

- The modelling of material budget and composition has some uncertainty. The thickness of several AHCAL components was re-measured and updated during this work, to minimise eventual uncertainties.
- The matching of the scales of simulation and measurement depends on how realistic the simulation of muons is. It is assumed that this method is accurate within one percent.
- Pure beams are simulated but the real beam is not perfectly pure. The spectrum of primary particles and the methods to purify beams are described in section 5.2.1. Additionally, the Cherenkov counter is used to further purify the sample during the analysis. Currently, no description of the remaining uncertainty exists.

6.3 Validation of the Detector Modelling and the Systematic Error Assumptions

The systematic uncertainties of the reconstruction and the simulation are discussed in sections 4.4.5 and 6.2.2. It is necessary to check these assumptions before the measurements can be used to test the quality of the different hadron simulation models. Electromagnetic showers are a good probe for such comparisons from the aspect of simulation. The electromagnetic processes are well understood on the relevant scales, and can be simulated with sufficient accuracy. This advantage is partly lost due to the special challenge of measuring electromagnetic showers in the AHCAL, as described in section 4.4.5. Nevertheless, it is chosen for this work to validate the assumptions.

A set of $e^{\pm}$ runs taken in-between the hadron runs is selected for this analysis. This ensures that the detector configuration and environmental conditions are practically the same for the hadron and the electron runs. The raw size of the electron runs is around 100000 events. For each run 200000 events are simulated and digitised. The simulated and real data are sent to the same reconstruction chain. The test-beam sample is purified by a cut on the measurements of the TCMT and the Cherenkov. The cuts are described in chapter 7.

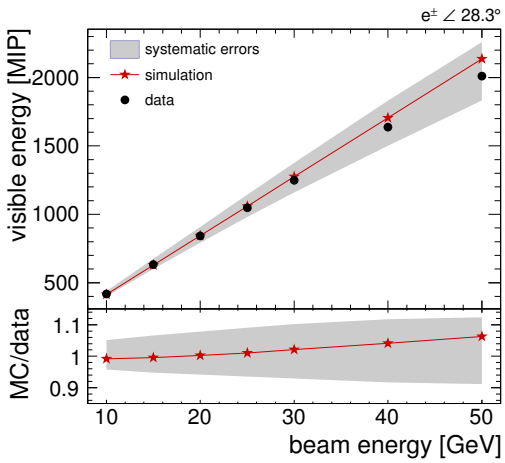

Figure 6.5: Electromagnetic response of the AHCAL versus energy. The visible energy, expressed in MIP, is plotted versus the beam energy. The ratio of simulation over data is shown in the lower frame.

The systematic errors have a different impact on integrated and differential measurements. The details are discussed in section 4.4.5. The main observables in the hadron analysis are the reconstructed energy and the shape of the hadron profiles. Accordingly, the total energy and electromagnetic shower profiles are chosen for comparison.

6.3.1 Integrated Variables – Energy Sum

Figure 6.5 shows the response of the AHCAL to electron and positron beams with varying energy. The visible energy measured in the test-beam is compared to the predicted visible energy. The systematic error combines the calibration and the scale matching uncertainties. The complete systematic uncertainty is assigned to the data points, for the sake of clarity. The ratio of simulation over data is drawn in the lower frame. For all tested energies, the differences between measurement and simulation are well inside the assumed systematic uncertainties.

6.3.2 Differential Variables – Shower Profile

Figure 6.6 displays the profiles of electromagnetic showers for two different beam energies. The simulation describes the measurement within the systematic errors for most of the peak region and in the late tail region where almost no signal is present. Some differences are visible between layer 10 and 25. The shape of the ratio shown in figure 6.6(a) suggests that the shower starts earlier in simulation than in data. Such an effect can be due to a wrong description of the AHCAL which assumes too much material or too dense materials. Another possible source is the presence of a small fraction of pions in the beam. Pion showers are longer than electromagnetic showers and would stretch the data profile. As the material composition was checked carefully for this work, it is assumed that the latter is the case. In general pion beams are more pure than electron beams. Therefore, it is assumed that this effect will not be present in hadron data.

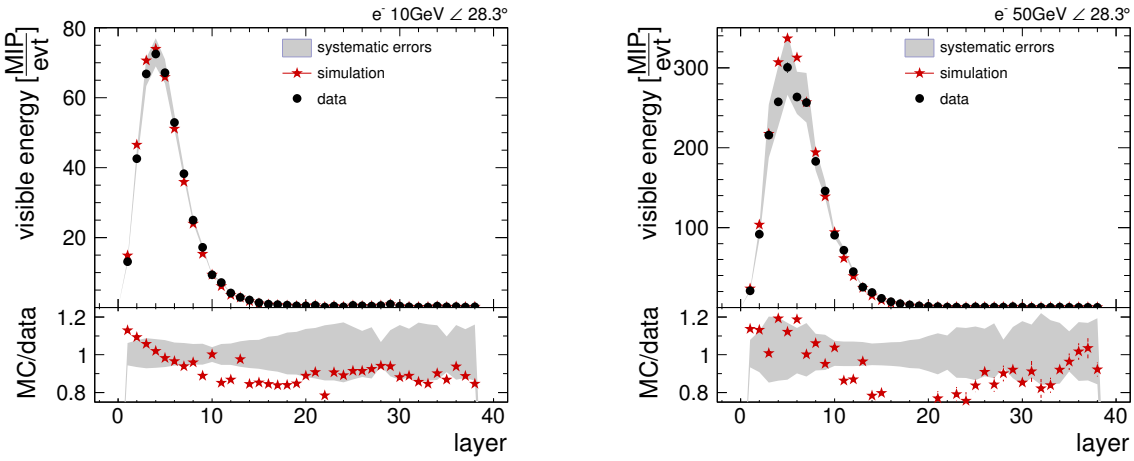

(a) (b)

Figure 6.6: Measured and simulated electromagnetic shower profiles for a 10 GeV beam (a) and a 50 GeV beam (b). The lower frame displays the ratio of simulation over data.

Chapter 7

Event Selection

In a test-beam environment, accelerator generated particle beams are adjusted to the needs of the experimenter. Section 5.2 describes the particle generation and aspects of the beam quality. Although the beams are already quite pure and well defined in position and momentum, it might be necessary to further enhance the quality of the data sample. Different aspects can be relevant depending on the studied effects. An identification of the incoming particle type is the most common selection criterion during the analysis. This chapter describes ways to identify the particle type and to measure event quality properties exploiting the information from the auxiliary detectors and the calorimeters themselves.

7.1 Particle Type

Although the beam-line usually runs in a mode that enriches the content of one particle type, the beam will always be a composition of different particle species. The typically observed particles, including their masses, are listed in table 7.1.

7.1.1 The Cherenkov Counter

The Cherenkov counter is the main device used to select particles of a certain species. Cherenkov light is produced when the particle moves faster than the speed of light inside a medium. This is the case if

$$\beta > \frac{1}{n}, \tag{7.1}$$

where $\beta = \frac{p}{E}$ is the velocity of the particle and n is the refraction index of the medium. The light is radiated at a specific angle Θ, given by

$$\cos\Theta = \frac{1}{n\beta}. \tag{7.2}$$

particle	electron	muon	pion	kaon	proton
symbol	e	μ	π	K	p
mass $\left[\frac{\text{MeV}}{c^2}\right]$	0.511	106	140	494	938

Table 7.1: Typically observed particles at the CERN test-beam and their masses.

This offers two approaches to differentiate particles with same momentum but different mass. One can either measure the Cherenkov angle Θ, or choose the radiator material such that not all particle species move faster than the speed of light in the medium. The CALICE test-beam setup at CERN used a threshold Cherenkov counter which exploits the second principle. The particles pass through a gaseous radiator medium. The speed of light inside the radiator can be adjusted by the gas pressure. Pressure curves and detection efficiencies for different particle types are shown in section 5.1.4.

The meaning of a positive or negative Cherenkov signal depends on the exact working conditions. Especially, the detection efficiencies have to be considered when interpreting the signal. The produced amount of light increases with the gas pressure and leads to a higher detection probability of the signal. But, the pressure is limited as it cannot be increased above the threshold of the heavier particle. Two cases are discussed here, the separation of electrons and pions, and the separation of pions and protons.

e/π-Separation

The Cherenkov counter is filled with helium gas and the pressure is set just below the pion threshold. Electrons and muons can generate Cherenkov light under this condition. The detection efficiency for electrons is nearly 100 % up to particle momenta of 20 GeV and drops down for higher energies.

Electrons can be selected using the Cherenkov ON signal. Pions and heavier particles will be removed from the sample. Also the muons will be suppressed but not fully, as these are above threshold but have a bad detection efficiency. At higher energies a lot of good electron events will fail the selection due to the low detection efficiency of the Cherenkov.

The pion content is enhanced by requiring the Cherenkov signal off. The purity of this selection depends on the electron detection efficiency and the initial electron admixture. A quantification of the effective electron detection efficiency would be necessary to use this selection.

π/p-Separation

The Cherenkov counter is filled with nitrogen gas to extend the Cherenkov operation range to lower energies. The pressure is set to the proton threshold. Electrons do not generate detectable signals with this gas filling. Muons, pions and kaons are above the Cherenkov threshold and generate light. The detection efficiencies for muons, pions and kaons are nearly 100 % for most of the energy range.

Protons can be selected by requiring no detected Cherenkov signal. The remaining contamination with lighter particles depends on the practically achieved detection efficiencies for these particles.

The rejection of protons by requiring an active Cherenkov signal is more efficient than the proton selection. But a possible side effect is a change of the relative fractions of the lighter particles, due to different detection efficiencies.

7.1.2 Calorimeter Based Identification

Cherenkov counters identify particles by their masses. Another possibility is to identify the particle type by the kind of interactions these undergo. The CALICE calorimeters qualify for such kind of particle identification due to the fine spatial granularity of the readout. A visual example of the different signatures is given in figure 7.1.

Minimum ionising particles are visible as a track of cells near the signal threshold, as depicted in figure 7.2(a). Electromagnetic showers are dense and compact, and start directly in the first layer of the calorimeter. Figure 7.2(b) shows the case of a 30 GeV electron. Hadrons can travel a significant distance as minimum ionising particle through the detector before a hadron shower is initiated. Figure 7.2(c) gives such an example.

The largest benefit in the usage of the calorimeters lies in the identification of muons. The Cherenkov usually differentiates already efficiently between electrons and pions. At the same time, hadron showers with a high electromagnetic content cannot be distinguished from electromagnetic showers using the shower shape. For all energies recorded at CERN, cuts on the energy sum and the number of hits inside the detectors are an economic way to reject muons. Nevertheless, the conducted research can require a more sophisticated method. An example is the leakage analysis included in this work. A cut on the TCMT alone is desired, as the AHCAL signal is the subject of the studies and the ECAL is not present. But, a simple cut on the TCMT energy would bias the reconstructed energy distribution of the AHCAL, as moderate leakage can have the same energy sum and number of hits as a muon. A method to avoid this problem is necessary.

Muon Identification with the TCMT

Typically, a muon travels through the complete TCMT leaving signals following a characteristic energy distribution in consecutive cells. This gives the possibility to identify muons using the visible energy, number of hits, and the geometry of the signal. The available geometrical information is given by the detector layout, which is described in section 5.1.2. A cut based muon identification is described here. The following observables are chosen to discriminate muons from different signals:

E_{vis} The sum of the visible energy.

N_{hits} The number cells with signals higher than 0.5 MIP.

N_{layer} The number of layers which have E_{vis} and N_{hits} compatible with a muon signal.

N_{tower} The number of towers of consecutively hit strips.

The usage of strips restricts the position information for a single hit to two dimensions, either x and z, or y and z. Therefore, N_{tower} is calculated for both strip orientations separately. Then the results from both orientations are summed.

Samples of reasonably pure pedestal, muon, and hadron events are necessary to calibrate the thresholds of the single observables. To simplify the selection procedure, data without ECAL is chosen. Random trigger events give the pedestal distributions. The muon selection is based on the AHCAL signal only. A simple cut on E_{vis} and N_{hits} is sufficient to select muons with good enough purity for the calibration, when the muon content in

(a)

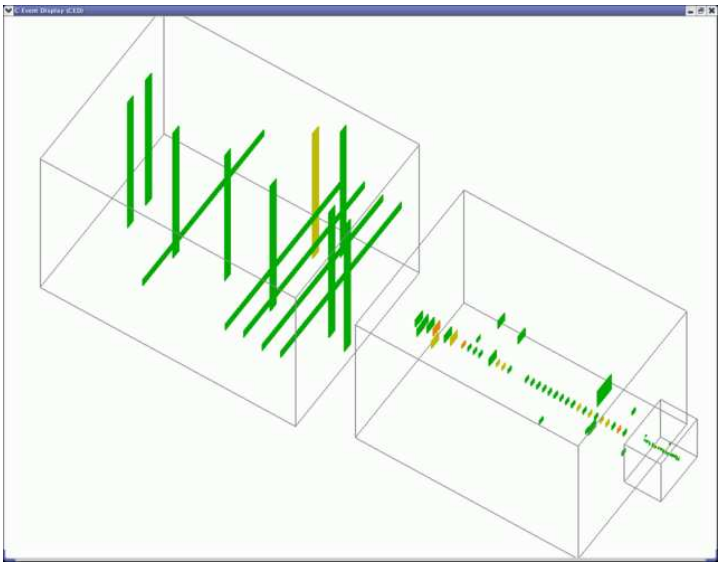

(b)

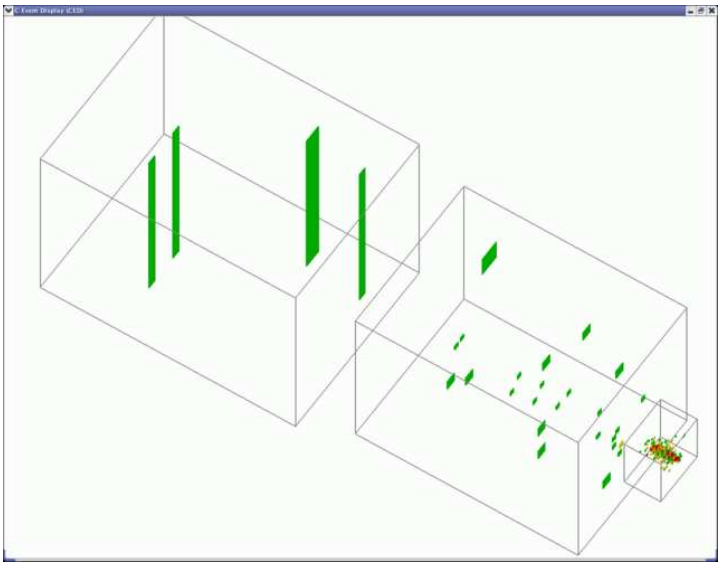

(c)

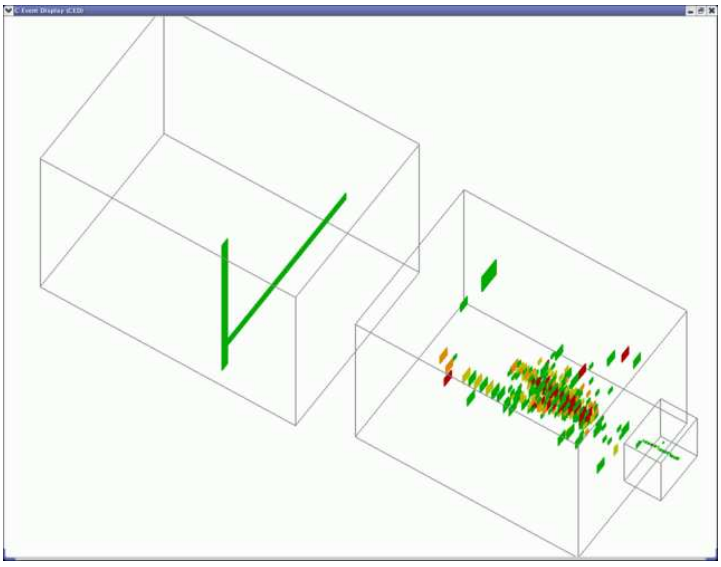

Figure 7.1:
Signatures of different particles in the CALICE calorimeters:
(a) Minimum ionising particle: Muon of 30 GeV passing the calorimeters.
(b) Electromagnetic shower: 30 GeV electron recorded in the ECAL.
(c) Hadron shower: 30 GeV pion passes the ECAL minimal ionising and showers in the AHCAL

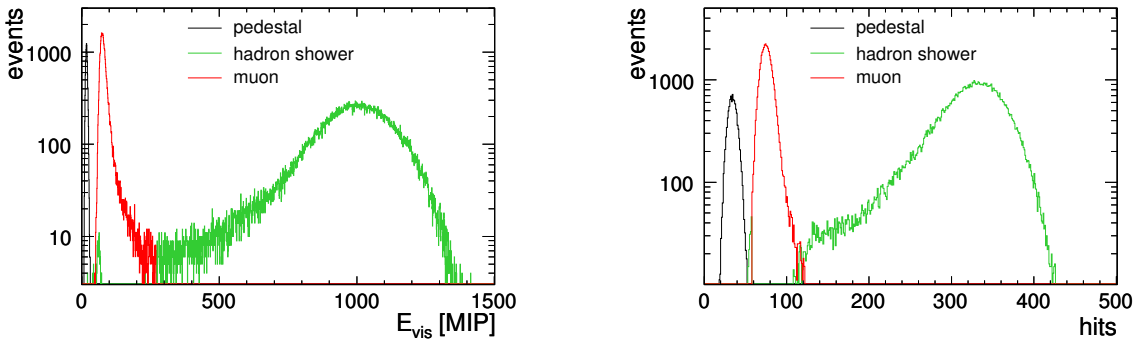

(d) (e)

Figure 7.2: The AHCAL energy sum (a) and the number of hits (b) for pedestal, muon, and shower events. See text for further explanation.

the run is not too small. Therefore, a 30 GeV hadron run is selected for the calibration, as the CERN beam contains approximately 30 % muons at this energy and the muon signal is well distinguishable from the hadron events. Figure 7.2 depicts the distributions of E_{vis} and N_{hits} inside the AHCAL for the different event types. The contamination with punch through hadron events inside the muon sample is smaller than 3 %.

The cut thresholds are optimised for the selected observables using the AHCAL selected event samples. The probability distributions of all TCMT observables are generated for the three AHCAL event types, namely pedestal events, muon events, and hadron shower events. Then the cut thresholds are placed at the points where the probabilities become equal. Figure 7.3(a) illustrates the procedure for the visible energy sum. The visible energy sum is smaller for pedestal events than for muon events, thus a minimum energy is required to reject events that have no signal in the TCMT. Most hadron showers are contained in the AHCAL and give no or a small signal in the TCMT. Muons give a signal which is practically always larger than a certain value. The crossing point between the pedestal and the muon signal probability is used as minimum required energy E_{min}. However, some hadron showers have sizable leakage into the TCMT. The point where the TCMT signal is more likely from a leaking hadron event than from a muon event is chosen as upper energy cut E_{max}. The thresholds for the number of towers N_{tower} are obtained similarly. Figure 7.3(b) depicts the corresponding distributions and thresholds.

The cut on the energy sum is a good illustration of the conflict between muon identification and hadron energy leakage measurement. The cut efficiently identifies muons. But, a large fraction of the hadron events with leakage is removed from the sample at the same time. The purity and the efficiency are measured to quantify the quality of the selection. The purity can be calculated from the number of hadron shower events that are identified as muon events inside the TCMT. The efficiency can be directly measured with muon beams. Figure 7.4 compares the results from the newly developed, complex method to a simple cut on the TCMT energy and hits. The complex method shows a much better purity and less energy dependence than the simple method, whereas the simple method is

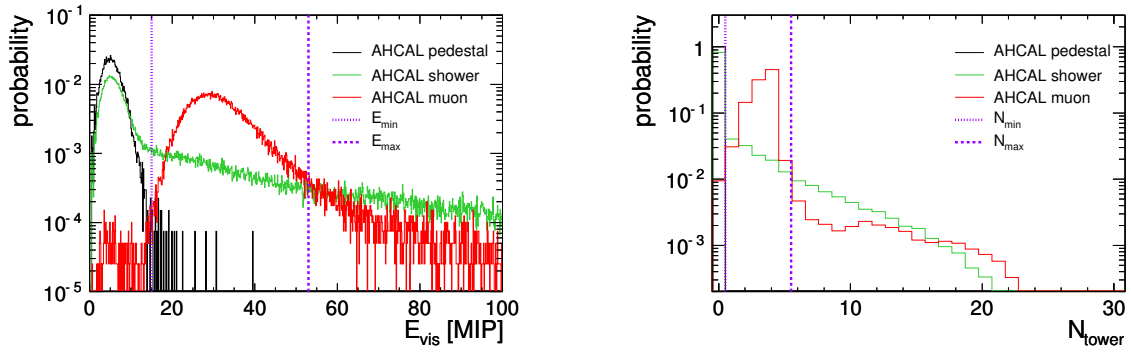

(a) (b)

Figure 7.3: The TCMT signal for different AHCAL event types. The TCMT energy sum (a) and the number of muon like towers (b) are shown, including the chosen thresholds.

superior in efficiency.

7.2 Event Multiplicity

The calorimeter is hit by more than one particle for a small fraction of the beam events. This can have to reasons: Either more than one particle is generated and transported to the experiment, or the particle interacts on the way to the detector. In the first case, two particles with same energy and initial direction have to be generated simultaneously. At CERN, this happens only rarely, but such events can be observed with high enough statistics. More frequently, a particle interacts with some material of the beam-line and generates secondary particles. If this happens after the last momentum selection, these particles can reach the detector. The amount of such events depends on the particle type and the beam energy.

The effect on the detected signal is different in the two situations. A multiple of the beam energy is registered by the detector, in the case of multiple primary particles. In the other case, the momentum of the impact particle is not well defined and can be significantly lower than the chosen beam momentum. This is especially problematic when leakage is studied.

The CALICE test-beam installation includes an analogue readout of one of the scintillation counters. This can be used to identify events with more than one charged particle travelling to the detectors. The calibration and performance of this detector is described in this section.

7.2.1 Calibration

Single particles pass through the multiplicity counter in the vast majority of the recorded beam events. This and the high signal to noise ratio allow the multiplicity counter to be

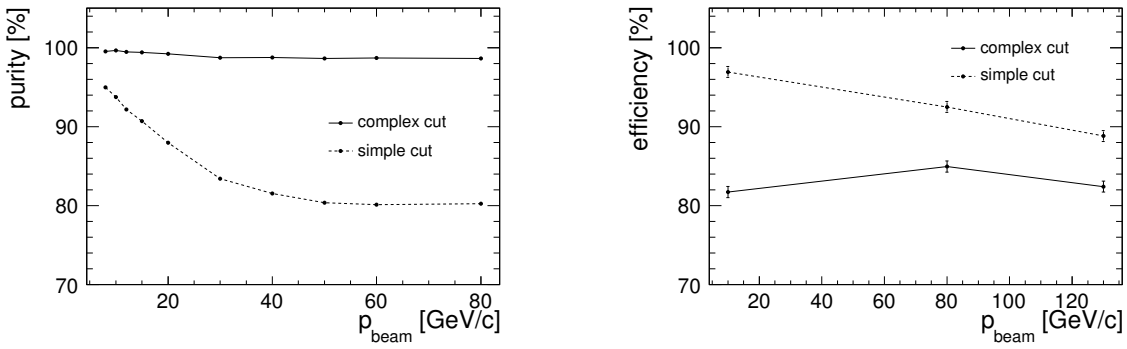

(a) (b)

Figure 7.4: Study of the different muon detection methods based on the TCMT signal. (a) The muon detection purity. (b) The muon detection efficiency.

calibrated on single runs. The particles have a sufficiently large momentum to be described as minimum ionising particles.

The energy deposition in thin materials follows a Landau distribution. The Landau distribution $L(x)$ is smeared with a Gaussian distribution $G(x)$, due to the electronics noise and the photon detection fluctuations. Additionally, the scintillator is with 16 mm already too thick to be fully modelled by a thin layer approach. Therefore, a Landau convolved with a Gaussian distribution was chosen to describe the signal. Equation 7.3 fits the measured distribution well. To avoid a bias, the range of the fit is restricted to the region with no significant contribution from double particle events.

$$f(x) = L(x) \otimes G(x) \tag{7.3}$$

$$a(x) \otimes b(x) = \int a(x-\tau) \cdot b(\tau) \mathrm{d}\tau \tag{7.4}$$

The fit is performed using the ROOT software framework [57], which includes the MINUIT minimisation package [58]. The framework is extended with a generic class to allow the convolution of arbitrary functions. The convolution is calculated with a numerical integration of equation 7.4. The implementations of Landau and Gaussian distributions inside the ROOT framework are used.

Figure 7.5(a) shows the raw measurement of the multiplicity counter amplitude and pedestal. The result of the fit is drawn as a blue line. Excesses over the fitted functions originate from two and three particle events. The pedestal is measured with random triggers identical to the pedestal of the AHCAL cells.

A threshold on the multiplicity amplitude can be used to reject two and more particle events. The threshold should be as high as possible to avoid an unnecessary rejection of good events in the Landau tail of the distribution. A good knowledge of the signal distribution of double particle events is necessary to calculate the threshold to reject these

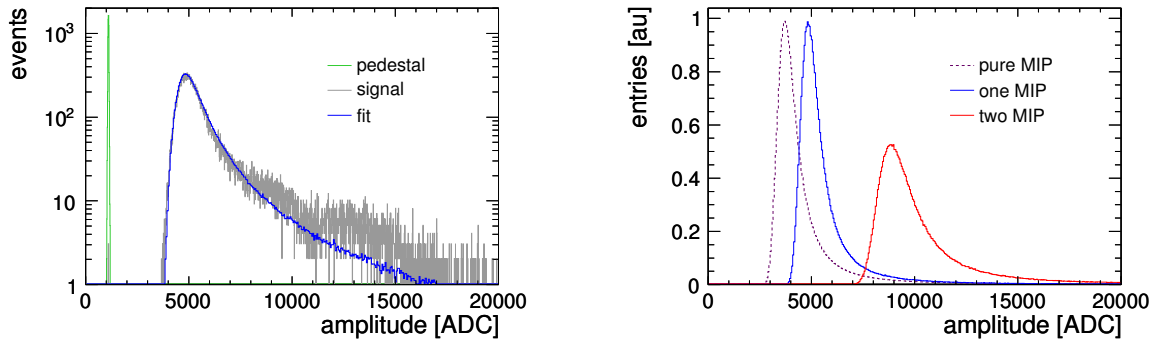

(a) (b)

Figure 7.5: (a) Signal of the particle multiplicity trigger for a 30 GeV e^+ beam. A convolution of a Landau- with a Gaussian-distribution is used to describe the signal. The fit result is shown as a light blue line. Double and triple particle events are visible as excess over the fit. (b) Histograms used for the calibration of the multiplicity counter. See the text for more details.

events. A direct measurement of the distribution is not feasible, considering the small number of double particle events in the region of the Landau tail. Alternatively, the distribution of double particles can be calculated from the distribution of a single particle.

Equations 7.5 and 7.6 give the signal composition in the case of one and two minimum ionising particles, respectively. The distribution of A_1 is known from the fit.

$$A_1 = A_{\mathrm{MIP}} + A_{\mathrm{ped}} \tag{7.5}$$

$$A_2 = A_{\mathrm{MIP}} + A_{\mathrm{MIP}} + A_{\mathrm{ped}} \tag{7.6}$$

The distribution of the pedestal A_{ped} is Gaussian and can be measured with the help of random trigger events. The distribution f_{MIP} of A_{MIP} can be calculated. The mean m_{MIP} and Gaussian width σ_{MIP} are given by:

$$m_{\mathrm{MIP}} = m_{\mathrm{fit}} - m_{\mathrm{ped}}, \tag{7.7}$$

$$\sigma_{\mathrm{MIP}} = \sqrt{\sigma^2_{\mathrm{fit}} - \sigma^2_{\mathrm{ped}}}. \tag{7.8}$$

Note that convolutions factorise and that the convolution of two Gaussian distributions with widths σ_1 and σ_2 is a Gaussian distribution with width $\sigma^2 = \sigma_1^2 + \sigma_2^2$.

Now, the distribution f_2 of two minimum ionising particles can be generated by adding two randomly selected amplitudes of A_{MIP} and a randomly selected pedestal value A_{ped} (equation 7.6). The resulting distribution of A_2 is drawn in figure 7.5(b). Additionally, The figure shows the bare distribution of the minimum ionising particle, A_{MIP}, and an equally generated distribution of A_1.

The threshold t is calculated by numerically solving equation 7.9, where p is the desired rejection purity

$$p = \frac{\int_t^\infty f_2(x)\mathrm{d}x}{\int_{-\infty}^\infty f_2(x)\mathrm{d}x}, \tag{7.9}$$

and $f_2(x)$ is the calculated distribution of two minimum ionising particles.

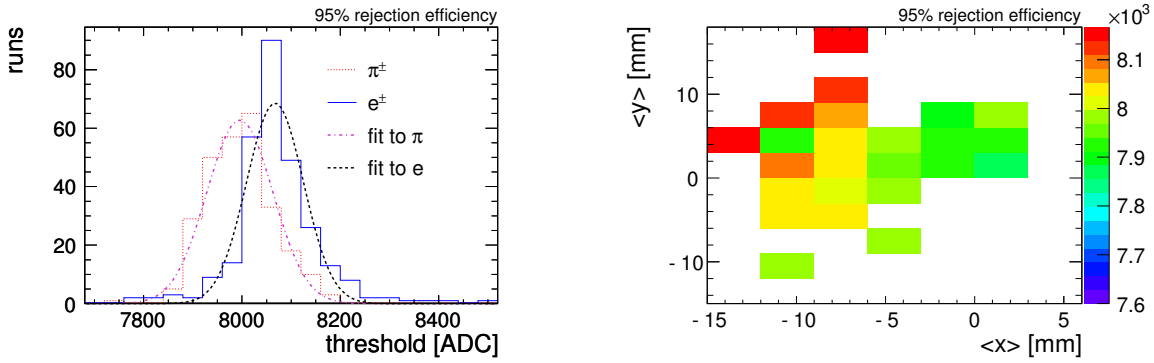

(a) (b)

Figure 7.6: (a) Threshold for rejection of 95 % of double particle events. The threshold differs for electrons and pions. (b) Threshold versus mean beam position in the drift chambers.

7.2.2 Results and Systematics

The multiplicity thresholds for 90 %, 95 %, 99 %, and 99.9 % rejection efficiency are determined for all CERN beam runs. Electrons give a slightly higher threshold than pions, due to the higher $\frac{\mathrm{d}E}{\mathrm{d}x}$. Figure 7.6(a) shows the distribution of measured thresholds for 95 % rejection efficiency.

Careful checks are performed to identify eventual systematic correlations between the threshold and ambient temperature, beam momentum, fraction of multiple particle events, and beam position. The largest contribution to the systematic error originates from a position sensitive light collection efficiency in the scintillator. The photomultiplier is mounted on one of the scintillator corners. It is found that the mean threshold gets larger the closer the mean beam position is. This is illustrated in figure 7.6(b). The maximum size of the effect is 5 %. This correlation propagates to a beam momentum dependence of the threshold, as the beam size is correlated to the beam energy. No other systematic dependencies larger than 1 % are observed. The total systematic uncertainty of the threshold is estimated to be 2 %, when individual calibrations are used for each run.

Chapter 8

Hadron Shower Measurements

A comprehensive collection of data was recorded during the CALICE CERN 2007 test-beam campaign, covering different energies, particle types, and detector configurations. This work comprises studies with pion beams in the energy range from 8 GeV to 80 GeV. A set of runs which were recorded without ECAL in front of the AHCAL is chosen to achieve high statistics and reduce the selection and energy uncertainties in the analysis. Furthermore, runs are selected where the beam hits the detector centrally to achieve a good radial symmetry. The only data set fulfilling all the requirements is taken with a detector configuration of 28.3 degrees (see figure 8.6). This set also has the advantage that it comes from a period of stable detector running.

The high granularity of the AHCAL allows new approaches to be used to study hadron showers. This chapter includes the description of the methods chosen for this work and the results obtained with data. Section 8.1 describes a method to identify the position of the first hard interaction inside a hadron shower. It is followed by a discussion of the measurement of hadron profiles with rotated detector geometries in section 8.2. Finally, a method to measure and correct for longitudinal leakage is introduced in section 8.3.

The described methods also build the basis for the comparison of data to the different simulation models, which are described in chapter 9.

8.1 Identification of the First Hard Interaction

Unlike electrons and photons, which start to shower practically always within the first layer of the AHCAL, hadrons can travel a significant distance before a shower develops. The average distance a hadron travels before it undergoes a hadronic interaction, which typically starts the cascade of the shower, is called nuclear interaction length λ_I.

The measurement of the position of the first hadron interaction allows the fluctuations of the shower start and the fluctuations in the hadronic cascade to be disentangled.

8.1.1 Definition

Generally, the shower start can be defined as the position of the first hard interaction a hadron undergoes in the detector. As the detector is not directly sensitive to the type of

the interaction that led to a signal, a definition based on the shape of the signal in the detector has to be found.

While neutral hadrons do not lose energy before interacting via the strong force, charged particles lose already some energy before showering and leave a signal in the detector due to ionisation and knock-on electrons. Additionally, the noise of the detector gives a certain amount of signal superimposed on the physics signal. Therefore, a practical method to detect the shower start has to be insensitive to the detector signal originating from a minimum ionising particle plus the detector random noise.

Based on these considerations, an energy deposition that exceeds a certain threshold in energy and spatial size and is nearest to the origin of the particle is defined as the shower start point. The exact algorithm is described in section 8.1.2.

8.1.2 Detection Algorithm

The detection algorithm works in several steps. First, possible regions of interest are identified inside the calorimeter signal. After this, the energy around these regions is collected into clusters. The cluster that fulfils the requirements of both size and shape, and is nearest to the origin of the incoming particle, is considered the shower start cluster. The shower start point is defined as the near end of the cluster main axis seen from the particle origin. This definition allows using the method both in test-beam environment and full size detector.

Identifying Cluster Seeds

The signal of minimum ionising particles follows a characteristic distribution. This distribution is measured during the calibration of the detector. The shape of this distribution is uniform enough for different cells to define a generic energy threshold, which identifies cells that are more likely traversed by more than one charged particle than by a single particle. The calibration of this threshold is described in detail in section 8.2.2.

All cells, where the recorded energy exceeds this threshold, are collected as seeds for the clustering. Before the clustering starts the hits are sorted in ascending z-position to ensure finding the cluster nearest to the origin of the incoming particle first.

Activity Based Clustering

During clustering, all active cells surrounding the seed cell are added to the cluster independent of the signal size in these cells. Therefore, all neighbour cells, typically 9 in front, 8 around and 9 behind the cell, are considered. If one or more of the newly added cells comply with the seed requirements the clustering continues around these cells until only cells below the seed threshold are added.

Selection of Clusters

For each cluster the total energy, the number of active cells and the main axis are calculated. The main axis is defined as the axis with minimum inertia. The calculation is done using the external algorithm from ClusterShapes included in the MarlinUtil [59] package.

The first cluster matching the requirements for all three values is considered the cluster of the shower start. The identification of the best set of thresholds is described in section 8.1.3.

Point of Shower Start

The 3D position of the shower start is defined as the first point on the main principal axis within the cluster.

8.1.3 Optimisation of the Parameters

As described in section 8.1.2, the method provides three observables to identify the shower start: total energy, number of active cells, and direction of the cluster measured as the angle between cluster main axis and beam axis. To achieve the best performance for finding the first hard interaction, the thresholds and limits for these values have to be optimised. This can be done using the shower start finding method on simulated data. The simulation provides the position where the incoming particle ends, which means that it took part in an identity-changing interaction. This position is assumed to be the true shower start and is compared to the result of the shower start finder.

In general it is expected that this optimisation depends on the chosen physics model in the simulation. To achieve the most realistic results, all optimisations have been done on simulation using the QGSP_BERT physics list. This model performed best in the description of showers at the low range of recorded energies, which is the region most challenging for the shower start finder.

For all simulated events where the incoming particle ended within the detector, the following quantities are calculated:

efficiency The efficiency to find a shower start at all.

resolution The RMS90 of the difference between reconstructed and real shower start z-position ($\sigma_{90,z}$), where RMS90 is the root mean square of the range including 90 % of the statistics with minimum root mean square.

offset The mean difference between reconstructed and real shower start z-position (Δz), using the same range as for the resolution.

The thresholds for energy and number of hits are each scanned in 15 steps in the range of 2 to 16 hits for the number of hits and 4 to 32 MIPs for the energy. The direction limit of the cluster is scanned in 9 steps from 5 to 85 degrees. Figure 8.1 shows the results for resolution and offset for an angle limit of 85 degrees.

The scan shows that limiting the cluster angle does not significantly improve the resolution or offset in the z-position, but reduces the efficiency of the method. In contrast to this, the x-y-position resolution can be improved by restricting the angle. In general, the x-y-resolution is at least a factor of two better than the z-resolution, which means that the general position resolution will be dominated by the z-resolution. Therefore, the optimisation is done for energy and number of hits allowing the maximum possible angle.

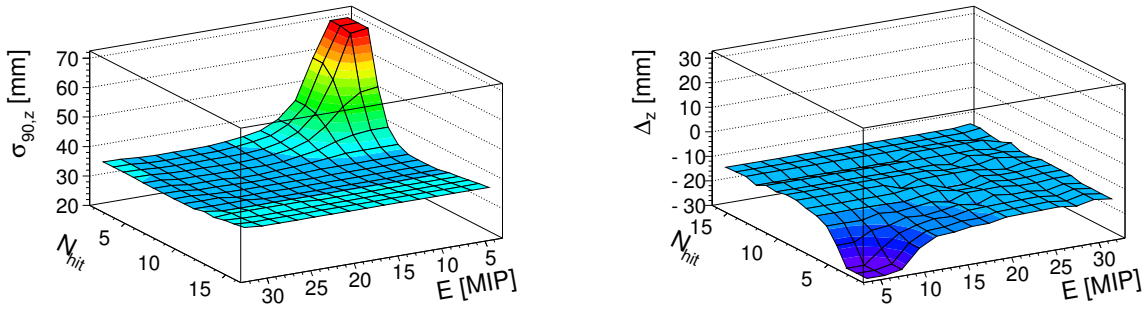

(a) (b)

Figure 8.1: (a) Resolution of the shower start method for simulated 10 GeV π^- and cluster angles up to 85 degrees. (b) Offset for the same data.

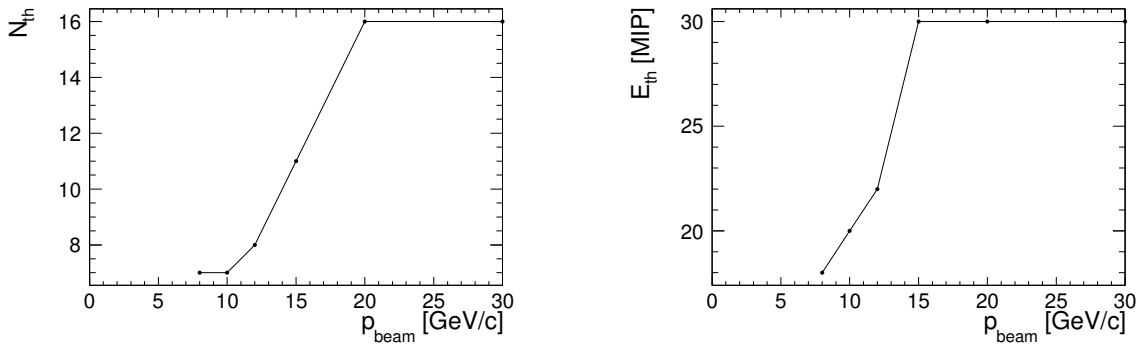

(a) (b)

Figure 8.2: Thresholds for hits (a) and energy (b) that give the best shower start position resolution at a given energy.

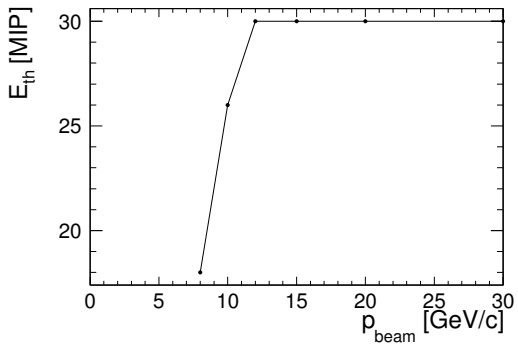

Figure 8.3: Best energy threshold when the hit threshold is fixed to 4 hits.

Depending on the requirements of an analysis using this method, a different optimisation strategy might be more beneficial.

The configuration with the smallest RMS90 is selected for each energy point. Figure 8.2 shows the resulting thresholds for the different energy points. Both the best hit threshold and the best energy threshold increase with beam energy. The thresholds are already at the end of the scan range around 20 GeV beam momentum p_{beam}. This increase of the best threshold combination corresponds to the growing size and density of the shower.

While in the test-beam the energy of the incoming particle is known a priori, in a real detector this is not the case. Accordingly, a single threshold should be chosen for all energies. Additionally, the test-beam prototype of the AHCAL has a different granularity in the last eight layers. This leads to a different number of hits for the same shower shape depending on the start position. Thus, it is preferable to leave the hit threshold as low as possible to achieve a homogeneous response of the method along z. Following these considerations, the energy threshold was optimised while the hit threshold was fixed at 4 hits. Figure 8.3 shows the best energy thresholds when the number of hits is fixed.

The resolution and the offset found with the individually optimised thresholds are displayed in figure 8.4. While the degradation of the resolution for low energies is understandable from the fact that the signal of low energy showers is harder to separate from non-showering particles and detector noise, the minimum around 15 GeV seems to be unphysical. This region corresponds to the energy range where the rather simple parametrised model LEP is used in the simulation. It is more probable that the resolution is at least as large as for high energies.

Figure 8.5 shows the resolution and the offset in the case a fixed hit and energy threshold is used for all beam momenta. It becomes obvious that the energy is a weaker variable to identify the shower start than the number of hits. Still, a reasonable resolution can be achieved over the full range, although the best threshold of the lowest beam energy is used.

As already mentioned, the result of the shower start finding method depends on the physics model chosen in the simulation. For the analysis, a common set of thresholds was used for all physics models. Table 8.1 and table 8.2 summarise the results for the different models.

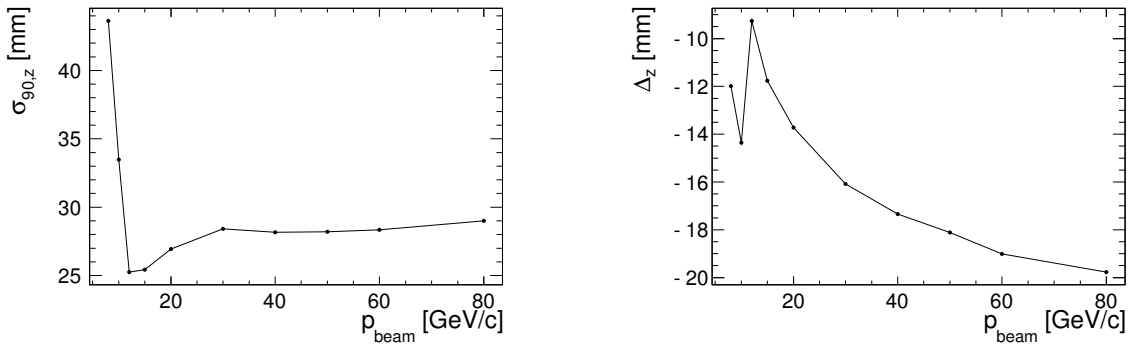

(a) (b)

Figure 8.4: (a) Resolution of the shower start method with the best thresholds for each energy point. (b) Systematic offset in the reconstructed shower start position with the best thresholds for each energy point. Results are based on simulation with the QGSP_BERT physics list.

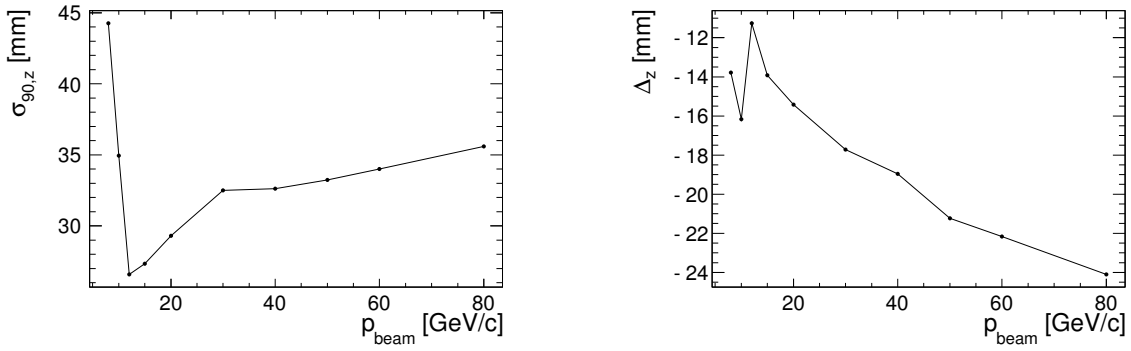

(a) (b)

Figure 8.5: (a) Resolution of the shower start method using global thresholds. (b) Systematic offset of the shower start method using global thresholds. Results are based on simulation with the QGSP_BERT physics list.

physics list	beam momentum [GeV/c]									
	8	10	12	15	20	30	40	50	60	80
CHIPS	-3.3	-4.3	-8.2	-9.8	-12	-15	-16	-17	-18	-20
FTF_BIC	-19	-19	-22	-23	-25	-30	-31	-33	-34	-37
FTFP_BERT	-16	-16	-17	-20	-22	-25	-26	-29	-29	-32
FTFP_BERT_TRV	-16	-16	-17	-20	-23	-26	-27	-29	-29	-31
LHEP	-16	-13	-14	-16	-18	-24	-28	-30	-33	-34
QGS_BIC	-16	-11	-15	-20	-27	-35	-38	-39	-40	-43
QGSC_BERT	-8.7	-22	-24	-25	-26	-30	-31	-32	-34	-36
QGSC_CHIPS	-6.7	-16	-18	-20	-24	-28	-29	-30	-32	-35
QGSC_QGSC	-4.2	-21	-24	-24	-27	-31	-32	-34	-35	-39
QGSP_BERT	-14	-16	-11	-14	-15	-18	-19	-21	-22	-24
QGSP_BERT_NOLEP	-14	-10	-9.7	-11	-15	-17	-20	-21	-21	-23
QGSP_BERT_TRV	-14	-16	-12	-12	-15	-18	-20	-21	-22	-24
QGSP_FTFP_BERT	-16	-16	-17	-18	-18	-18	-21	-21	-22	-24

Table 8.1: Offset between measured and real z-position of the first interaction. All values are in mm. The accuracy of the measurement is better than 0.2 mm for all points and is not displayed for compactness.

physics list	beam momentum [GeV/c]									
	8	10	12	15	20	30	40	50	60	80
CHIPS	39	38	36	35	35	34	34	34	35	36
FTF_BIC	34	33	33	33	33	34	35	35	35	36
FTFP_BERT	31	31	31	31	31	31	32	32	33	34
FTFP_BERT_TRV	33	30	31	31	31	31	32	32	33	34
LHEP	31	28	28	27	28	30	31	32	34	35
QGS_BIC	30	28	28	29	32	36	36	37	38	39
QGSC_BERT	57	40	38	38	38	39	40	41	41	43
QGSC_CHIPS	53	38	37	37	37	38	38	39	39	41
QGSC_QGSC	72	42	39	39	40	41	42	43	44	47
QGSP_BERT	44	35	27	27	29	33	33	33	34	36
QGSP_BERT_NOLEP	44	35	32	32	32	32	33	33	34	35
QGSP_BERT_TRV	44	35	28	31	32	33	33	33	34	35
QGSP_FTFP_BERT	33	30	31	31	32	33	33	33	34	35

Table 8.2: Resolution of the z-position of the first interaction. All values are in mm. The accuracy of the measurement is better than 0.1 mm for all points and is not displayed for compactness.

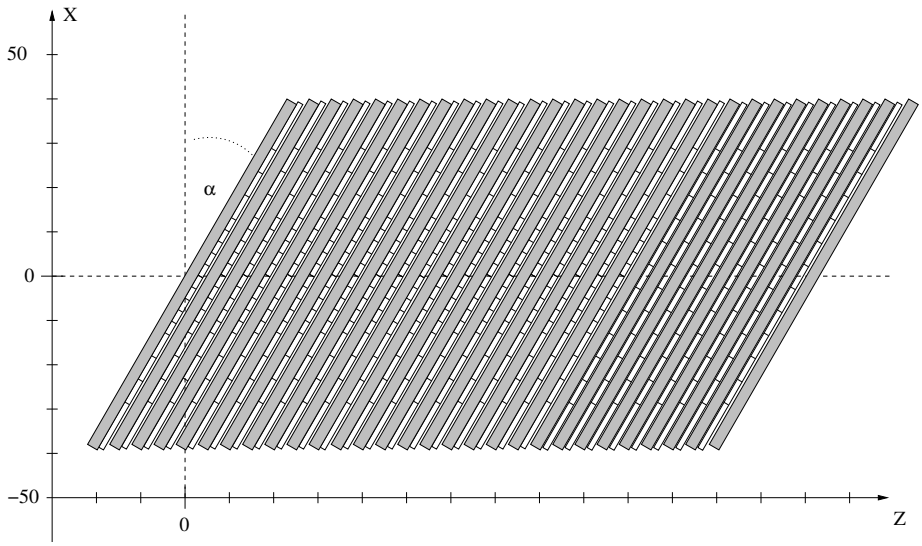

Figure 8.6: Schematic drawing of the rotated AHCAL.

8.2 Profiles in the AHCAL

The AHCAL is built from cells of three different sizes and uses a layout with reduced granularity for the last eight layers. This leads to a complex distribution of the positions and covered range of the cells, especially when the layers are rotated with respect to the beam axis. To avoid artifacts of the detector geometry in the measurement of shower profiles some way of homogenising has to be used. This section describes an approach to distribute the cell energy over the cell size.

8.2.1 General Considerations

The AHCAL test-beam prototype allows the orientation of the layers with respect to the beam to be changed. Figure 8.6 sketches the AHCAL in such a configuration. The beam enters the detector parallel to the z-axis. For better visibility, only 20 out of the 30 layers with the finer core are drawn. This configuration is often referred to as "rotated AHCAL", even though the main calorimeter axis is still parallel to the beam direction.

When measuring shower profiles, the detector layout and configuration has to be taken into account. One important aspect is that the detector is built from square cells while the shower development is best described in a cylindrical coordinate system. Whenever a reasonable binning is chosen, some cells will intersect more than one radial bin.

In the case of a rotated detector, the cells will cover a significant range in longitudinal direction. This not only implies that the cell might extend over more than one longitudinal bin, but also introduces some correlation between the radial and the longitudinal measurement. Finally, the rotated configuration introduces border regions where the detector is not sensitive in all positions.

Figure 8.7 shows the position of the detector cells with respect to the binning used for the measurement of the profiles. The radial binning is set to 3 cm which corresponds to the smallest cell size. This has the advantage that the width of the bin corresponds

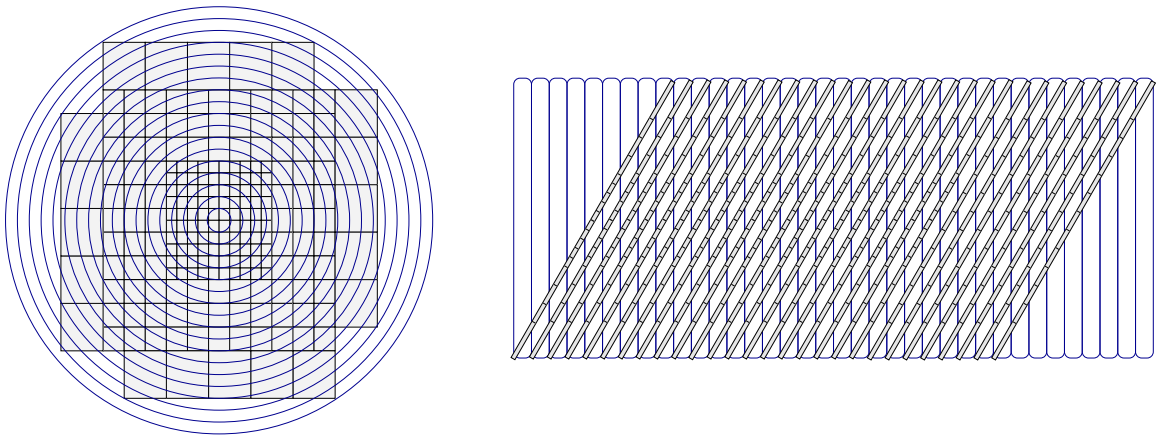

(a) (b)

Figure 8.7: Position of the rotated detector with respect to the radial (a) and longitudinal (b) binning.

approximately to the accuracy of the single cell position information. The longitudinal bin width is set to the distance between two layer centres. This ensures that the number of cells contributing to the different bins stays constant over the whole detector except for the border regions.

8.2.2 Ansatz: Virtualisation

As described before, cells will cover more than one bin. Therefore, some strategy is necessary to distribute the cell energy over the different bins. A procedure, called virtualisation, is used to achieve this. The main idea is to homogenise the detector geometry by subdividing the cells into virtual cells of $1\,\mathrm{cm}^2$ size.

Estimation of the Number of Particles in a Cell

The distribution of the visible energy left by single minimal ionising particles is recorded during the detector calibration for each cell. Knowing this distribution allows the thresholds for multiple MIPs to be distinguished. Figure 8.8(a) shows the simulated distributions for one to six MIPs. The crossing points where the $N+1$-MIP histogram becomes larger than the N-MIP histogram corresponds to an energy above which the signal is more likely to have been generated by $N+1$ MIPs than by N MIPs. While the absolute scale varies significantly, the shapes of these distributions change only moderately from cell to cell.

The threshold positions were calculated for 500 channels. The resulting thresholds, expressed in units of MIP, are shown in figure 8.8(b). The threshold is a linear function of the order. The inverse is used to estimate the probable number of particles in a cell. This overestimates the number of particles to some degree, as not all particles are minimum ionising. But it is more realistic than assuming that the signal comes from one particle or is homogeneously distributed over the cell.

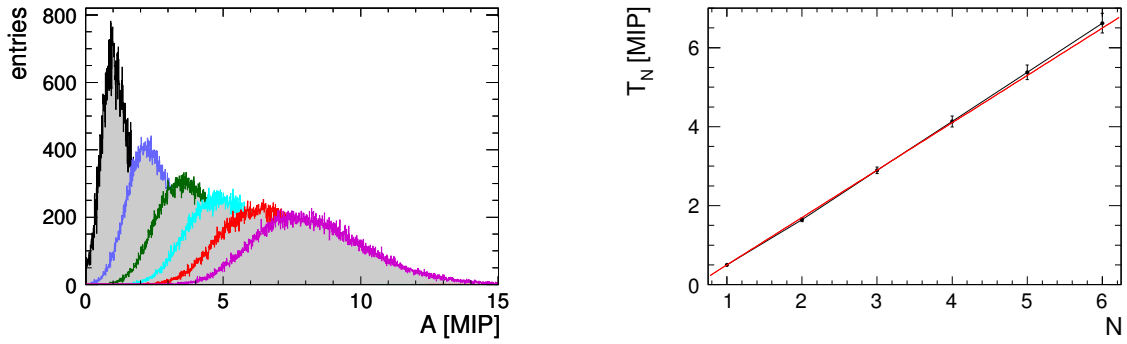

(a) (b)

Figure 8.8: Estimation of the number of particles in a cell from the recorded energy. (a) Distributions of N-MIP. (b) Threshold versus number of MIP N.

Distribution of Energy

It is assumed that the cell was hit by as many particles as estimated before. The total energy is equally distributed over these virtual particles. Each virtual particle is randomly assigned to one of the $1\,\mathrm{cm}^2$ virtual cells within the cell area.

This method ensures that the energy of the cell is on average distributed over the full space. In contrast to other methods, it ensures that neither the full energy of a highly active cell is assigned to a single space point nor the energy of a single minimal ionising particle is distributed to many space points. In the limit of many events, the mean energy in the virtual cell is the same for the different methods. But, the described method converges faster and delivers a more realistic energy distribution in the virtual cells. This helps to avoid threshold effects in a further analysis.

Border Regions and Normalisation

When the detector is in a rotated configuration, regions exist that have no full coverage along the longitudinal or radial bins. Figure 8.9 shows the front part of the detector with two regions marked. In the orange region the detector response is reduced, as some part of the space is not instrumented. In the red region the detector does not cover all radial positions anymore.

It is assumed that in average the showers develop symmetrically along the direction of the incoming particle. Under this assumption, one can consider some re-weighting to recover the response. But, it should be taken into account that the insensitive part is not equally spread over all radial positions. For the orange region, where all radial positions are still covered, a simple re-weighting using the fraction of the sensitive detector in each bin of z and r is applied. For the red region, where the response would have to be extrapolated to the uncovered radial positions, a more sophisticated method would be necessary. Currently, only showers that start after the red region are considered and the data from the cells in the red region are neglected.

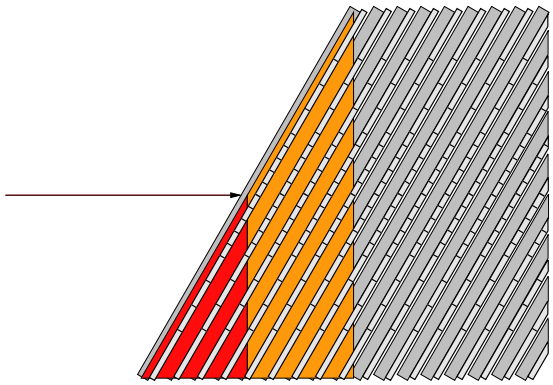

Figure 8.9: Front region of the rotated AHCAL.

Crosscheck

The method to measure profiles for an arbitrary angle was crosschecked with data measured in the zero degree configuration. The longitudinal profile obtained with this method was compared to a simple layer-wise energy sum profile. The results were consistent with being identical.

8.2.3 Profiles from Shower Start

Knowing the shower start point allows the shape of the hadron shower development to be measured independently of the fluctuations in the first nuclear interaction.

Shifting Cell Positions

To first approximation, the found shower start point $\vec{r}_{\text{start}}$ has to be subtracted from the cell positions $\vec{r}_{\text{cell}}$:

$$\vec{r}'_{\text{cell}} = \vec{r}_{\text{cell}} - \vec{r}_{\text{start}}. \tag{8.1}$$

This neglects the systematic difference between real and measured shower start point. More accurately, this offset $\vec{r}_{\text{offset}}$ should be taken into account:

$$\vec{r}'_{\text{cell}} = \vec{r}_{\text{cell}} - (\vec{r}_{\text{start}} - \vec{r}_{\text{offset}})\,. \tag{8.2}$$

Figure 8.10 displays the offsets predicted by different simulation models. $\vec{r}_{\text{offset}}$ depends significantly on the energy and the physics model chosen in the simulation. It is assumed that the offset present in data lies in the range of the simulation predictions. The middle of the range is subtracted as reference value from data at each energy point. The high and low limits of the range are used to calculate the systematic uncertainty on this assumption.

Normalising for Detector Acceptance

When overlaying shower start point-corrected events, it is important to consider that the detector acceptance relative to the start point changes with the position of the shower start.

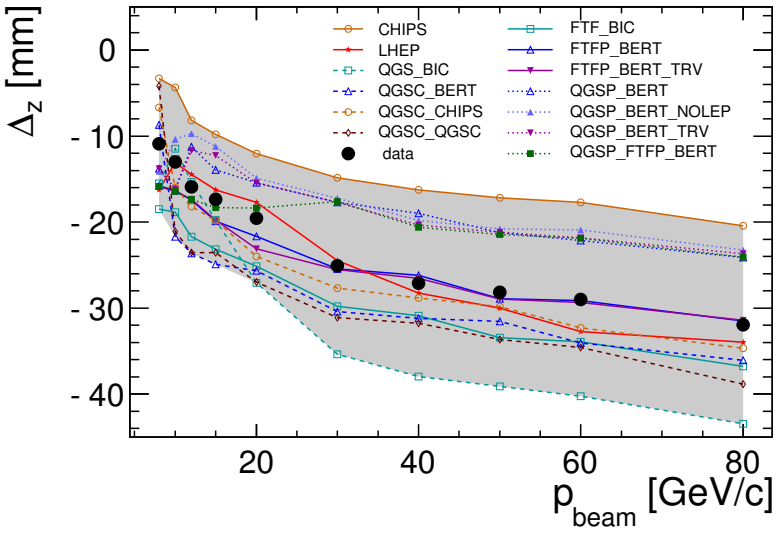

Figure 8.10: Predictions for the systematic shift from different simulation models and assumption for data.

Figure 8.11 shows an illustration of two showers with same longitudinal development but different shower start points. While the full response is recorded for the blue shower, the red shower is only partly recorded as the detector ends.

The virtualisation ansatz gives an elegant way of keeping track of the different measurement ranges in the events. The three dimensional positions of all virtual $1\,\mathrm{cm}^2$ cells representing the active detector are known.

A normalisation histogram with identical binning to the measurement histogram is filled with the positions calculated with equation 8.1 for all unmasked (see section 8.2.2) virtual cells independent of the occupation state of the cells. The resulting histogram represents the sum of the active detector area for each bin. This allows the measurement to be normalised bin by bin to the energy density per event.

8.2.4 Two Dimensional Profiles

The described methods are used to measure the two dimensional profile of hadron showers. Both, the classical profile where the shower profile in the detector is measured, as well as the shower development with respect to the first hard interaction are studied. Figure 8.12 shows shower profiles of 10 GeV negatively charged pions and 80 GeV positively charged pions. The energy density per event is plotted versus the radius r of the radial ring and its longitudinal position z. While figures 8.12(a) and 8.12(b) show the profile as it is recorded within the detector, figures 8.12(c) and 8.12(d) show the measurement from the shower starting point normalised to the effective detector response.

The shapes of the showers are important for the particle flow approach, as it is necessary to distinguish between nearby showers. Especially, it is important to have reliable predictions of the shower shape in the simulations used for the design of the detector.

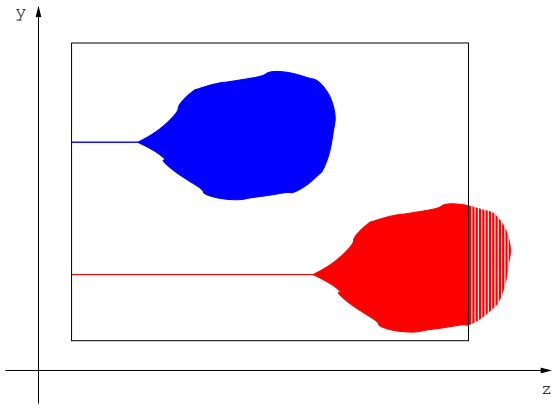

Figure 8.11: Side view of AHCAL (no rotation). Two showers of the same size but with different point of shower start are sketched.

Therefore, the results of this measurement are compared to different simulation models. The results of the studies are discussed in chapter 9.

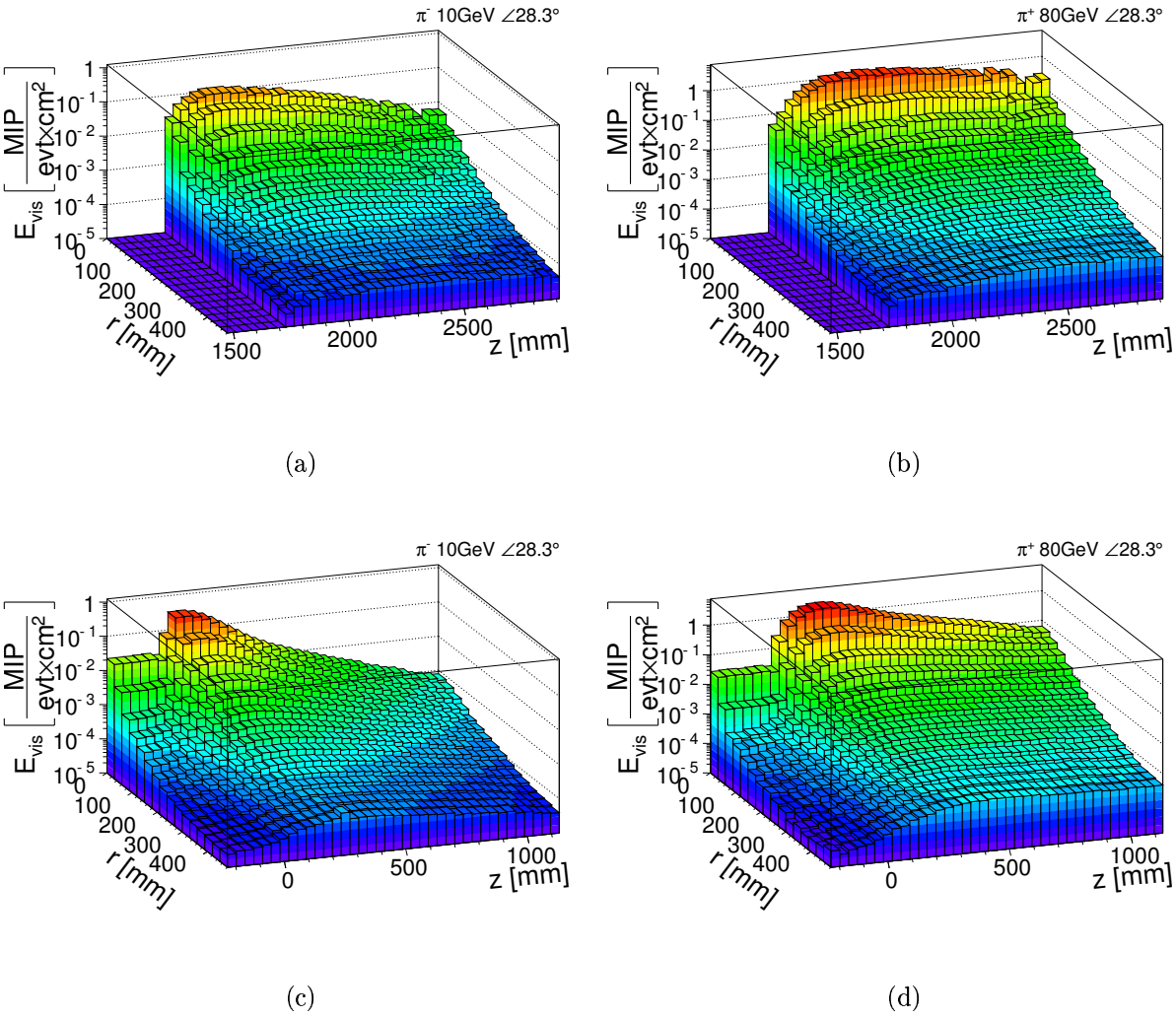

Figure 8.12: Two dimensional profiles of pion showers inside the AHCAL. The energy density is drawn versus the longitudinal position z and the radial distance to the calorimeter centre r. (a) and (b) show the profiles measured in reference to the calorimeter. (c) and (d) show the profiles measured in reference to the shower start. (a) and (c) are the profiles of 10 GeV π^-, and (b) and (d) are the profiles of 80 GeV π^+.

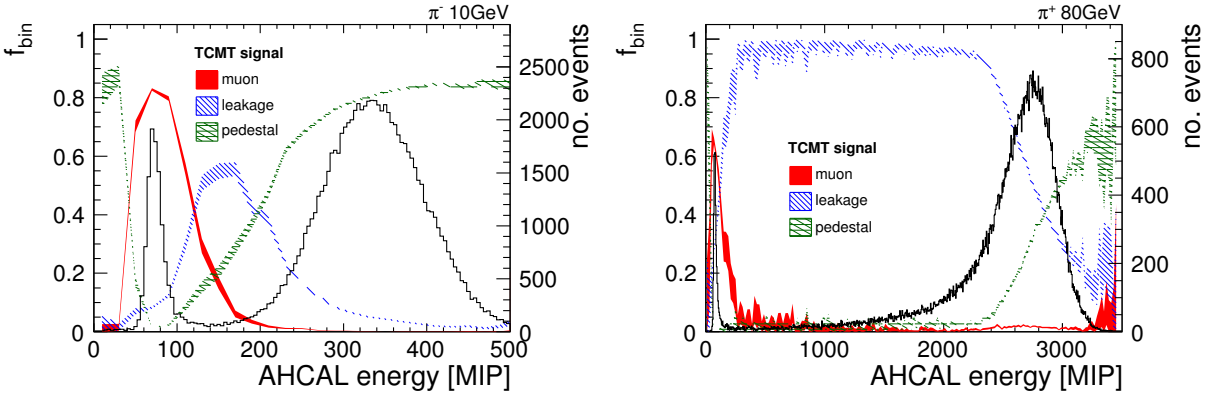

(a) (b)

Figure 8.13: The raw energy distribution in the AHCAL for two different pion energies: (a) 10 GeV and (b) 80 GeV. The fraction of the events that have a pedestal, muon, or leakage like signal in the TCMT is plotted for each bin.

8.3 Leakage

The fraction of the absorbed energy in a hadronic calorimeter depends on the depth of the calorimeter. The energy of the particles that are leaving the detector volume is called leakage. As the shower size varies with energy, this can introduce a non-linearity to the response of a hadronic calorimeter. Also, the energy resolution of a calorimeter will worsen as the amount of leakage will fluctuate event by event. The size of the calorimeter inside a high energy physics detector has to be chosen sufficiently large to achieve reasonable results for linearity and resolution.

One fluctuation in hadron shower developments is the position of the first interaction. Figure 8.11 sketches the case of two showers of the same energy but with different shower starting point. It is obvious that in the case of a late shower start the probability for leakage is larger than in the case of an early shower start. If the relation between shower starting point and leakage is known, the calorimeter signal can be corrected for this effect. This section discusses the applicability of a shower start based leakage correction.

8.3.1 Signal Definition

The reconstructed energy E_{AHCAL} and the resolution σ_{AHCAL} have to be measured in a robust way for the leakage analysis. Figure 8.13 shows the raw signal distribution in the AHCAL for pion beams with two different energies. The TCMT is used to identify the type of the events at different positions in the spectrum. The fraction of muon events, fully contained events, and leakage events is superimposed on the spectrum. Muons are identified using the method described in section 7.1.2. Fully contained events are defined as events with a TCMT signal in agreement with a pedestal signal. Leakage events are defined as events that have neither a muon nor pedestal signal in the TCMT.

One problem is the contamination of the signal with muons and the fact that the fraction of muons changes significantly with the beam energy. The TCMT is used to identify these muons, but the detection efficiency is not 100 % and some muons will be left in the sample. In the case of 30 GeV pions the muon content is highest. The contamination of the sample will be approximately 6 % at this energy. At all other energies the remaining contamination is 2 % or smaller.

A second issue is the shape of the distribution, especially the long tail to low values. The root mean square of the distribution will overestimate the width of the resolution. A fit of the main peak with a Gaussian distribution will underestimate the width. Therefore, the following method has been chosen to measure σ_{AHCAL}: The position of the central range with $\frac{2}{3}$ of the statistics is determined. For this, the position $q(\chi)$ is calculated for $\frac{1}{6}$ and $\frac{5}{6}$, where $q(\chi)$ is defined by the following relation:

$$\chi = \frac{\int_{-\infty}^{q(\chi)} f(x)\mathrm{d}x}{\int_{-\infty}^{\infty} f(x)\mathrm{d}x}. \tag{8.3}$$

The resolution is then half the distance between the two measured positions:

$$\sigma_{\mathrm{AHCAL}} = \frac{q\left(\frac{5}{6}\right) - q\left(\frac{1}{6}\right)}{2}. \tag{8.4}$$

8.3.2 Energy Calibration

The desired result of a calorimeter measurement is the energy E of the impact particle rather than the visible energy E_{vis}. The calorimeter response can be calibrated with the help of test-beam data. It is assumed that the total energy is related to the visible energy by

$$E = \frac{1}{\alpha} \cdot (E_{\mathrm{vis}} - \nu)\,, \tag{8.5}$$

where α is the calibration factor and ν the noise.

The visible energy is measured for different beam momenta p_{beam}. To avoid leakage, showers that start in layers two to four are used. The calibration factors α and ν are determined with a linear fit. The following values have been obtained: α=(33.41±0.02) MIP/GeV and ν=(9.4±0.5) MIP. Figure 8.14(a) shows the measured values, the fit, and the residual to the fit. The maximum deviations from linearity are approximately 1 %. The two largest deviations are observed for 15 GeV and 30 GeV beams. The dip at 30 GeV is explained by the described remaining contamination of muon events in the sample.

8.3.3 Leakage Correction

The response of the AHCAL is measured for different shower start points. Figure 8.14(a) displays the measured curves. The later the shower starts the lower the reconstructed signal becomes. The shape of the hadron showers reflects in this curves. The long tail seen in longitudinal profiles of hadron showers leads to a moderate reduction of the reconstructed energy up to the point where the core of the shower starts to move out of the calorimeter. Afterwards, the reconstructed energy drops down fast.

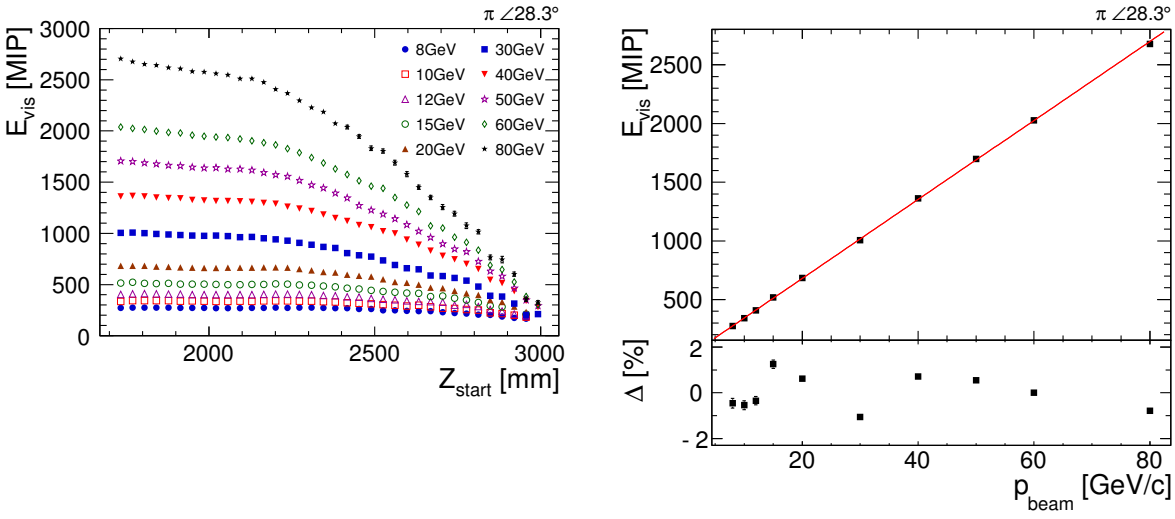

(a) (b)

Figure 8.14: (a) The response of the AHCAL to pions. The mean visible energy E_{vis} is plotted against the shower start position z_{start} for different beam momenta. (b) Calibration of the detector response. The mean visible energy E_{vis} is plotted against the beam momentum p_{beam} for showers that start in the first 10 cm of the AHCAL. The red line shows the calibration fit. The lower plot shows the residual Δ for the different measurements. Only statistical errors are displayed.

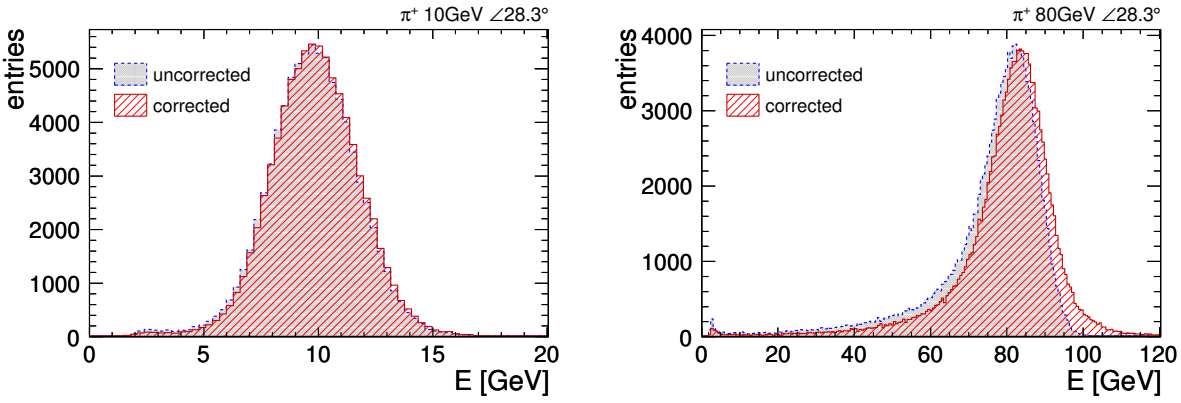

(a) (b)

Figure 8.15: Leakage correction: The distributions of the reconstructed energy E in the AHCAL are shown for (a) 10 GeV negative pions and (b) 80 GeV positive pions. The uncorrected distributions are plotted with blue line and grey filling. The corrected distributions are drawn in red colour.

The correction function is the inverse of the response curve normalised to the average of the first two points. In this study the corresponding function is selected by the beam energy setting. Therefore, the results presented are idealistic. In a collision experiment, the particle energy is not known a priori. It would be necessary to have already some first approximation of the particle energy to select the right correction function. Studies with a generalised parametrisation of the response are in progress [60].

The energy distributions of pions are shown in figure 8.15 for corrected and uncorrected data. At 10 GeV/c beam momentum, longitudinal leakage is rare and only small changes are visible. In the case of 80 GeV pions, the correction shifts the distribution to higher values; and the result is more symmetric than in the uncorrected case. But, it is also visible, that not all events with leakage are corrected properly. The tail to lower values is still significant.

The mean reconstructed energy E_{AHCAL} and the resolution σ_{AHCAL} are measured for beam momenta between 8 GeV and 80 GeV to quantify the effect of the leakage correction. Figure 8.16 depicts the results. The residuals Δ_E of the mean energy to the beam energy are comparable to the residuals of the calibration after correction. Without the correction, residuals up to 5 % at 80 GeV are observed. At the same time, the energy resolution is improved by more than 10 % at 80 GeV.

8.3.4 Conclusions

The knowledge of the first hard interaction gives some limited handle on correcting longitudinal leakage. It allows the linearity and resolution of the reconstructed energy to be improved. The correction becomes more relevant for higher energies as the showers grow in size. The non-linearity can be corrected from 5 % to approximately 1 %. The im-

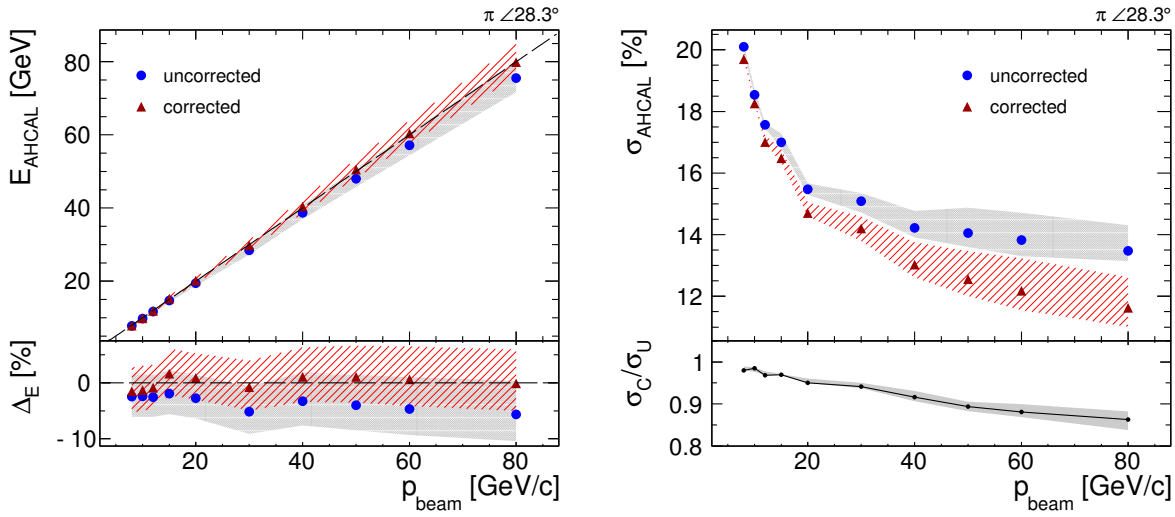

(a) (b)

Figure 8.16: (a) The response of the AHCAL to pions with different energy. The reconstructed energy E_{AHCAL} is plotted against the pion momentum p_{beam}. The red triangles show the result after the leakage correction was applied. The blue squares show the response measured without correction. The dashed black line indicates the one to one relation. The lower plot shows the residual to the one to one correspondence. The bands show the cell calibration uncertainty.
(b) The energy resolution of the AHCAL at different pion energies. The resolution σ_{AHCAL} is plotted versus the beam momentum p_{beam}. The red triangles show the resolution measured with correction; the blue squares the measurement without correction. The lower plot shows the ratio of the corrected resolution σ_{c} over the uncorrected resolution σ_{U}. The bands show the cell calibration uncertainty.

provement on the resolution increases with energy and reaches more than 10 % at 80 GeV. Nevertheless, the energy distribution still shows a significant tail to lower values.

In the studied case, the idealistic assumption is made that the selection of the detector response function can be done perfectly. A practical method might give less good results due to uncertainties in this selection.

Studies are ongoing exploiting additional observables like the energy fraction in the back of the calorimeter. First results suggest that this can further improve the detector resolution. But, all calorimeter based methods will be inherently limited at some level, as the recorded information is reduced due to leakage. The persistent tail in the energy distribution is a sign of this. At some point, further improvement will be only possible by extending the calorimeter. This is also visible in figure 8.13 which shows that the TCMT records leakage for practically all events in the tail of the 80 GeV distribution.

Chapter 9

Comparison of Measurement and Simulation

The methods described in chapter 8 are applied to measurements taken at the CERN test-beam and compared to the predictions of simulation. Several different simulation models are confronted with the measurement to judge the quality of the competing approaches and identify the best model for hadron simulation. The comparison comprises thirteen different Geant4 physics lists. A detailed description of the physics lists can be found in section 6.1.1. The physics lists are arranged into four groups according to their high energy model.

9.1 Shower Start Distribution

The shower start points follow an exponentially falling distribution. In principle, this distribution can be used to measure the nuclear interaction length inside the detector. But two effects have to be considered when interpreting the result. First, the resolution and offset of the shower start finder lead to a pileup in the first layers. And the predictions for the resolution vary significantly between simulation models. Second, calibration errors can lead to a different noise prediction in measurement and simulation. This can lead to regions with differing detection efficiencies. Both effects lead to a significant dependence of the fit result on the exact fit range. Except LHEP, all models showed a description of the data within the accuracy of the method. The fitted values lie within 5 % of the expected value of 28.1 cm for both data and simulation, although no realistic description of the shower start resolution is used. LHEP predicts a 10 % stronger attenuation of the pion beams. Figure 9.1 shows the measured and simulated results for 10 GeV and 50 GeV pions.

9.2 Response and Resolution with Leakage Correction

The response of the AHCAL after leakage correction is compared to the simulation predictions. Figure 9.2 displays the results. All physics lists except CHIPS show a stronger non-linearity than data. The FTF physics lists stay within the error of the data. The

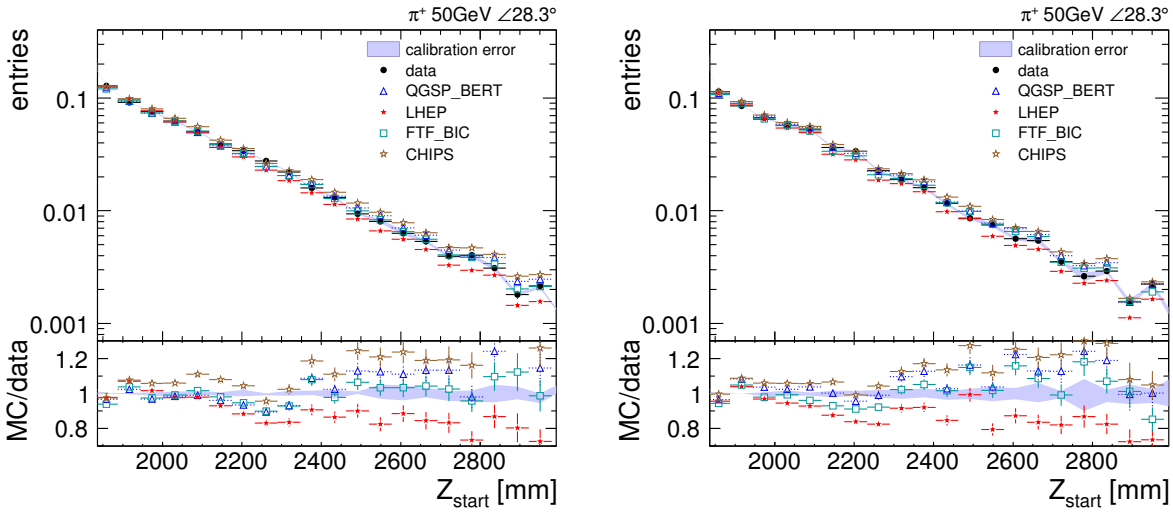

(a) (b)

Figure 9.1: Distribution of reconstructed shower start points measured with pion beams. Test-beam data and simulation predictions are shown for 10 GeV negative pions (a) and 50 GeV positive pions (b). The physics lists are selected such that all studied models are represented.

QGSP lists give energies approximately 2 % above the data range for beam momenta larger than 20 GeV. QGSC_CHIPS shows the same kind of overestimation but with deviations up to 4 % at 80 GeV. QGS_BIC, QGSC_BERT, and QGSC_QGSC predict energies in agreement with the errors for beam momenta higher than 20 GeV, but show up to 5 % less energy than measured for beam momenta smaller 20 GeV. LHEP predicts even less signal in the low energy range, such that the residual is 7 % smaller than the lower bound of the measurement.

The CHIPS physics list shows a completely different response from the other lists. The shape corresponds to the measured one, but the predicted visible energy is approximately 10 % higher than the mean response, leaving a discrepancy of at least 5 % when the errors are considered.

The resolution of the AHCAL after leakage correction is plotted in figure 9.3. The two jumps in the resolution at 15 GeV and 30 GeV are attributed to a beam contamination: e.g. the beam contains residual muons at 30 GeV that lower the response and thus increase the relative resolution. Neglecting these two jumps, the FTF physics lists can predict the resolution within the measurement uncertainty. Also the QGS_BIC model performs reasonably. The QGSP physics lists show a slightly better resolution than observed. The QGSC_CHIPS physics lists has the same level of agreement. The other QGSC physics lists predict a significant worse resolution. The same is true for the LHEP physics list. CHIPS is the only physics list that predicts a significantly better resolution than observed.

A second observable is the predicted resolution improvement due to leakage correction. Figure 9.3 contains the ratio of the resolutions of corrected and uncorrected measurements. The FTF, QGSP, QGS_BIC, and QGSC_CHIPS physics lists predict the improvement

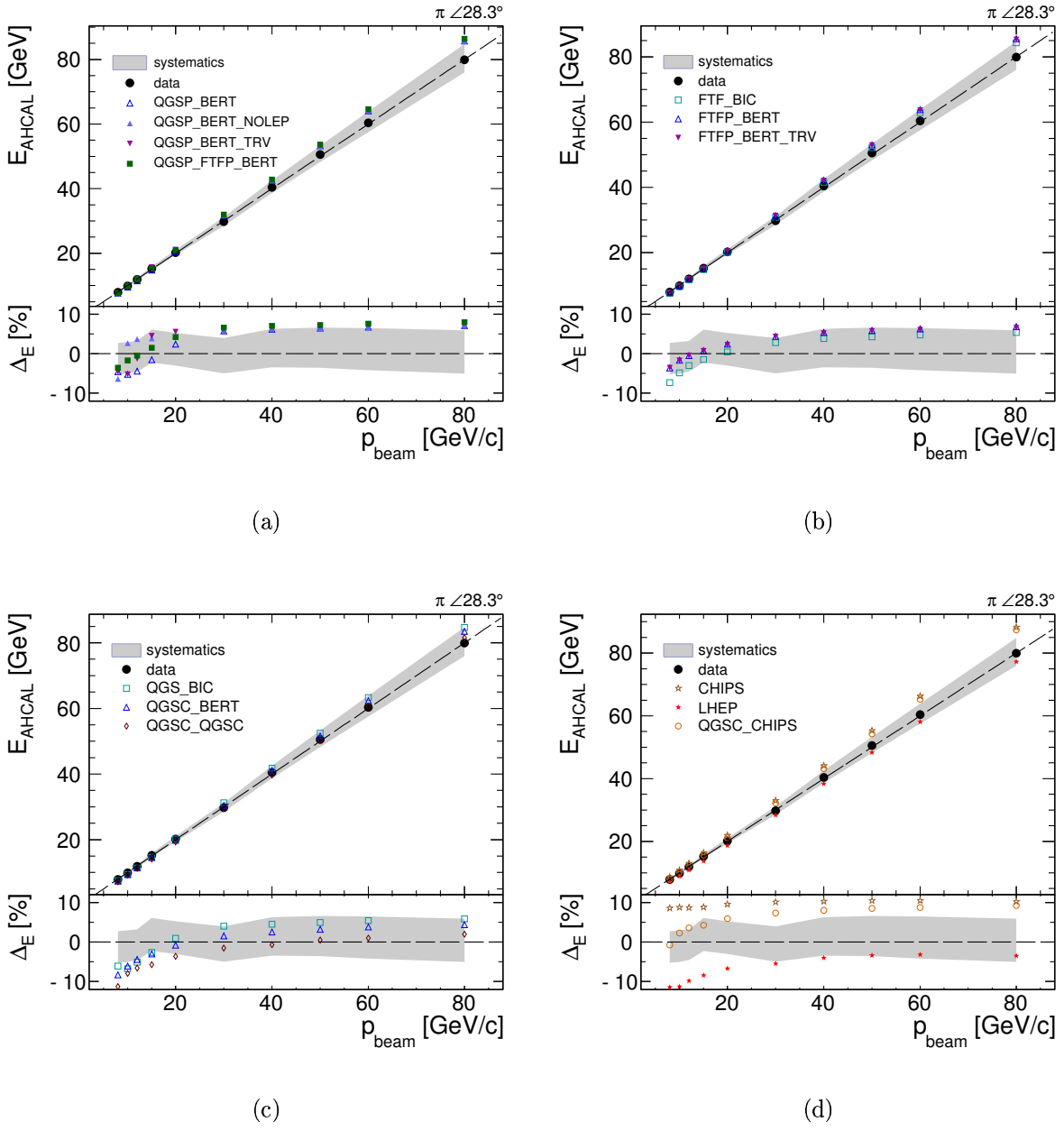

Figure 9.2: Leakage corrected response of the AHCAL. Simulations with different physics lists are compared to the CERN test-beam measurements. The reconstructed energy E_{AHCAL} is plotted against the pion momentum p_{beam}. The dashed black line indicates the one to one relation. The lower plot shows the residual to the one to one correspondence. The grey bands indicate the cell calibration uncertainty.
(a) Simulations with the QGSP model.
(b) Simulations with the FTF model.
(c) Simulations with the QGS and QGSC models.
(d) Simulation with the CHIPS model and the LHEP model.

correctly. The QGSC_BERT and QGSC_QGSC physics list predict less improvement for energies larger than 30 GeV. The LHEP physics list always predicts a too small improvement and the CHIPS physics list predicts almost a factor two better enhancement.

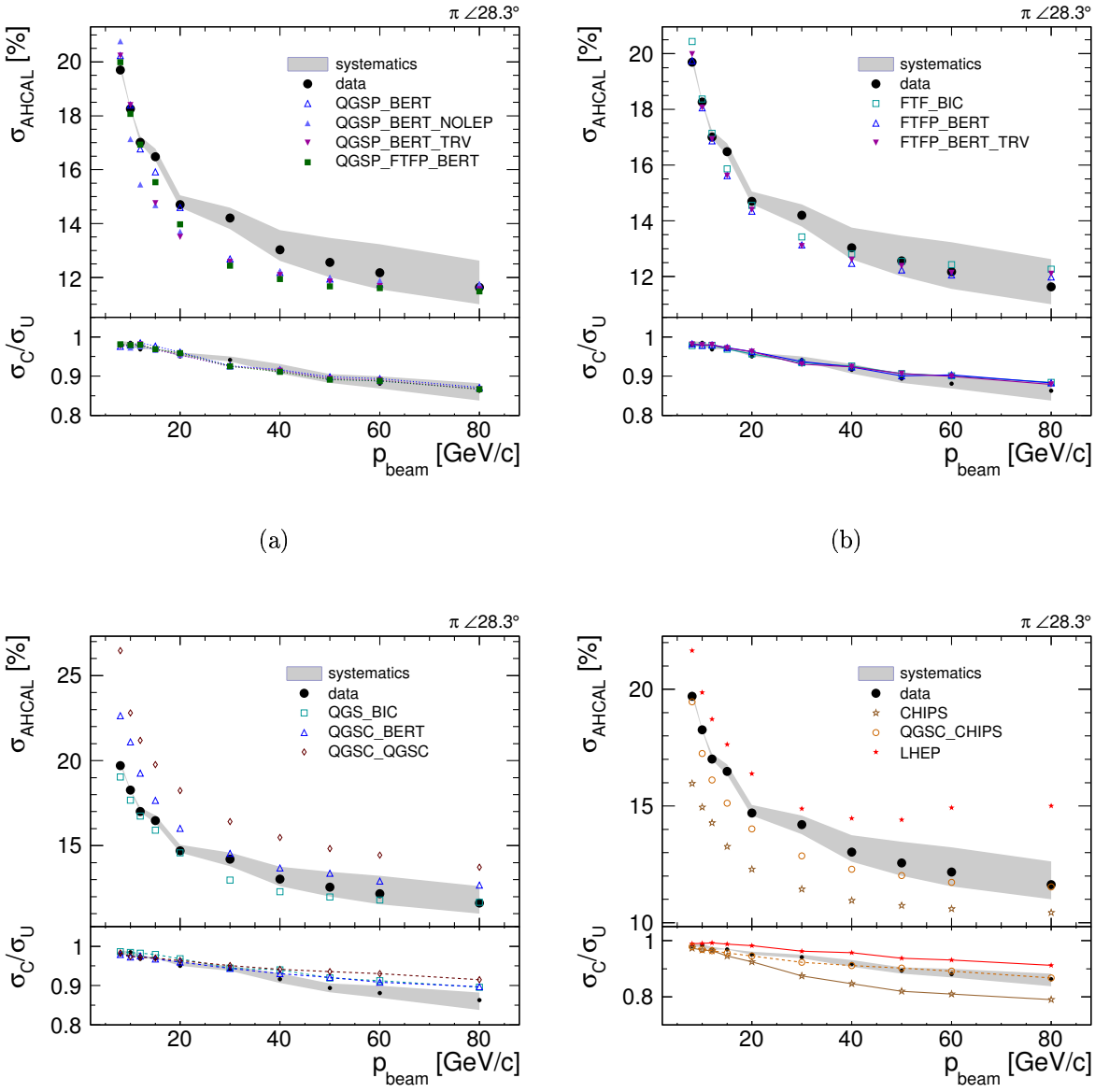

Figure 9.3: Resolution σ_{AHCAL} after application of the leakage correction. Simulations with different physics lists are compared to the CERN test-beam measurements. The resolution as defined by equation 8.4 is plotted versus the beam momentum p_{beam}. The lower plot shows the ratio of the corrected resolution over the uncorrected resolution. The grey bands indicate the cell calibration uncertainty.
(a) Simulations with the QGSP model.
(b) Simulations with the FTF model.
(c) Simulations with the QGS and QGSC models.
(d) Simulation with the CHIPS models and the LHEP model.

9.3 Spatial Development

In the particle-flow approach, the jet resolution depends on the capability to separate nearby showers. Therefore, it is especially important to have a realistic prediction of the shower shapes in simulation. The profiles recorded with the AHCAL are a good reference to judge the quality of the simulation in this aspect. The possibility to measure shower profiles from the start point of the shower increases the sensitivity of the comparison. Longitudinal and radial projections are chosen to enhance different aspects of the shower shape. The shapes are presented for all physics lists and two representative energies, as the physics lists typically show different behaviour below and above approximately 20 GeV.

9.3.1 Radial Profile

Figures 9.4 and 9.5 show the radial profiles of 10 GeV and 80 GeV pion showers. The energy density is plotted versus the radial distance to the centre of the calorimeter. For better visibility, the physics lists are grouped according to their high energy model. All models predict a higher density in the core of the shower than observed. Likewise, all models except CHIPS show a deficiency between 8 cm and 11 cm. This means that the shower core is wider in data than in simulation. Apart from this, most models predict the further development quite well. Especially the QGSP and FTF physics lists can describe the profile within the accuracy of the measurement. The QGSC_BERT and QGS_BIC physics lists show in general a lower energy density for radii larger than 6 cm. Exceptions are the two CHIPS predecessor models QGSC_QGSC and QGSC_CHIPS as well as the LHEP model. While the LHEP model predicts a significantly narrower profile, the two other models predict much stronger tails than observed.

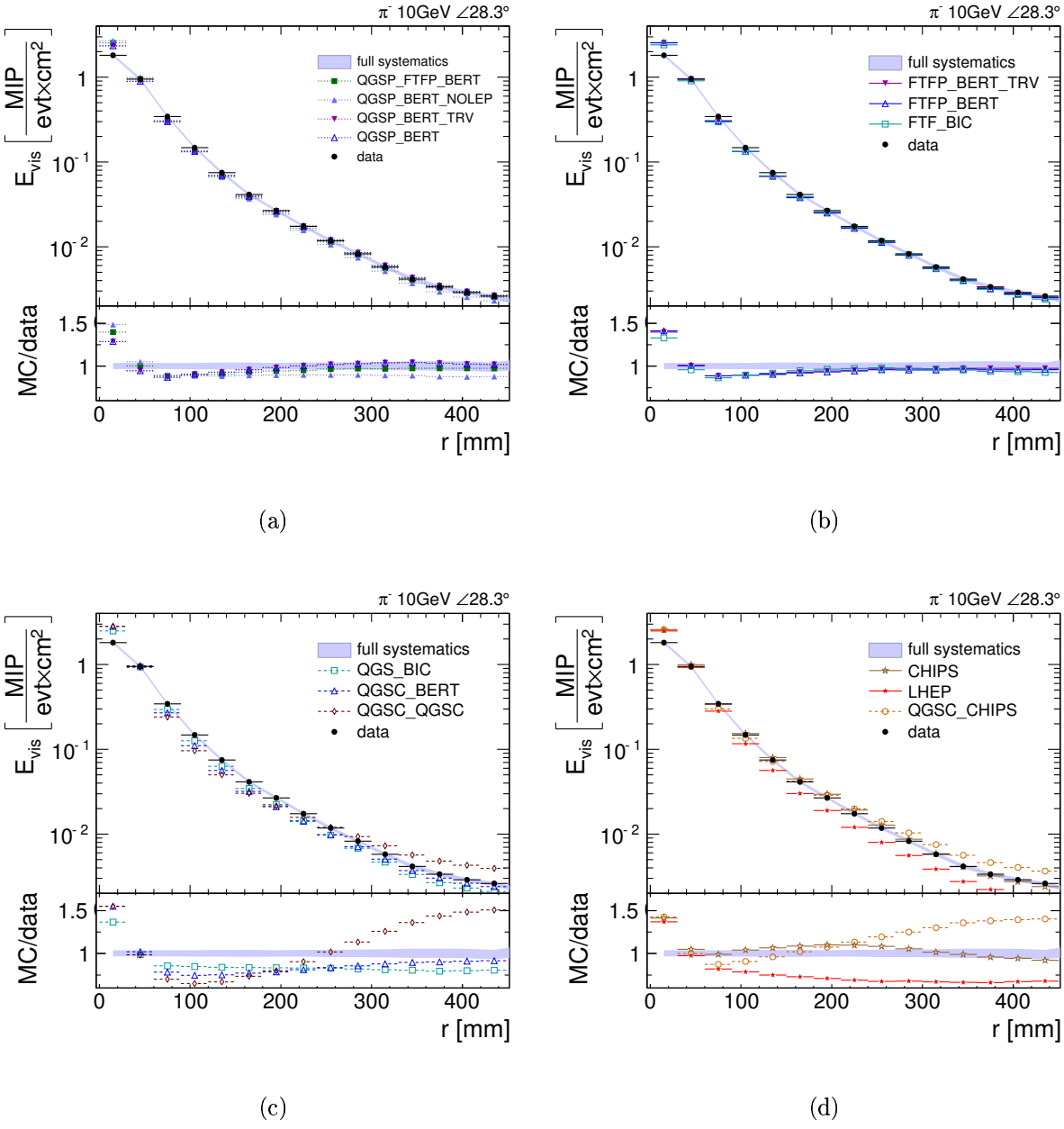

Figure 9.4: Comparison of simulation predictions to test-beam measurements. The radial profile of 10 GeV negative pion showers is compared to simulations using different Geant4 physics lists. The energy density is drawn versus the radial distance to the calorimeter center r. The lower plots show the ratio of simulation over data.
(a) Simulations with the QGSP models.
(b) Simulations with the FTF models.
(c) Simulations with the QGSC models.
(d) Simulation with the CHIPS models and the LHEP model.

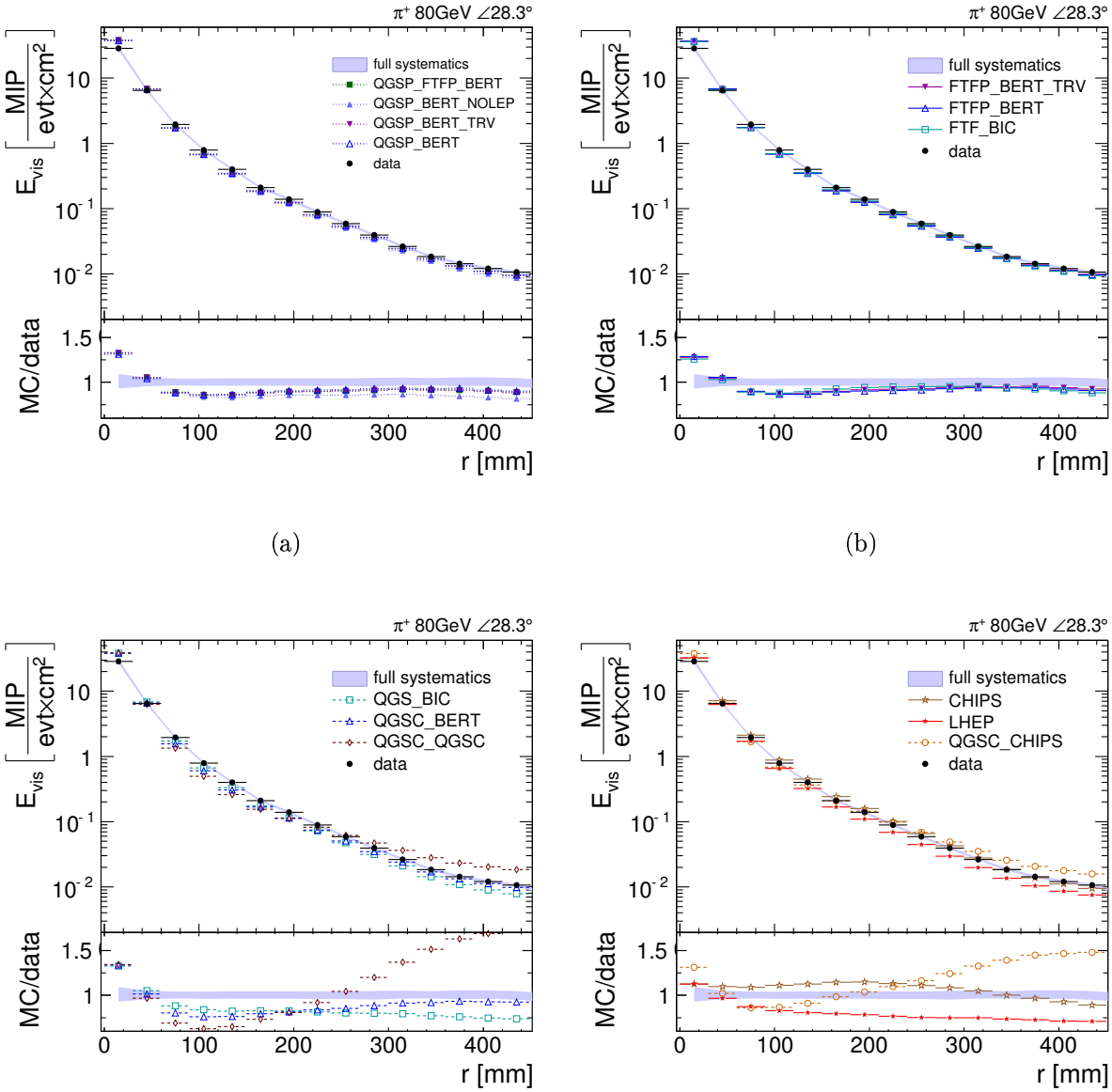

Figure 9.5: Comparison of simulation predictions to test-beam measurements. The radial profile of 80 GeV positive pion showers is compared to simulations using different Geant4 physics lists. The energy density is drawn versus the radial distance to the calorimeter center r. The lower plots show the ratio of simulation over data.
(a) Simulations with the QGSP models.
(b) Simulations with the FTF models.
(c) Simulations with the QGSC models.
(d) Simulation with the CHIPS models and the LHEP model.

9.3.2 Longitudinal Profile

Figures 9.6 and 9.7 show the longitudinal profiles of 10 GeV and 80 GeV pion showers. The energy density is plotted against the longitudinal position z inside the calorimeter. At low energies, the FTF_BIC, the QGSP_BERT, and the QGSP_BERT_TRV physics list describe the profile within the accuracy of the measurement. The other variants of FTF and QGSP_BERT perform only slightly worse. The QGS_BIC and LHEP physics lists shows a too short tail of the distribution. The QGSC physics lists show a tendency for a too large signal at the rise of the shower. The CHIPS physics list shows a shifted peak position.

At higher energies, an excess of the simulation over the measurement becomes visible in the region of the shower maximum for all physics lists except LHEP. In contrast to the low energy showers, the tail of the distribution is matched by all simulation models.

The data curves show a variation from layer to layer that is not present in the simulation. These variations come from the systematic calibration uncertainties. As it was discussed in section 4.4.5, these uncertainties are largest when only a few cells contribute to the signal. The strong increase of the layer to layer variations in the response indicate that for this energies the systematic uncertainty comes mainly from the saturation correction. This supports the assumption, that the main systematic error is the uncertainty in the saturation scaling factor.

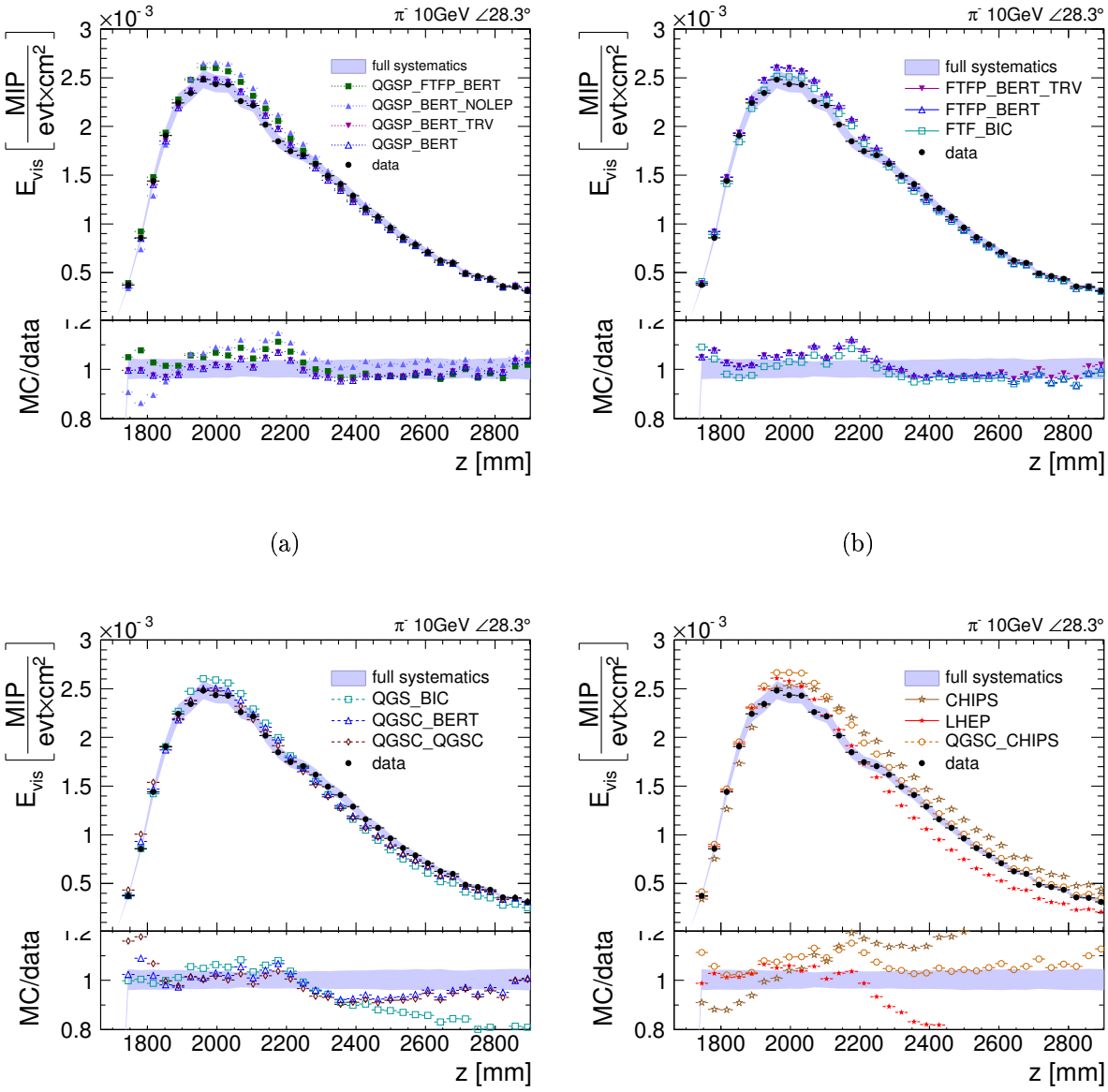

Figure 9.6: Comparison of simulation predictions to test-beam measurements. The longitudinal profile of 10 GeV negative pion showers is compared to simulations using different Geant4 physics lists. The energy density is drawn versus the longitudinal position z. The lower plots show the ratio of simulation over data.
(a) Simulations with the QGSP models.
(b) Simulations with the FTF models.
(c) Simulations with the QGSC models.
(d) Simulation with the CHIPS models and the LHEP model.

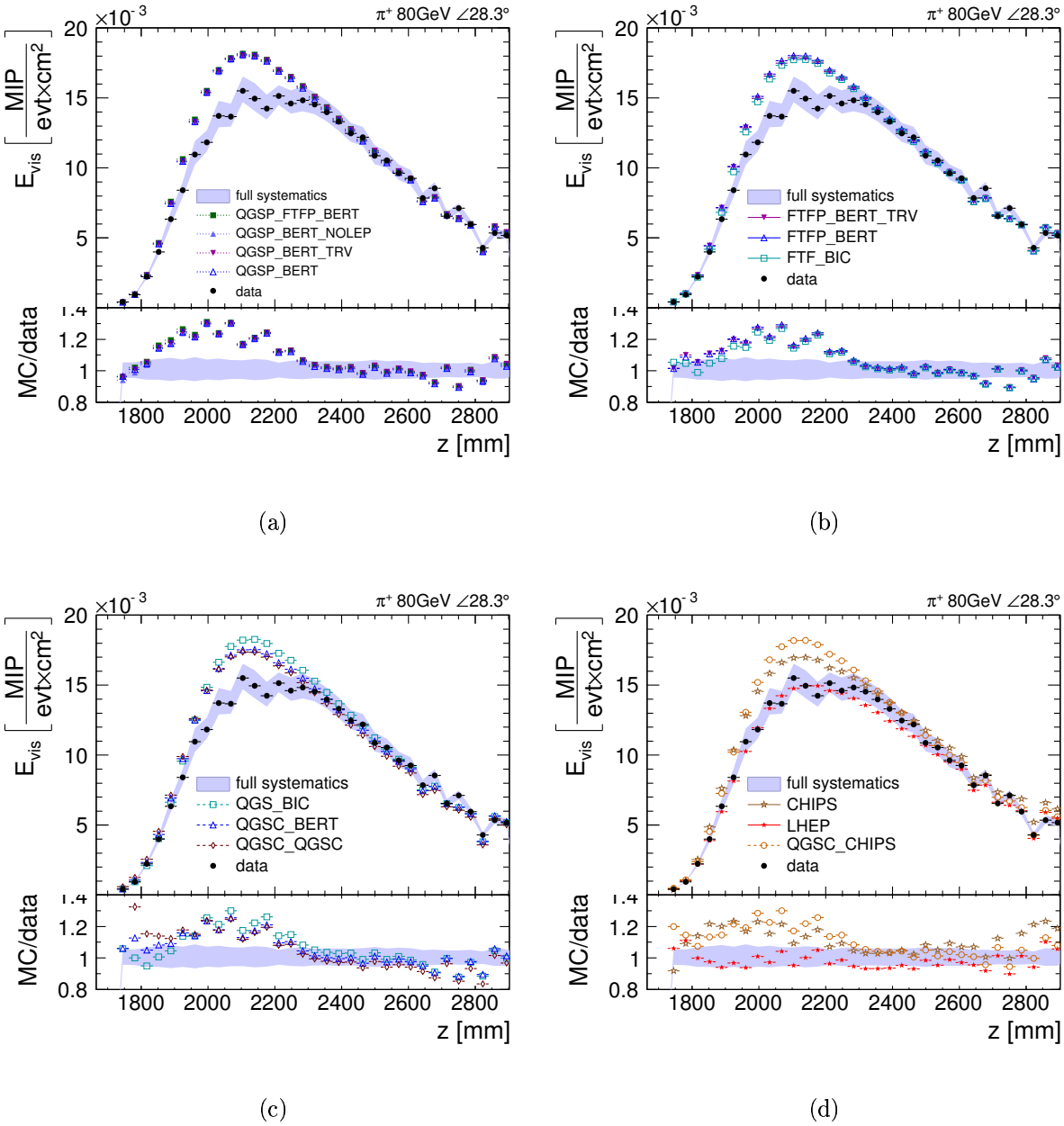

Figure 9.7: Comparison of simulation predictions to test-beam measurements. The longitudinal profile of 80 GeV positive pion showers is compared to simulations using different Geant4 physics lists. The energy density is drawn versus the longitudinal position z. The lower plots show the ratio of simulation over data.
(a) Simulations with the QGSP models.
(b) Simulations with the FTF models.
(c) Simulations with the QGSC models.
(d) Simulation with the CHIPS models and the LHEP model.

9.3.3 Longitudinal Profile from Shower Start

The position fluctuations of the first interaction are removed from the profile when it is recorded from shower start. This gives a better measure of the longitudinal shape of the shower core. Additionally, the profile is measured at different positions in the detector, which cancels some of the calibration errors that were visible as jumps in the standard longitudinal profile. Figures 9.8 and 9.9 show the longitudinal profiles measured from shower start. The full error band combines the shower start uncertainty in data (see section 8.2.3) and the calibration uncertainty (see section 4.4.5). To give an impression of the size of the shower start uncertainty, it is shown additionally.

The FTF and QGSP physics lists can describe the low energy profiles well within the measurement errors, except a small excess in the QGSP_BERT_NOLEP physics list at the position of the shower maximum. The QGSC physics list also give a reasonable description, only slightly worse than the previous mentioned physics list. Neither the QGS_BIC nor the LHEP physics list can describe the tail of the distribution. Both suggest shorter showers than measured. The peak position simulated by the CHIPS physics list is matched better when measured from shower start, but the showers are significantly longer than measured.

At high energies all physics lists except LHEP predict more visible energy in the shower maximum than observed in the test-beam data. LHEP, CHIPS, and QGSC_CHIPS are the only physics lists that can predict the tail of the shower correctly. All other models simulate too short showers. Also, the position of the peak is not described well by most of the lists. Only the FTFP physics lists and the QGSC_CHIPS physics list match the position. The QGSP lists and the CHIPS list peak too early. The QGSC_QGSC list and the lists which include BIC peak too late.

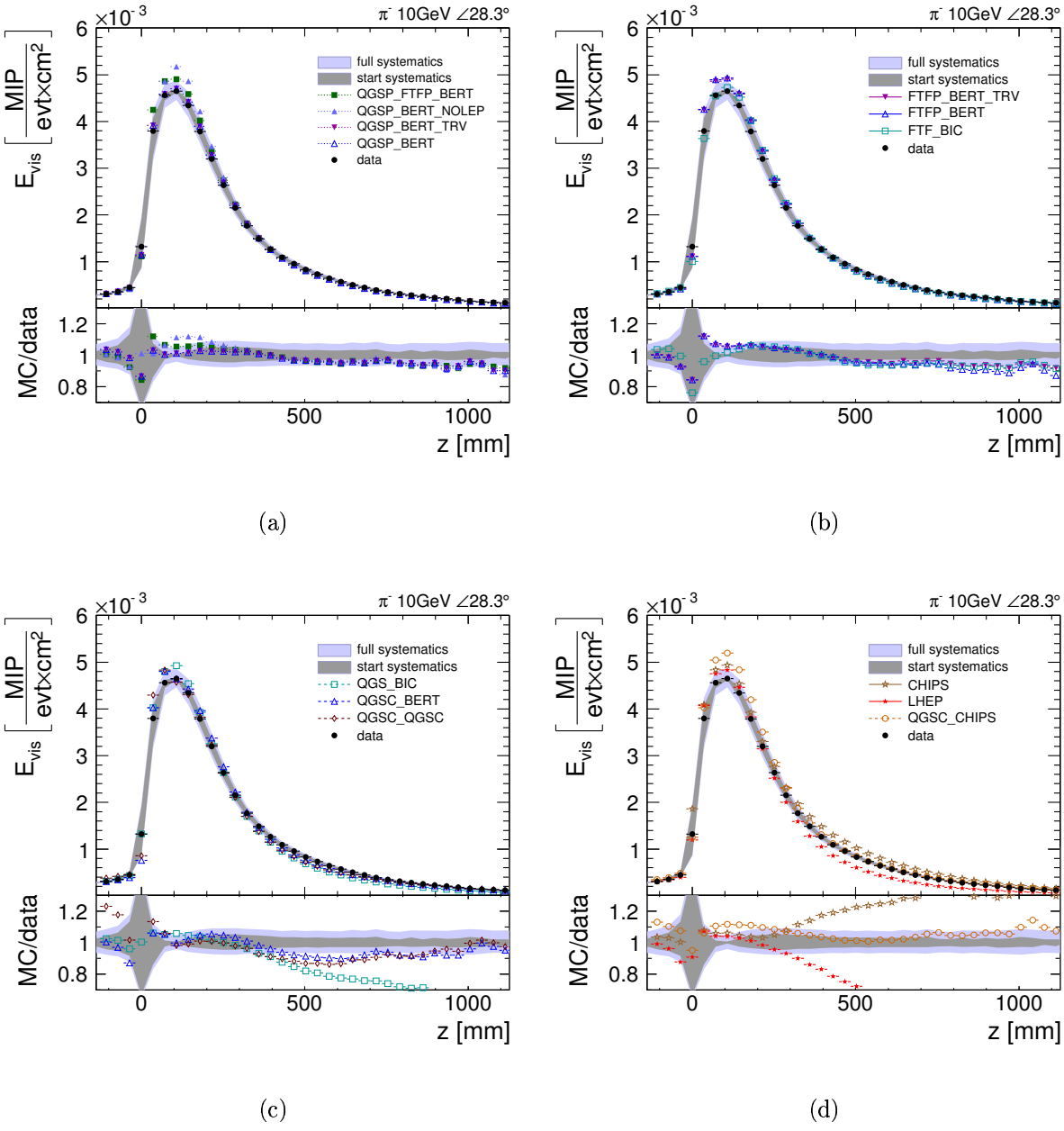

Figure 9.8: Comparison of simulation predictions to test-beam measurements. The longitudinal profile measured from shower start is compared to simulations using different Geant4 physics lists. The energy density of 10 GeV pion showers is drawn versus the longitudinal position z. The lower plots show the ratio of simulation over data.
(a) Simulations with the QGSP models.
(b) Simulations with the FTF models.
(c) Simulations with the QGSC models.
(d) Simulation with the CHIPS models and the LHEP model.

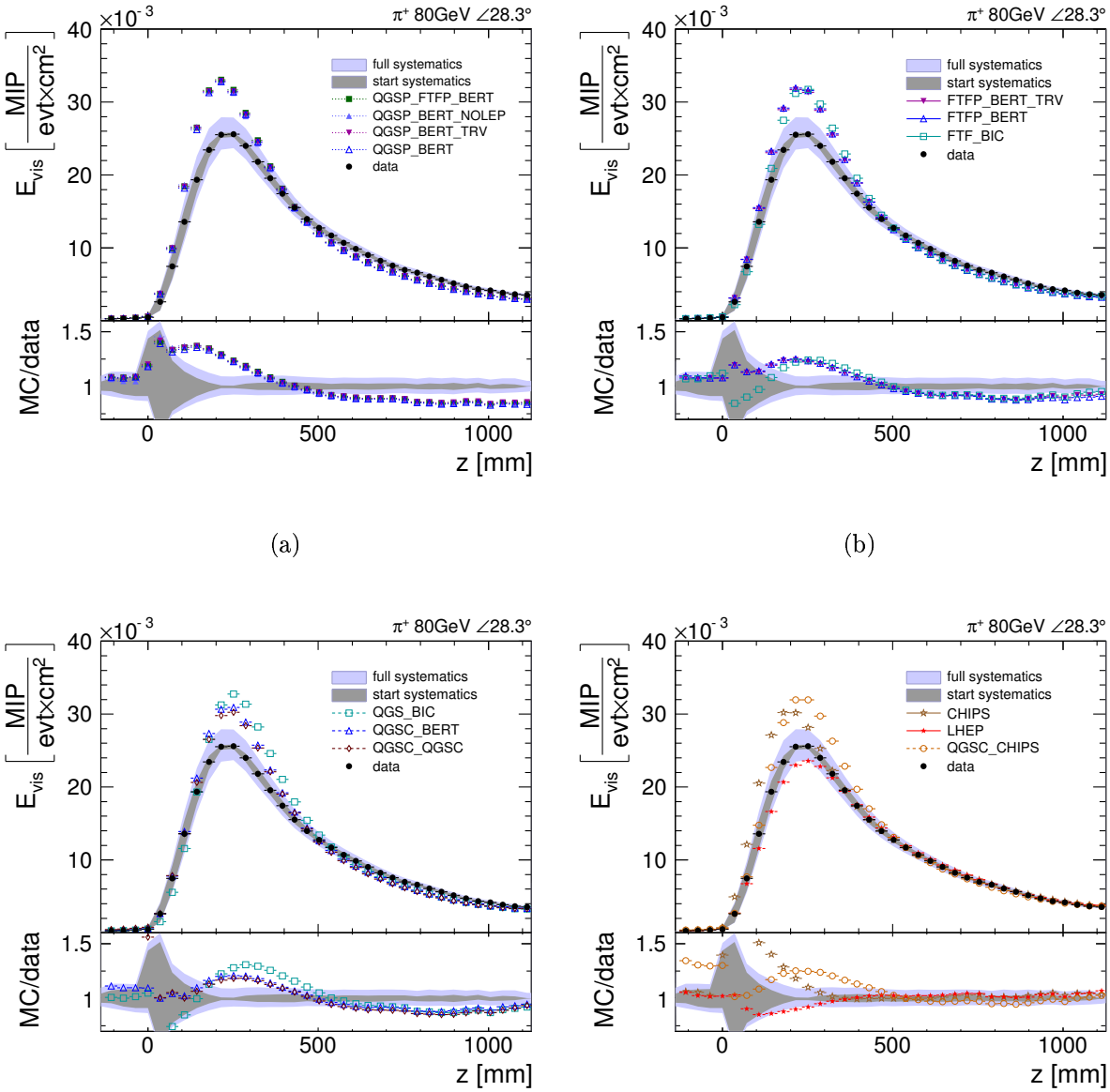

Figure 9.9: Comparison of simulation predictions to test-beam measurements. The longitudinal profile measured from shower start is compared to simulations using different Geant4 physics lists. The energy density of 80 GeV pion showers is drawn versus the longitudinal position z. The lower plots show the ratio of simulation over data.
(a) Simulations with the QGSP models.
(b) Simulations with the FTF models.
(c) Simulations with the QGSC models.
(d) Simulation with the CHIPS models and the LHEP model.

9.3.4 Differential Longitudinal Profiles

The projections of the showers in one dimension have been discussed so far. Both, longitudinal and transversal profiles exhibit significant discrepancies between simulation and measurement, particularly at energies above 20 GeV. The AHCAL data offer to investigate further where the exact location of the discrepancies is. To achieve this, the longitudinal profiles are generated for different radial positions.

All the simulations show an excess in the region of the longitudinal peak position for energies higher than 20 GeV. At the same time the radial profile shows a plus in energy in the shower centre and a deficiency at larger radii for many physics lists. Figure 9.10 displays the longitudinal profile for different radial rings and compares it to simulations with FTF based physics lists. The main discrepancy is at the core of the shower maximum, as the observations in longitudinal profile and radial profile suggested. For larger radii the longitudinal shape is described better.

A different situation can be observed in the case of the CHIPS physics list. The simulation shows more visible energy than the measurement at all radial distances. Additionally, the shower peaks before the measured shower for small radii and shifts with increasing radius. Between 12 cm and 18 cm the simulated peak position is already significantly behind the measured peak position. Figure 9.11 displays the situation for the CHIPS, LHEP, and QGSC_CHIPS physics list. Also the LHEP model shows a changing behaviour at different radial distances. The shower develops too long in the core and too short at radii larger than 18 cm. This situation is not visible in the one dimensional longitudinal profile. Simulations with QGSC_CHIPS show an excess in the core and an excess for large radii while the profile is too short in the medium range.

The good sensitivity of the differential profiles becomes obvious in the case of the 10 GeV profiles. Figure 9.12 shows the results from simulations with QGS_BIC, QGSC_BERT, and QGSC_QGSC. The longitudinal profile disfavoured QGS_BIC because of a poorly matching tail. Looking at the differential profiles, a large discrepancy in the amplitude of the longitudinal profile at medium radii becomes visible. QGS_BIC performs better than the other lists in the group, which was not visible in the full longitudinal profile.

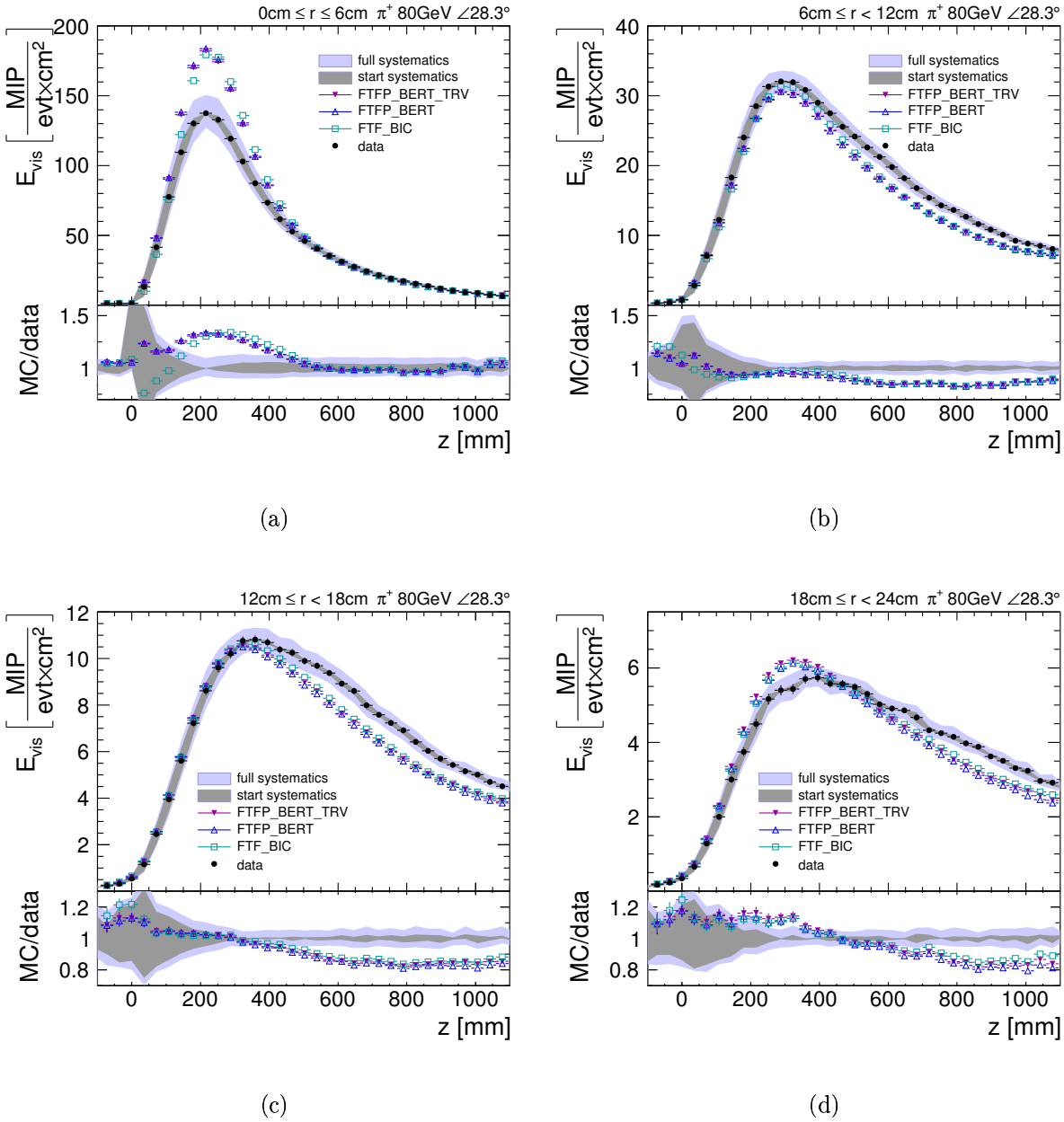

Figure 9.10: Comparison of simulation predictions to test-beam measurements. The longitudinal profile from shower start is measured for different radial distances to the calorimeter centre r. The energy density is plotted versus longitudinal position z. The measurements are compared to simulations using the FTFP_BERT, FTF_BIC, and the FTFP_BERT_TRV physics lists. The lower plots show the ratio of simulation over data.
(a) $0\,\text{cm} \leq r < 6\,\text{cm}$
(b) $6\,\text{cm} \leq r < 12\,\text{cm}$
(c) $12\,\text{cm} \leq r < 18\,\text{cm}$
(d) $18\,\text{cm} \leq r < 24\,\text{cm}$

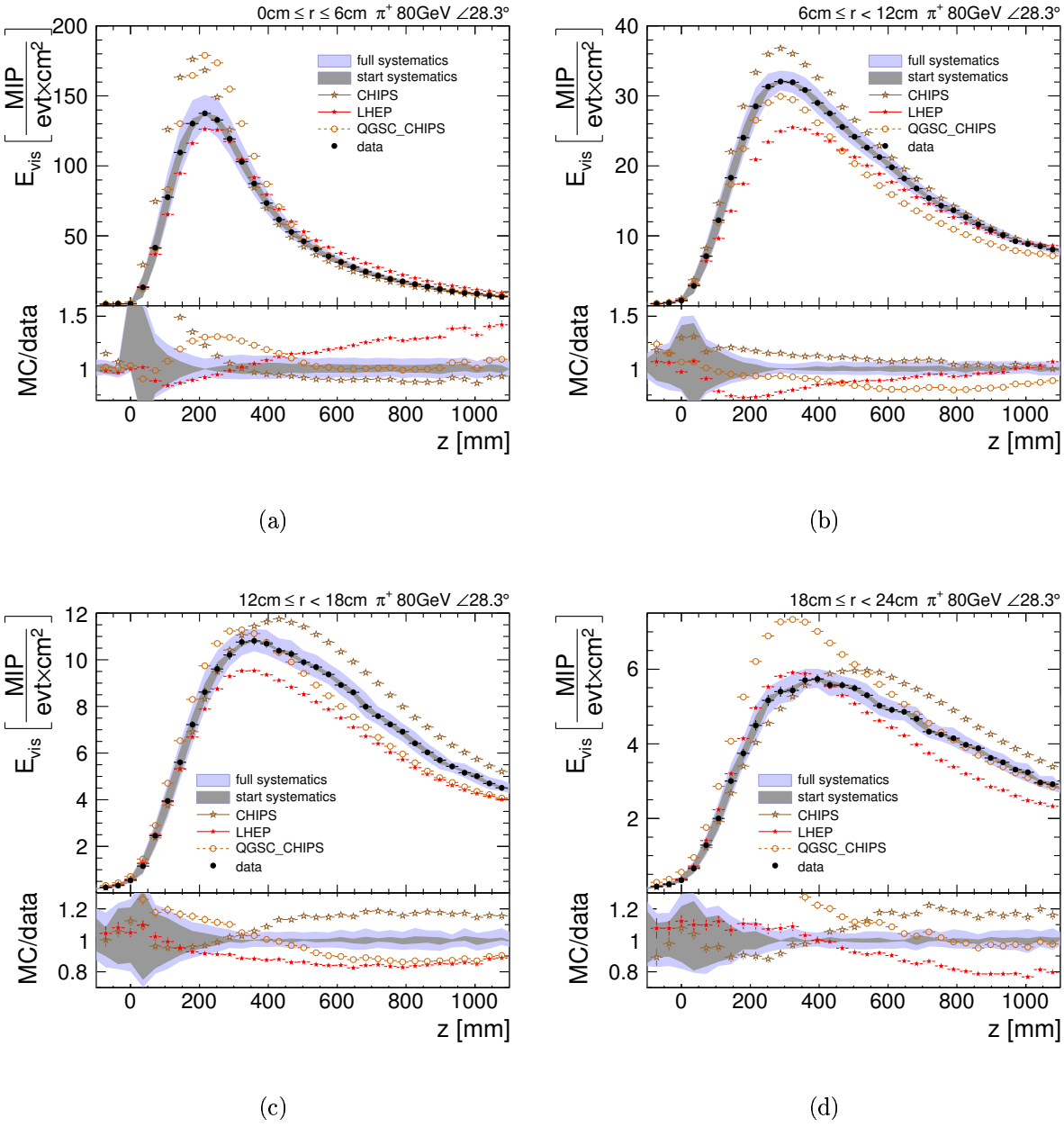

Figure 9.11: Comparison of simulation predictions to test-beam measurements. The longitudinal profile from shower start is measured for different radial distances to the calorimeter centre r. The energy density is plotted versus longitudinal position z. The measurements are compared to simulations using the CHIPS, QGSC_CHIPS, and the LHEP physics lists. The lower plots show the ratio of simulation over data.
(a) $0\,\text{cm} \leq r < 6\,\text{cm}$
(b) $6\,\text{cm} \leq r < 12\,\text{cm}$
(c) $12\,\text{cm} \leq r < 18\,\text{cm}$
(d) $18\,\text{cm} \leq r < 24\,\text{cm}$

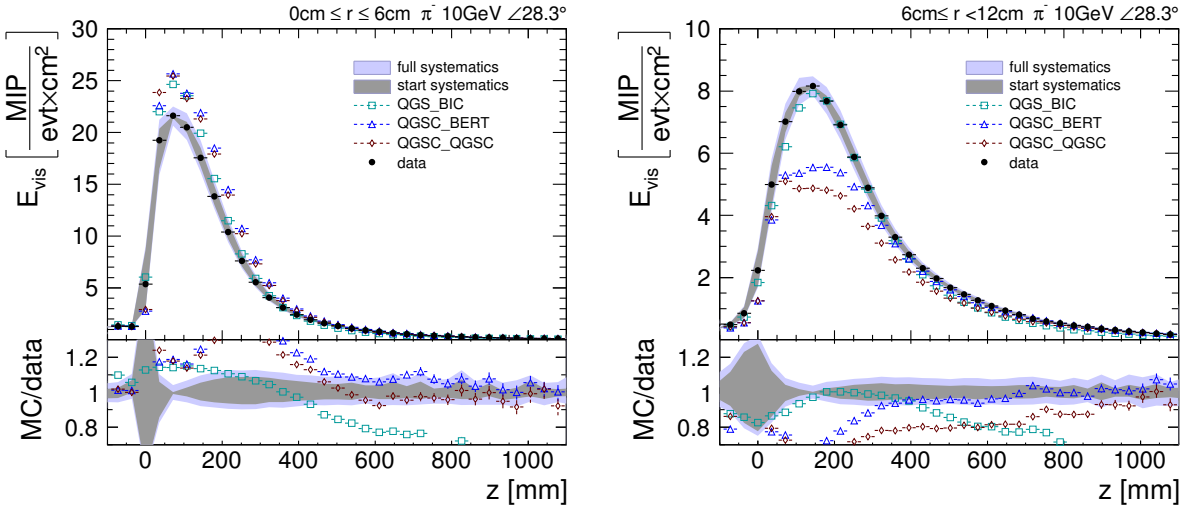

(a) (b)

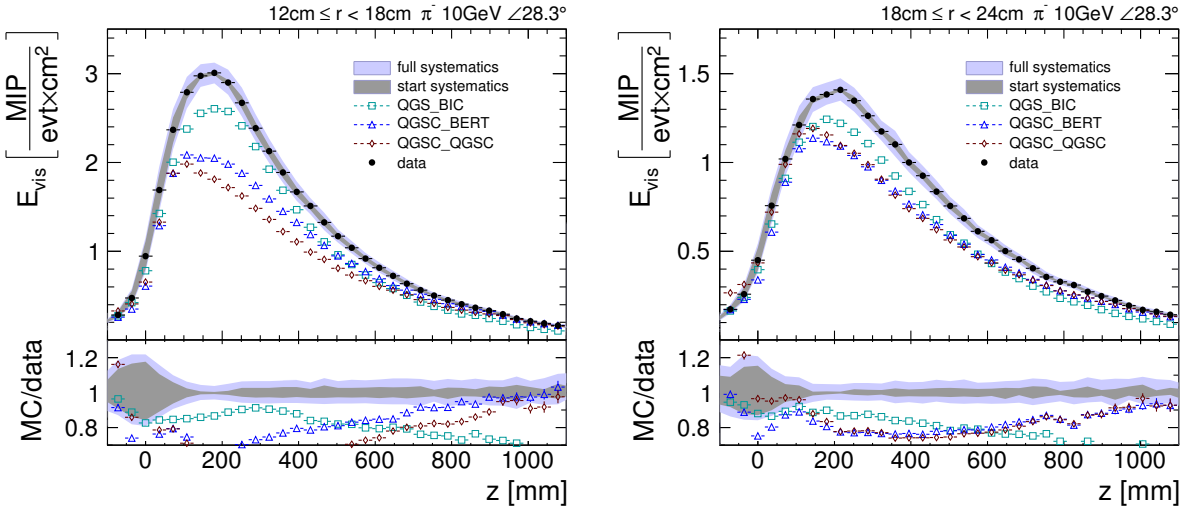

(c) (d)

Figure 9.12: Comparison of simulation predictions to test-beam measurements. The longitudinal profile from shower start is measured for different radial distances to the calorimeter centre r. The energy density is plotted versus longitudinal position z. The measurements are compared to simulations using the QGSC_BERT, QGSC_QGSC, and the QGS_BIC physics lists. The lower plots show the ratio of simulation over data.
(a) $0\,\text{cm} \leq r < 6\,\text{cm}$
(b) $6\,\text{cm} \leq r < 12\,\text{cm}$
(c) $12\,\text{cm} \leq r < 18\,\text{cm}$
(d) $18\,\text{cm} \leq r < 24\,\text{cm}$

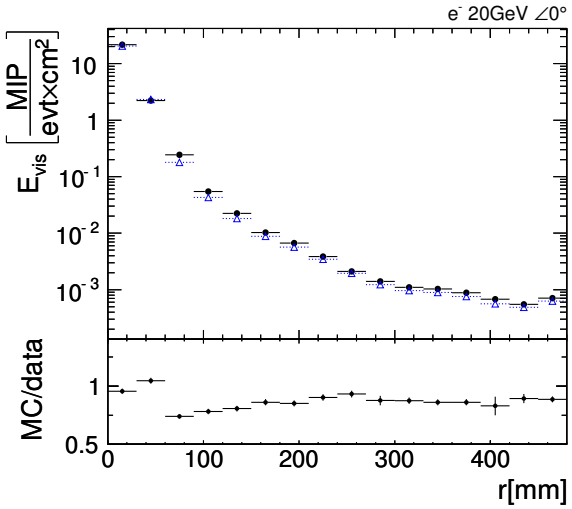

Figure 9.13: Radial profile of electromagnetic showers. Showers of 20 GeV electrons are confronted to simulations with the QGSP_BERT physics lists. The lower plot shows the ratio of simulation over data.

9.4 Conclusions

The results from the confrontation of simulation with data are summarised in table 9.1. None of the studied physics list describes the data perfectly. Especially, the shape of high energetic showers is not predicted within the assumed systematic uncertainties.

The systematic error assumptions are tested in section 6.3 with electromagnetic simulations. The total response and the maximum of the longitudinal profile are well within the systematic uncertainties for electromagnetic showers up to 50 GeV. But, studies of the radial profile show some discrepancies between measurement and electromagnetic simulation. Figure 9.13 shows the radial profile of 20 GeV electromagnetic showers confronted to simulations taken from the work of [61]. If the source of the discrepancies lies in the simulation, is not fully understood. The accuracy of electromagnetic simulations is expected to be much better than hadron shower simulations. Therefore, deviations of this size are surprising. The exact source of the discrepancies is currently under investigation. Unless, this issue is settled a final conclusion on the radial performance of the hadron simulation is not possible.

Nevertheless, several conclusions can be drawn from the studies. There are clear performance differences between the models. For example, the recently developed CHIPS physics list shows several strong deviations in the performed tests. In summary, it is the list with the worst performance. At the same time this model shows interesting alternative behaviour in situations where all established models cannot fully describe the measurements, like the form of the energy response. The tests also include two predecessors of the CHIPS physics list, QGSC_CHIPS and QGSC_QGSC. These models perform significantly better in some aspects than the current version of CHIPS. This gives the hope that there is still some room for improvements in this interesting ansatz. Future developments have to show if the CHIPS model can be a competitive approach to describe hadron showers.

The LHEP physics list performs only slightly better than CHIPS, which is not surprising as it is not considered the state of the art approach for simulation. But these performance deficiencies are still of relevance, as the LHEP models are still in use in many physics lists.

The best results are achieved with the FTF and QGS based physics lists, where the lists based on the FTF model perform slightly better than the QGS models. One reason for the difference could be that the QGS models do not need the LEP model between the high and low energy models. The different variants of QGSP_BERT show that indeed some aspects can be improved by changing the transition region between the models. But all variants have at least one aspect where the performance could be improved.

physics list	shower start	energy				shower shape			
		response		resolution		radial†	longitudinal		2D
		$< 20\,\mathrm{GeV}$	$> 20\,\mathrm{GeV}$	energy dependence	leakage correction		$< 20\,\mathrm{GeV}$	$> 20\,\mathrm{GeV}$†	
CHIPS	$\oplus$	$\ominus\ominus$	$\ominus\ominus$	$\ominus\ominus$	$\ominus\ominus$		$\ominus\ominus$	$\ominus$	$\ominus$
FTF_BIC	$\oplus$	$\oplus$	$\oplus$	$\oplus$	$\oplus$		$\oplus$	$\ominus$	
FTFP_BERT	$\oplus$	$\oplus$	$\oplus$	$\oplus$	$\oplus$		$\oplus$	$\ominus$	
FTFP_BERT_TRV	$\oplus$	$\oplus$	$\oplus$	$\oplus$	$\oplus$		$\oplus$	$\ominus$	
LHEP	$\ominus$	$\ominus\ominus$	$\oplus$	$\ominus$	$\ominus$	$\ominus\ominus$	$\ominus\ominus$	$\oplus$	
QGS_BIC	$\oplus$	$\ominus$	$\oplus$	$\oplus$	$\ominus$		$\ominus$	$\ominus$	
QGSC_BERT	$\oplus$	$\ominus$	$\oplus$	$\ominus$	$\ominus$		$\oplus$	$\ominus$	$\ominus\ominus$
QGSC_CHIPS	$\oplus$	$\ominus$	$\oplus$		$\oplus$	$\ominus$		$\ominus$	$\ominus\ominus$
QGSC_QGSC	$\oplus$	$\ominus$	$\oplus$	$\ominus\ominus$	$\ominus$	$\ominus\ominus$	$\oplus$	$\ominus$	$\ominus\ominus$
QGSP_BERT	$\oplus$			$\ominus$	$\oplus$		$\oplus$	$\ominus$	$\oplus$
QGSP_BERT_NOLEP	$\oplus$	$\oplus$		$\ominus$	$\oplus$			$\ominus$	
QGSP_BERT_TRV	$\oplus$	$\oplus$		$\ominus$	$\oplus$		$\oplus$	$\ominus$	
QGSP_FTFP_BERT	$\oplus$	$\oplus$		$\ominus$	$\oplus$		$\oplus$	$\ominus$	$\oplus$

† *The reliability of these measurements is currently under discussion. See the text for further information.*

Table 9.1: Summary of the confrontation of simulation and measurement for different Geant4 physics lists. The performance of the lists is tested for proper prediction of shower start, energy response and resolution including leakage correction, and the shower shape. Following symbols are used to indicate the performance: $\oplus$ means that the simulation and measurement agree within errors; $\ominus$ is used in the case that significant deviations between simulation and measurement are present; $\ominus\ominus$ indicates that strong deviations are present, especially when one model performs much worse than the rest; no sign is given when the deviations are only slightly larger than the systematic errors.

Chapter 10

Next Generation Readout Electronics

A new ASIC for SiPM readout, called SiPM Integrated Readout Chip (SPIROC), is developed in the CALICE collaboration [62]. It is the successor of the chip used for the AHCAL prototype (FLC-SiPM) [63]. While the FLC-SiPM is a purely analogue chip, the new chip design aims at a fully integrated readout system providing trigger, zero suppression, and digitisation. The compact design and a very low power consumption allow to built the SPIROC into the detector. This is important to reduce the amount of dead regions and to increase the homogeneity of the detector.

While the general working principle of the analogue amplifier is unchanged with respect to the previous chip, the implementation was redesigned to reach the necessary reduction in power consumption. The changes affect all stages of the amplifier, thus the performance of the system has to be reevaluated. The extension of the chip to a full readout system also adds additional components that have to be tested. This work includes the characterisation of the analogue components inside the first SPIROC prototype samples.

This chapter describes the chip layout and the studied quantities. The requirements for an operation inside an ILC calorimeter are discussed and motivated by the experiences from the AHCAL construction and operation.

10.1 Layout of the SPIROC

Figure 10.1 sketches the layout of the SPIROC. The voltage at the chip input can be varied with an 8 bit DAC between 0 V and 5 V. This allows to compensate operation voltage differences between the individual SiPMs. The input signal is coupled via capacitors to two amplifier chains. The size of the capacitors is chosen 1:10 to achieve a factor of ten gain difference between the two amplifier chains. The amplifier gains can be individually adjusted in 15 steps by selecting different feedback capacitors. Both amplifier stages are connected to a CR-$(RC)^2$ shaper with variable shaping time. The peaking time can be varied between 25 ns and 175 ns in steps of 25 ns. The output of the shapers is connected to a sample and hold stage, which can store up to 16 values.

The trigger for the sample and hold stage is generated in a special trigger chain connected to the high gain amplifier. The signal is sent to an additional shaper with 15 ns time constant. The output of this fast shaper is compared to a reference voltage. The trigger level can be set with a 10 bit DAC common to all channels and a 4 bit individual

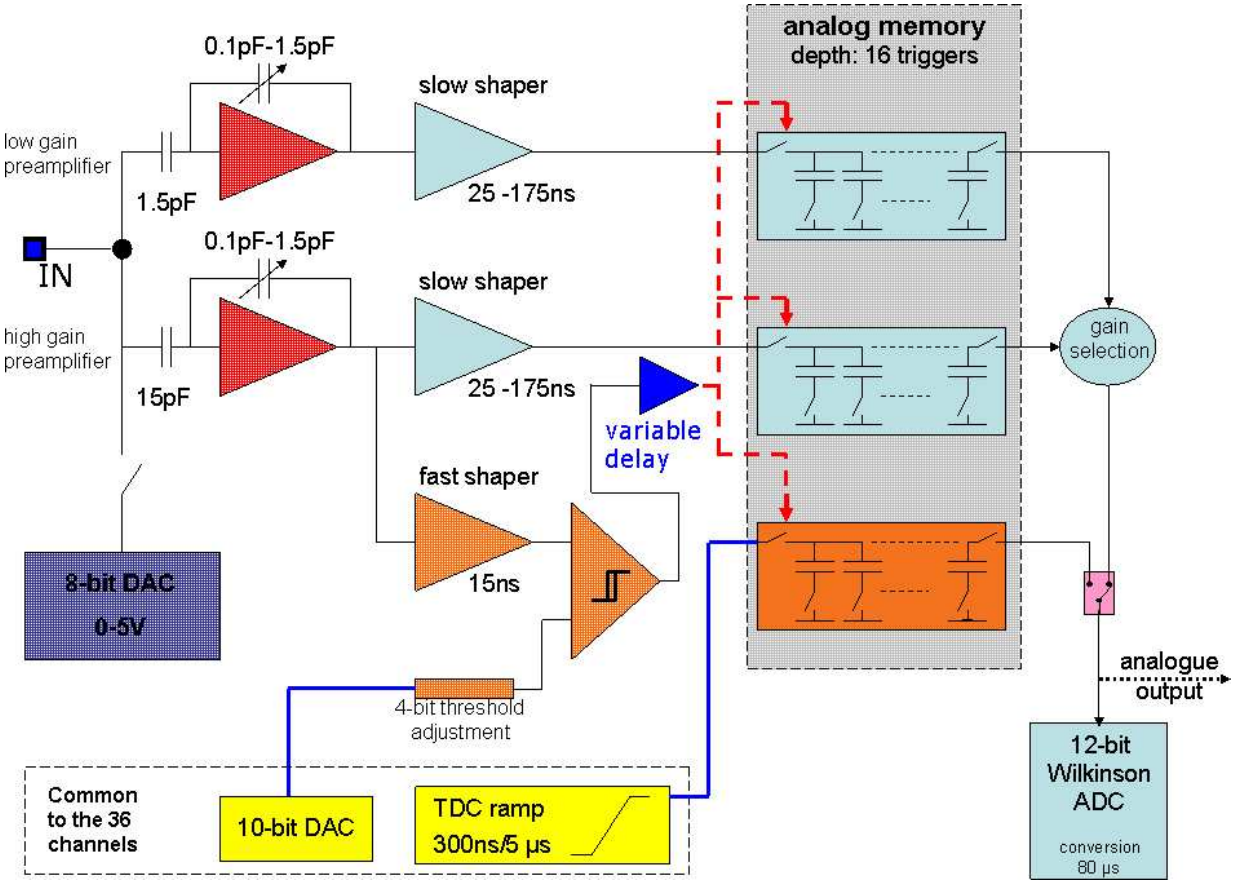

Figure 10.1: Layout of the SiPM Integrated Read Out Chip, SPIROC.

adjustment. A variable delay allows to adjust the sampling time to the maximum of the slow shaper output. Additionally to the amplifier signals, the voltage of a linear ramp is stored to a third sample and hold stage. The ramp is started with a reference clock, thus the stored value corresponds to the time of the trigger.

The chip includes a Wilkinson ADC to digitise the voltages stored on the sample and hold stages. Two out of the three chains can be chosen for digitisation. During normal operation, an automatic gain selection chooses the amplifier chain with suitable dynamic range for digitisation. The signal can be sent to an analogue output instead of the Wilkinson ADC.

10.2 General Considerations

The performance requirements of the chip depend on the input signals and the desired quality of the output signal. Before the single components of the SPIROC are tested, some general aspects of semiconductor photomultiplier signals and the required readout system performance are discussed for the case of an ILC calorimeter.

source	pixel	gain			unit
		0.25	0.5	1.0	[Me]
	1	0.04	0.08	0.16	[pC]
1 MIP	13	0.52	1.04	2.08	[pC]
full SiPM	1156		93	185	[pC]
full MPPC	3000	120	240		[pC]

Table 10.1: Relevant signals for the calorimeters read with semiconductor photomultipliers.

10.2.1 Input Signals

This section will discuss the signals of SiPMs relevant for the amplifier design. The general properties of SiPMs are described in chapter 3. Possible candidates for applications with the SPIROC are the MEPhI/Pulsar SiPM, the Hamamatsu MPPC, and the CPTA MRS. Experience from the AHCAL test-beam calorimeter and laboratory measurements show typical pixel gains of 0.5 to 1 million electron charges (Me) for the SiPM with 1156 pixels (see figure 3.2(a)). The MPPC gain is more around 0.25 Me and has a total amount of 1600 pixels. While the pixel dead time of the SiPM is large enough to ensure that each pixel can fire only once during an event, the MPPC pixel can fire several times increasing the effective amount of pixels. Experience with the CPTA MRS is still small in the CALICE collaboration. Therefore, the discussion will cover only SiPM and MPPC.

The operation of the semiconductor photomultipliers inside a calorimeter puts several requirements on the readout system. The amplifier has to resolve the signal of a single pixel to measure the voltage and temperature dependent pixel gain. On the other end of the scale, signals up to full saturation of the photo-sensor have to be amplified linearly. This is especially important to allow an accurate correction of the photo-sensor non-linearity. The experience with the AHCAL prototype showed, that an accurate measurement of the photo-sensor saturation level is crucial to minimise the systematic calibration uncertainties.

The signal generated by a minimum ionising particle is another important operation point. The calorimeter cells are calibrated to the size of this signal. Therefore, it is important that the readout system is linear at this point, and gives a good signal to noise ratio. Table 10.1 shows an overview of the signals and their sizes in charge.

10.2.2 Determination of Operation Parameters

The SPIROC has a large number of steering parameters that allow to adjust the chip to different input signals. This makes it a very flexible device, but methods to optimise the operation parameters have to be developed. Uncertainties in these methods will play a role in the total system performance. The most important parameters are:

Shaping time The time constant of the shaper directly influences the amplifier noise. A shorter time constant reduces the bandwidth of the amplifier and thus the equivalent noise charge. An optimal matching of the signal bandwidth and the amplifier bandwidth is necessary to achieve the best signal to noise ratio.

Trigger threshold The first step in the signal processing is the trigger decision. The accuracy of the applied threshold and its stability will influence the measurement

in several means: A too high threshold will reduce the signal detection efficiency; a too low threshold will increase the amount of noise hits; the jitter and offset of the trigger time t_0 depend on the threshold stability and value.

Hold After the trigger decision is taken the signal will be stored for later digitisation. To reach the best performance it is important to hold the signal at the peak maximum of the shaped output signal. This gives the highest gain and is the least sensitive point for variations in timing. As the time of the output signal maximum changes with different types of SiPM, it is important to measure and accurately set the time t_{hold} at which the analogue output will be sampled.

Amplifier gain and gain mode selection The SPIROC design includes two analogue amplifier chains for each channel to combine a high resolution with a large dynamic range. Depending on the size of the recorded signal the output of the better suited chain will be digitised. The gain settings for the different chains and the threshold for the transition from the high to the low gain chain has to be optimised for best resolution and linearity.

A shaping time of 50 ns is selected for this study. The choice is motivated by the signal shapes observed with scintillator-SiPM/MPPC-systems. This choice ensures that the main peak of the signal is shorter than the shaping time and that possible signal shape changes do not significantly affect the recorded signal fraction. Section 3.2.3 gives an overview over the signal shape and possible signal induced shape variations. A smaller shaping time would give the risk of non-linearities. A longer shaping times would mainly increase the integrated noise and deteriorate the signal to noise ratio. Also the probability for pileup increases with a longer shaping time.

Detailed studies of the trigger thresholds have not been possible with the samples available for this work. The studies are included in later work [64]. The chip performance for different gain and hold settings is studied in this work. The studied quantities are described in the next section.

10.2.3 Benchmark Parameters

The first prototype of the SPIROC suffers from problems in setting the operation parameters and a bug in the digitisation circuitry. This restricts the possible tests significantly. The internal digitisation chain is unusable. Also the trigger threshold optimisation and the automatic gain selection are not operational. Therefore, the following properties are chosen for this study:

- The linearity and the dynamic range of the input DAC.
- The gain in the different amplifier chains for the different amplifier settings.
- The linear range for different operation settings.
- The noise of the chip for different amplifier gains.

The linear range of the input DAC defines the maximum variance of the SiPM operation voltage that can be connected to a common bias voltage. The linearity of the DAC defines the accuracy of the operation voltage supplied to the photo-sensor. The response changes 5.6 % per 100 mV for the SiPMs used inside the AHCAL [27]. This gives an upper limit for the acceptable non-linearity of approximately 15 mV, if the uncertainty should be restricted to 1 %.

The signal to noise ratio is given by the gain and noise of the amplifier. The most challenging signal is a single pixel charge. The separation of the single pixel peaks in a low light spectrum has to be good enough to allow a stable and automatic fitting of the photo-sensor gain. The experience with the AHCAL shows that the signal to noise ratio should be at least 4 to achieve reasonable efficiencies [25, 27, 65].

The linear range of the amplifier has to be large enough to cover a fully saturated photo-sensor. A combination of gain settings has to be found for the two amplifier stages which gives a smooth matching of the two.

Chapter 11

Test Bench Setup for the Characterisation of the SPIROC

A test bench is set up for the SPIROC characterisation. The main components are a digital pulse generator, a VME DAQ system, and a SPIROC specific test board. The test board supplies and steers the SPIROC. The pulse generator is used to generate test signals and to trigger the sample and hold in the chip. The analogue output signals are digitised with an on-the-shelf ADC. A custom made amplifier is used to increase the sensitivity in the noise measurements. A high ohmic multimeter allows to measure the voltage of the input DAC.

This section describes the listed components including their calibration for the later measurements. The measurement setups are explained.

11.1 Test Board

The central part of the test bench is the SPIROC test board. It hosts and supplies the chip under test. Figure 11.1(a) shows a picture of the test board. The chip is mounted in a special socket, which allows to exchange the chip without soldering. The board comprises an ALTERA micro controller which steers the SPIROC. The micro controller communicates with a control PC over a USB connection. A complex set of operation parameters can be set with a LabVIEW based slow control software. The parameters relevant in this work are: the selection of the readout channel, the selection of the amplifier chain (high or low gain), the setting of the variable amplifier gain, the setting of the shaper time constant, and the input DAC value. The board has an input connection for an external triggering of the track and hold stage. The analogue output signal of the selected SPIROC channel is available via the test board.

The presence of the micro controller principally allows to do automatised and flexible measurements. This feature has been used to scan the input DAC voltage. Unfortunately, the USB connection couples noise into the system, such that the gain, linearity, and noise measurements have to be performed with the ALTERA offline.

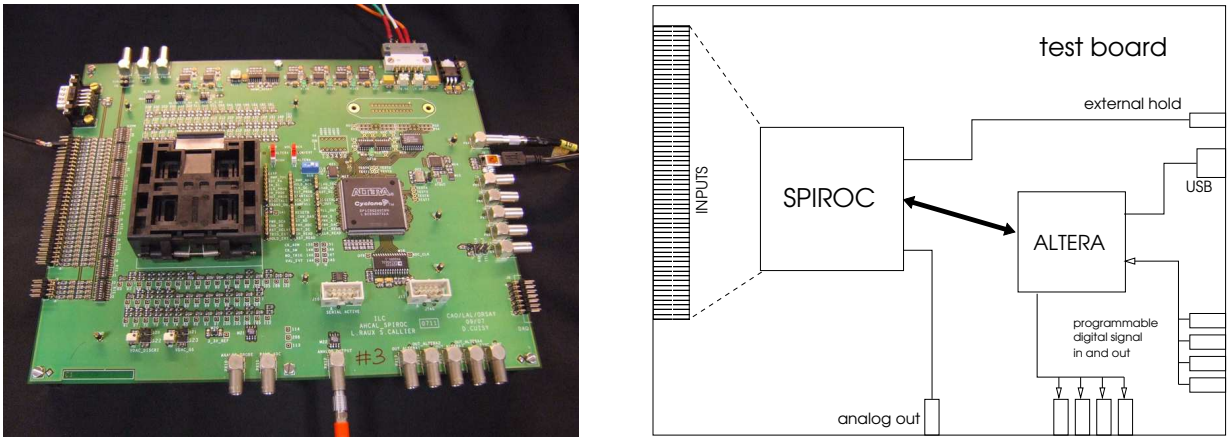

(a) (b)

Figure 11.1: (a) Photograph of the SPIROC test board. (b) Functional layout of the SPIROC test board.

11.2 Pulse Generator and Test Signal Generation

The test signals are generated with the digital delay/pulse generator SRS DG535 [66]. The device offers rectangular signals of variable amplitude and width. The delay between different outputs and the width of the signal can be adjusted over a wide range with an accuracy of 5 ps. This allows to generate both the test signal and the trigger for the SPIROC sample and hold with the same device. The amplitude and the delay can be remotely set over a GPIB interface, which is used to make automatised scans with varying signal amplitudes and hold times.

The test signal is generated by sending the pulser signal over a capacitor, to mimic the shape of a SiPM signal. The leading edge of the resulting signal is defined by the slew rate of the pulser. The achieved rise time is 2 ns to 3 ns, depending on the chosen amplitude. The width of the signal can be chosen by the size of the capacitor which discharges over the 50 Ω termination resistor at the SPIROC input. A 100 pF capacitor is used resulting in a decay constant τ=5 ns. Figure 11.2 shows the schematics of the signal generation and sketches the pulser signal and the resulting signal.

The charge Q of the pulse can be calculated from the capacity C and the voltage difference V between the high and the low level of the generator pulse:

$$Q = V \cdot C. \tag{11.1}$$

Attenuators are used to adjust the pulser amplitude range to the required input signal range.

All used amplitude settings are calibrated with the help of the DAQ. The high and low level of the pulser signal are measured with the ADC. This gives an accurate calibration of the test charge. Without the calibration of the individual amplitudes, the differential non-linearity of the pulse generator would dominate the linearity measurement at low charges.

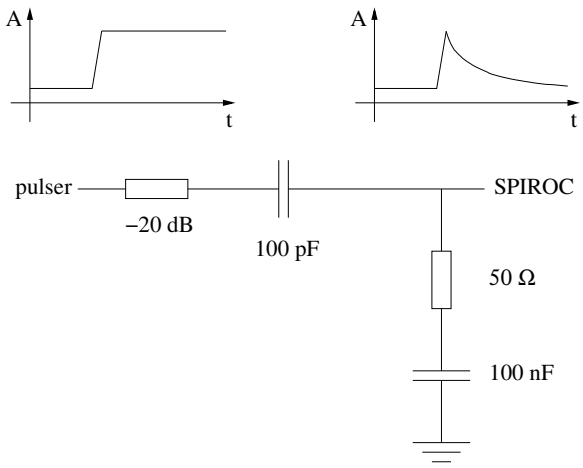

Figure 11.2: Schematics of the test signal generation. The pulse shapes at the output of the pulser and at the input of the SPIROC are sketched above.

11.3 Data Acquisition System

The DAQ system consists of standard VME and NIM components. A CAEN V785N [67] ADC module is used to record the SPIROC output voltage. The gate for the ADC is generated with a LeCroy Model 222 gate generator module [68]. The recorded data are transferred via a CAEN 2718 VME-PCI-bridge to a readout PC [69]. A readout software was developed for the measurements. It features interactive and batch mode operation of the DAQ. The data are stored in root trees. A synchronised reading of several cards is possible.

The response and linearity of the ADC card is measured with the help of the programmable calibration source DIGISTANT Typ 4462. The calibration source offers voltages with an accuracy better than 1 ‰. Figure 11.3(a) shows the measurement. The linearity is better than 5 ‰ for results between 300 and 3950 ADC units. Each ADC unit corresponds to (1.003073±1e-6) mV. The noise of the ADC is measured with a 1.5 V alkaline battery at the input. This method allows to measure the noise of the ADC in the linear region. The noise follows a Gaussian distribution. The width of the distribution σ_{noise} is (0.549±0.003) ADC, which corresponds to an input noise of (0.551±0.003) mV.

11.4 Custom Made Amplifier

The input noise of the ADC is too large to directly measure the noise of the SPIROC. To enhance the signal to noise ratio of the DAQ system, a low noise amplifier was built based on the AD8052 microchip [70]. The schematics of the custom made amplifier are shown in figure 11.4. The design is chosen to be non-inverting and allows to subtract an offset voltage from the input. Two different amplifier gains can be selected.

The response and noise of the amplifier and ADC are measured similarly to the measurement of the ADC alone. Figure 11.5 displays the response measurement. The non-linearity in the measurement corresponds to the non-linearity of the ADC. The amplifier adds no

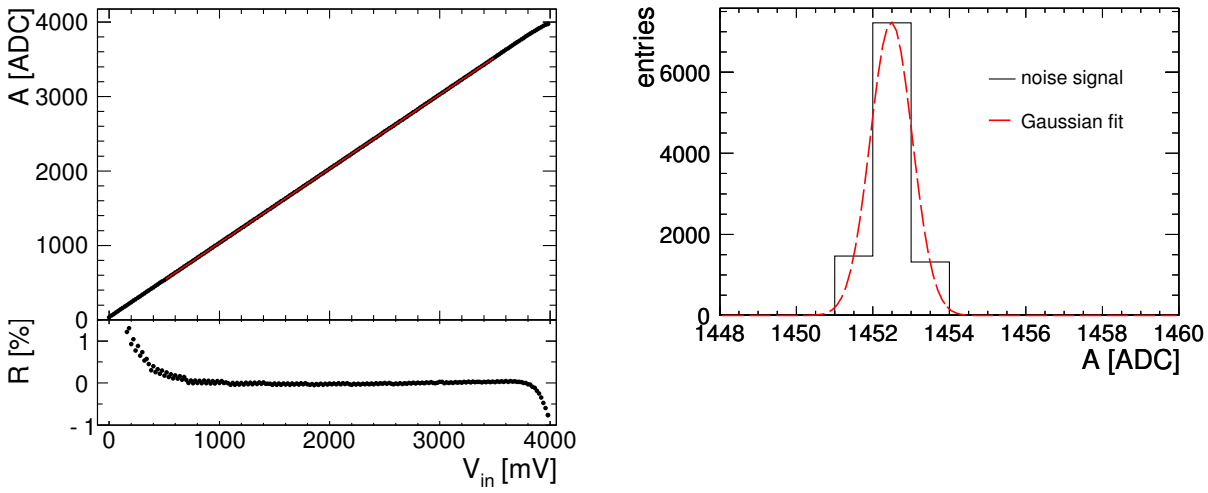

(a) (b)

Figure 11.3: (a) Response of the CAEN V785N ADC module. The measured value A is plotted against the calibration voltage V_{in}. The lower plot shows the residual R to a linear fit in the central range. (b) Noise of the CAEN V785N ADC module. The signal distribution of a 1.5 V battery is measured and fitted with a Gaussian.

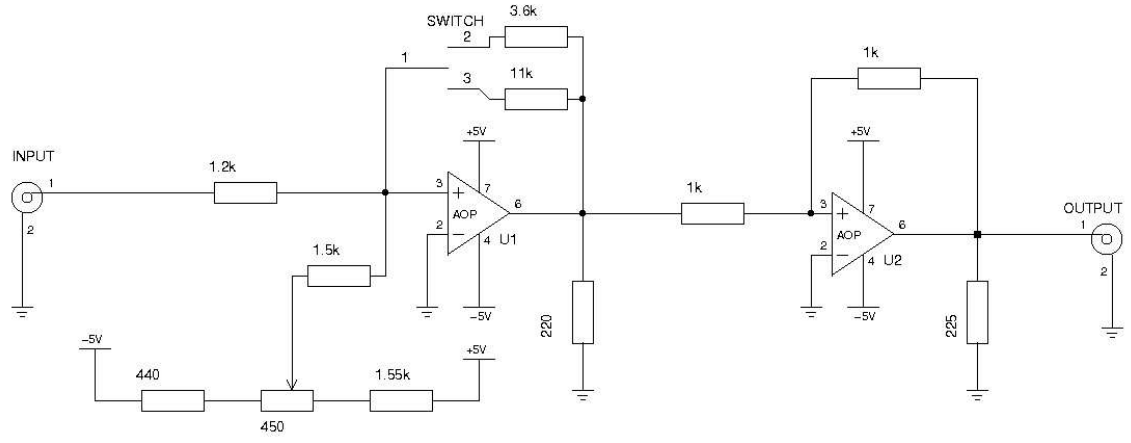

Figure 11.4: Schematics of the custom made amplifier.

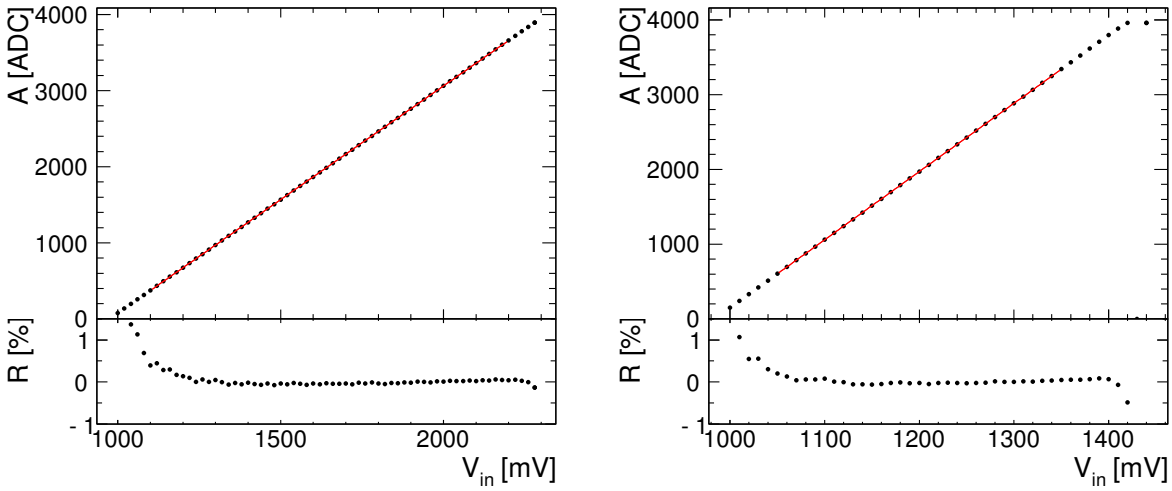

(a) (b)

Figure 11.5: Response of the custom made amplifier for two different gain settings: (a) ×3 and (b) ×9. The lower plot shows the residual to the linear fit of the central region. The observed non-linearities are caused by the ADC used to measure the response.

measurable non-linearities. The calibration gives an amplification of 2.996140±0.000003 in the low gain mode and 9.14821±0.00002 in the high gain mode. The noise of the combined system of amplifier and ADC is (0.565±0.003) ADC in the low gain mode and (0.753±0.005) ADC in the high gain mode. This corresponds to an input noise of (0.0825±0.0005) mV in the high gain mode.

11.5 Keithley Multimeter

The low current design of the SPIROC input DAC limits the maximum deliverable current to a value around 1 μA. Therefore, a measurement device with an input resistance in the GΩ range is necessary to avoid a bias of the measurement. The ADC cannot be used due to its input resistance of 1 kΩ. Instead, the Keithley 2001 Multimeter [71] was used to read the DAC voltage. It offers an input resistance larger than 10 GΩ for the relevant input voltage range. The accuracy of the device is better than 0.2 mV in the selected measurement range. The multimeter can be read by the SPIROC slow control software. This allows an automatised scan of the different DAC settings.

11.6 Measurement Setups

Gain, linearity, and hold optimisation measurements are performed with charge injection. Figure 11.6(a) sketches the measurement setup. The pulse generator is used to generate the test signal, the trigger for the track and hold stage, and the trigger for the ADC gate.

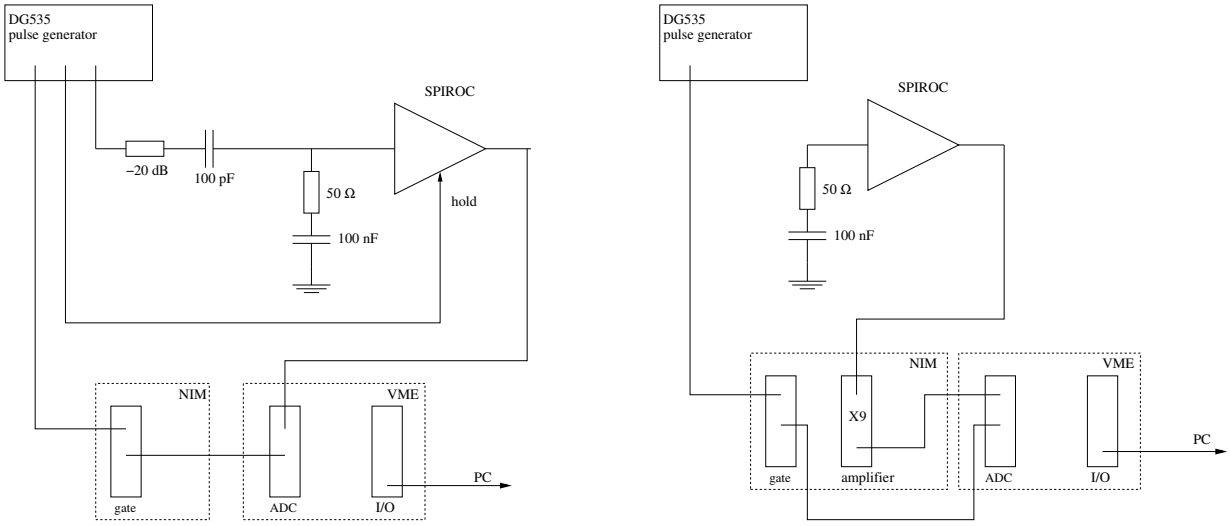

Figure 11.6: (a) Setup to measure the SPIROC response. Pulses with defined charge are sent to the SPIROC input. The track and hold of the SPIROC is triggered externally by the pulse generator. The analog output signal is recorded with the ADC of a VME DAQ system. The gate for the ADC is generated with a LeCroy gate generator.
(b) Setup to measure the SPIROC noise. All inputs are disconnected from the SPIROC. No track and hold is used. The output signal is amplified with a factor of 9 before it is recorded with the ADC. The readout system is randomly triggered by the pulse generator.

The pulse amplitude and the time of the hold can be set from the readout PC, which is used to do an automatic scan of the two parameters. The SPIROC settings have to be programmed manually and are fixed during one measurement cycle.

The noise measurement is performed with a factor of 9 amplification before the ADC. To reduce the external noise the ALTERA clock is switched off and the USB connection is removed. Additionally, all inputs are removed and the hold trigger is disconnected. The pulse generator is used to randomly trigger the readout system. Figure 11.6(b) shows the setup configuration.

Figure 11.7 depicts the electronically relevant circuitry of the SPIROC input DAC measurement. The current of the DAC is decoupled from the amplifier inputs with capacitors. The termination circuitry consists of the 50 Ω resistor and a 100 nF capacitor to prevent a DC current to ground. The current loop is closed by the multimeter input resistance, which has to be large enough to stay within the current limitation of the DAC.

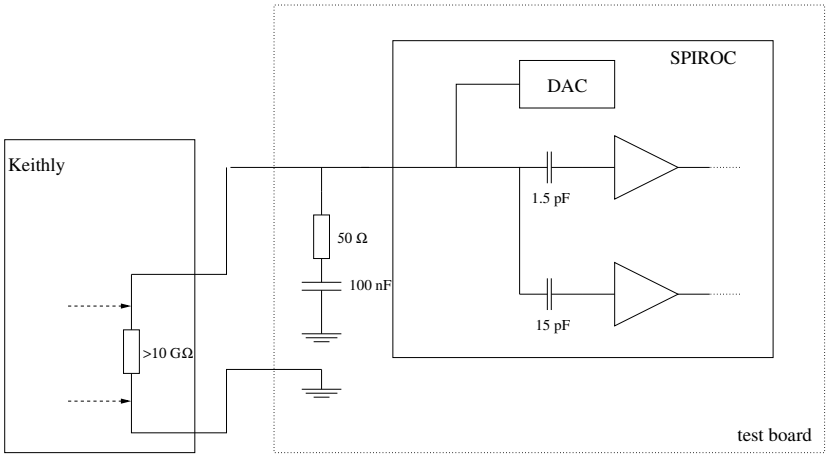

Figure 11.7: Setup to measure the SPIROC input DAC. The voltage at the SPIROC input is measured with a high ohmic multimeter.

Chapter 12

SPIROC – DAC and Analogue Performance

Semiconductor photomultipliers put stringent requirements on the performance of the readout system. The signal to noise ratio has to be large enough to resolve single pixel signals. At the same time the system has to be linear up to the saturation of the photomultiplier, to allow an accurate correction of the sensor non-linearity. The analog signal chain of the SPIROC is characterised using the test bench setup described in chapter 11. Also, the performance of the input DAC is evaluated. This chapter summarises and discusses the results from these measurements. The results are compared to the properties of the MEPhI SiPM that are used in the AHCAL. The values are taken from [27].

12.1 Input DAC

The quality of the input DAC defines how accurate the working point of the photomultipliers can be set. The output voltage V_{DAC} as a function of the programmed value is measured for all channels of the sample chip. Figure 12.1(a) shows the result including a calibration fit for a typical channel. The residual to the fit is displayed in figure 12.1(b). The DNL of all channels is presented as a histogram in figure 12.2(b). The RMS of the distribution is (31.9±0.2) mV. This would correspond to a smearing of the SiPM gain of (0.83±0.03) %, and a smearing of the SiPM response of (1.8±0.2) %. When interpreting this result it has to be considered that the distribution of the single channels are mostly not of Gaussian form. Figure 12.2(a) shows the distribution of the same channel presented in figure 12.1(a). The values group in two peaks which gives a larger typical error than one would expect from a Gaussian distribution. An estimate on the upper limit can be made from the DNL distribution of all channels. The largest observed deviations are approximately 200 mV. This corresponds to an uncertainty of the order of 10 % on the SiPM response. These large values come mainly from one of the 36 channels. In total more than 99 % of the measurements lay between ±100 mV. The majority of the channels shows a peak DNL of approximately 50 mV which is roughly 3 least significant bits (LSB). Next to the DNL which is present over the full range of the DAC some non-linearities at the ends of the DAC range are observed for values lower 5 and above 247.

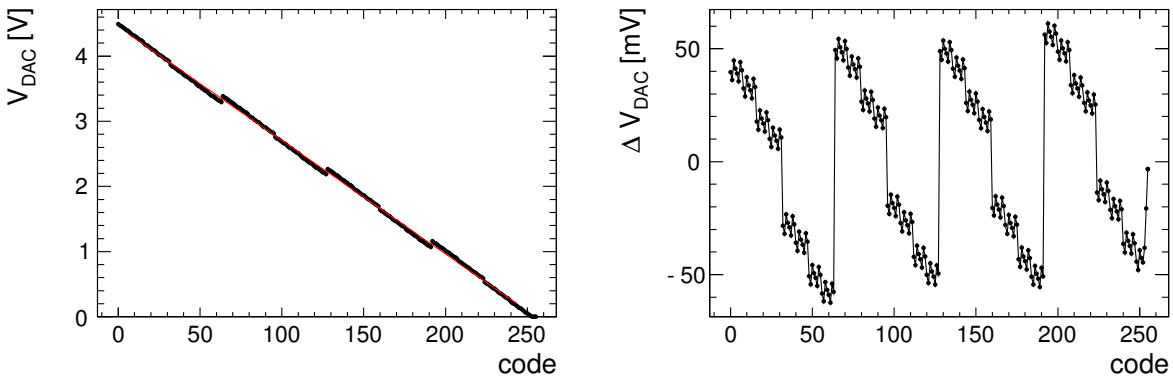

(a) (b)

Figure 12.1: (a) Input DAC performance of SPIROC channel 21. The output voltage V_{DAC} is plotted versus the 8 bit code. The output is fitted with a linear function. (b) The residual ΔV_{DAC} between the actual voltage V_{DAC} and the linear fit.

The form of the DNL is such that the maximum peak to peak difference reaches twice the typical DNL. Such jumps in output voltage are visible in figure 12.1(b) at DAC values of 64, 128, and 192. The position of these jumps is different for the different channels. These differences are the result of a varying size of the least significant bit. Figure 12.3(a) shows the distribution of the LSB size for all SPIROC channels. Significant tails are observed. Two thirds of the measurements lie within (10.9±0.2) mV and (24.3±0.2) mV, which is better than ±1 LSB.

Next to the linearity of the DAC, the adjustable range and the calibration slope s are measured. The DAC can be set with 8 bit accuracy. The calibration slope gives the average value of the least significant bit. A mean slope of (-17.2±0.1) mV/LSB is measured. The values have an RMS of (0.6±0.07) mV/LSB. The slope difference leads to an integral uncertainty of 150 mV at a DAC setting of 250. Without an individual calibration of the DAC, this leads to a spread of the SiPM-tile response of (8±1) % compared to the design value. Figure 12.3(b) displays the distribution.

The adjustable range is measured as the voltage difference between DAC settings of 5 and 247 to avoid the end of range non-linearities. Figure 12.3(c) depicts the results of this measurement. The smallest range is 3.9 V. This is more than 20 % smaller than the design value of 5 V.

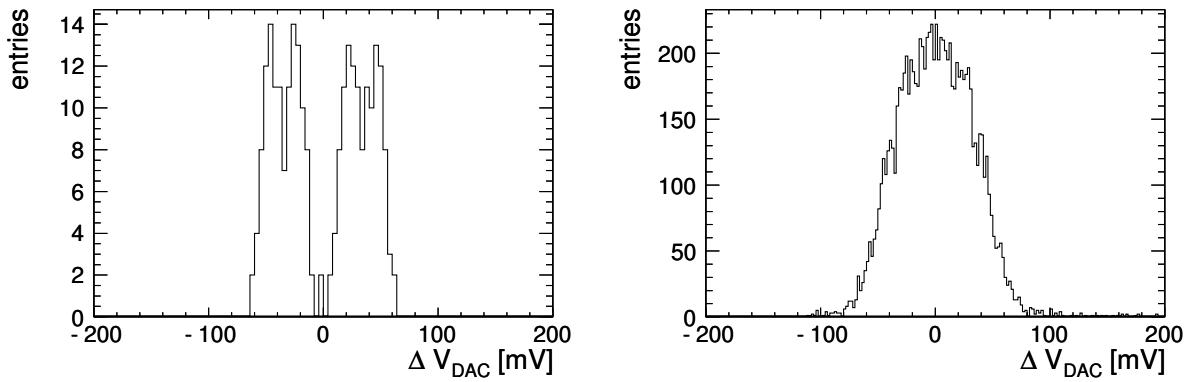

(a) (b)

Figure 12.2: Histogram of the differential non-linearity ΔV_{DAC} of the SPIROC input DAC for: (a) a single channel and (b) all channels.

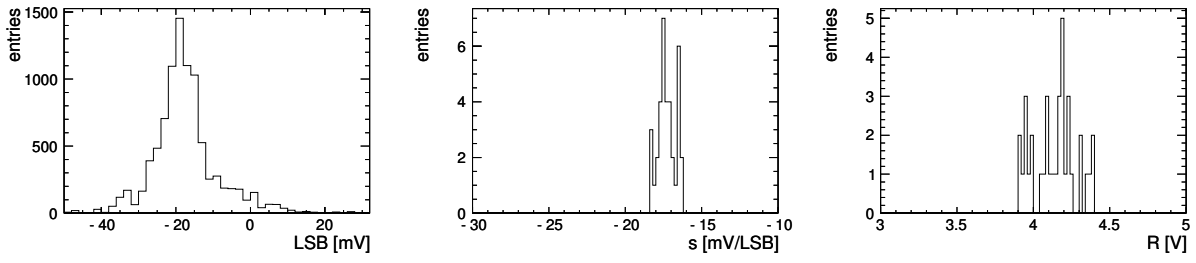

(a) (b) (c)

Figure 12.3: (a) Histogram of the size of the least significant bit. (b) Histogram of the average size of the LSB. (c) Histogram of the DAC range.

12.2 Gain, Linearity, and Hold

The gain of the analogue amplifiers in the SPIROC can be adjusted by changing the size of the feedback capacitance C_{gain}. It is necessary to understand the performance of the chip for the different settings to chose the best operation parameters. This section discusses the measurement of the optimal hold trigger time, the gain of the amplifier, and the achieved linear range.

12.2.1 Hold

The following procedure to measure the hold timing has been established with the predecessor chip FLC-SiPM: The output amplitude is measured for a fixed input charge and different hold times. Stable results were obtained independently of the exact size of the charge. The same procedure is used for the SPIROC. Figure 12.4(a) shows the result for a typical configuration of the high gain path (HG). The same scan for the low gain path (LG) is displayed in figure 12.4(b). The measured value includes delays from the setup cables. A significant difference for the best hold time is observed for the two different amplifier signal paths. Additionally, the results show a dependence on the input charge q, especially for the LG path. This situation is not expected and implies some restrictions on the operation of the SPIROC. A common and fixed hold timing for both signal paths has to be used. This means that one of the two chains cannot be operated at the best hold setting. Additionally, the difference to the best setting will vary with the amplitude.

Operating the SPIROC with an off-peak hold setting leads to an increased sensitivity of the output signal to jitter in the trigger. The jitter transfers to amplitude changes proportional to the slope of the curve. The signal variation can be measured from the recorded curves. An amplitude variation of $(0.75\pm0.01)\,\%$ is found for a 5 ns trigger time shift at the optimal hold setting. The same trigger time variation leads to a $(4.87\pm0.01)\,\%$ amplitude change for a hold which is 15 ns off peak. As the trigger performance with real signals is not yet studied, no number for the influence on the calorimeter resolution can be estimated.

The hold scan result alone is not conclusive. An operation mode has to be found that gives a good enough signal to noise ratio and sufficient linearity. As the HG and LG value do not agree, some choice for the hold has to be made taking into account signal to noise and linearity of the SPIROC.

12.2.2 Gain and Linearity

The gain and the linear range of the amplifier are determined by the choice of the feedback capacitance C_{gain}. While the gain increases with smaller feedback capacitance, the linear range becomes smaller. The combination of the two signal paths allows to achieve a good signal to noise ratio and a large dynamic range at the same time. The gain and linearity are measured to identify the right gain setting for the LG path, to verify that the signal to noise ratio is sufficient, and to check that the HG and the LG range can be matched.

As the hold analysis was inconclusive, the amplifier gain and the linear range is measured for several different hold settings. Practically, this means a scan of the output voltage

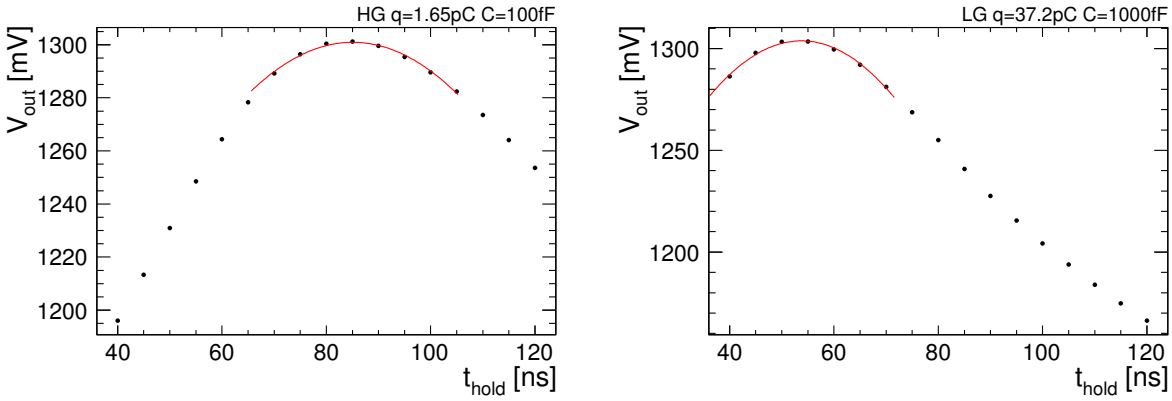

(a) (b)

Figure 12.4: Scan for the best hold value t_{hold} with fixed input charge q. The output amplitude is plotted against the hold time t_{hold}. The red line displays the result of a Gaussian fit to the peak region. (a) Scan of the high gain path with feedback capacitance setting C=100 fF. (b) Scan of the low gain path with feedback capacitance setting C=1000 fF.

V_{out} versus input charge q_{in}, hold time t_{hold}, and feedback capacitance C_{gain}. The response at fixed C_{gain} and t_{hold} is fitted with a linear function. Figure 12.5(a) shows the measurement and the fit for the HG path. The fit range is chosen such that it stops before the onset of the amplifier saturation. The lower plot shows the residual Δ to the linear fit. The linear range is defined by the maximum input charge which shows a residual less than 1 %. The LG path shows an unexpectedly strong non-linearity at low input charges. The fit range is chosen such that it starts after this effect. Figure 12.5(b) shows an example of the LG path measurement.

The measured amplification g of the SPIROC is displayed in figure 12.6. The highest amplification of (116.26±0.03) mV/pC is reached in the high gain path with C_{gain}=100 fF and hold t_{hold}=95 ns. The amplitude dependent hold values are also visible in this measurement. For lower feedback capacitances, the highest gain is measured for earlier hold times.

The residual is displayed in figure 12.7. The optimal hold for the high gain and the low gain path are indicated in the plots, to help the discussion of the operation parameter selection. Also the signal charges of a MIP and a fully saturated SiPM with a gain of one million electrons per pixel are indicated. To achieve the best signal to noise ratio, the smallest gain capacitance is chosen for the high gain path. This results in a linear range of approximately 7.5 pC at the optimal hold of 95 ns. If the hold of the low gain path is chosen, the linear range gets slightly smaller to approximately 7 pC. The results for the low gain path are presented for two different feedback capacitances: C_{gain}=1000 fF and C_{gain}=1300 fF. The first shows a sufficient linear range to cover a fully saturated SiPM with a hold setting of 95 ns. The second can cover the same range with the hold setting of 80 ns optimised for the low gain path. The gain of the LG path is (5.6409±0.0002) mV/pC for C_{gain}=1000 fF and t_{hold}=95 ns, and (4.9075±0.0001) mV/pC for C_{gain}=1300 fF and t_{hold}=80 ns.

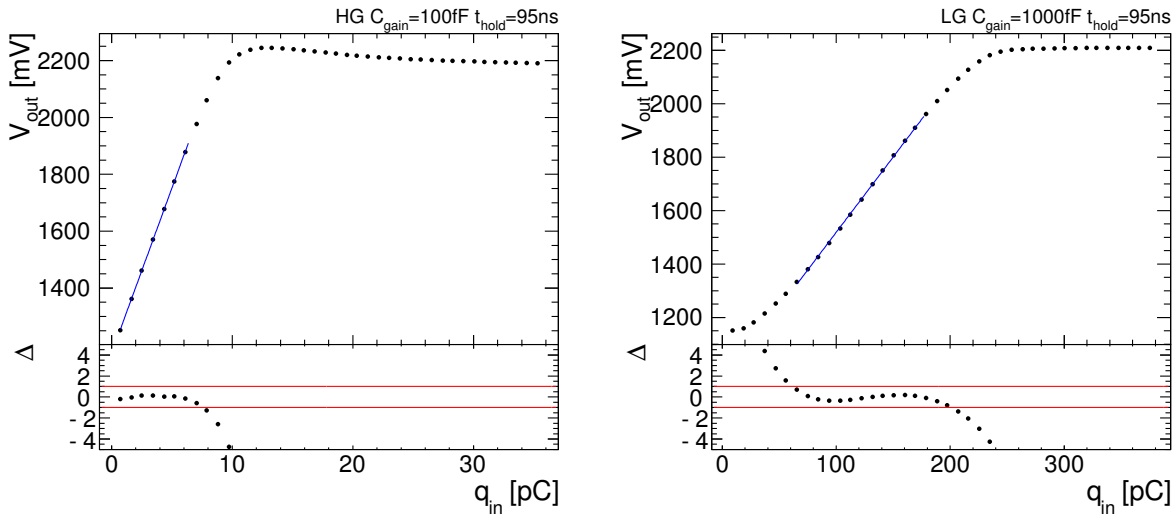

(a) (b)

Figure 12.5: Measurement of the SPIROC response. The output voltage V_{out} is plotted versus the input charge q_{in}. The blue line shows the result of the linear fit. The lower plot shows the residual Δ to the fit. The red lines indicate the end of the linear region. (a) Measurement of the high gain path with feedback capacitance setting C_{gain}=100 fF and hold t_{hold}=95 ns. (b) Measurement of the low gain path with feedback capacitance setting C_{gain}=1000 fF and hold t_{hold}=95 ns.

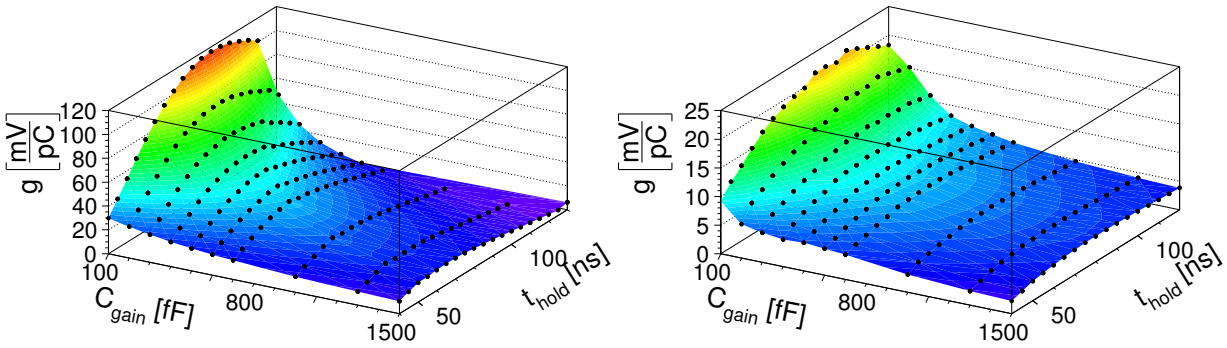

(a) (b)

Figure 12.6: The SPIROC gain g is plotted versus feedback capacity C_{gain} and hold t_{hold}. (a) Results for the high gain path. (b) Results for the low gain path.

The linear range of the high gain path ends before the linear range of the low gain path starts for the presented operation settings. It would be necessary to reduce the gain in the high gain path to achieve a linear matching of the two amplifier chains. The issue of this non-linearity was presented to the designer of the chip and a fix is suggested. Tests show that the non-linearity is significantly reduced. A full qualification measurement is pending. Here, it is assumed that the issue can be fixed and the non-linearity at low input values can be ignored.

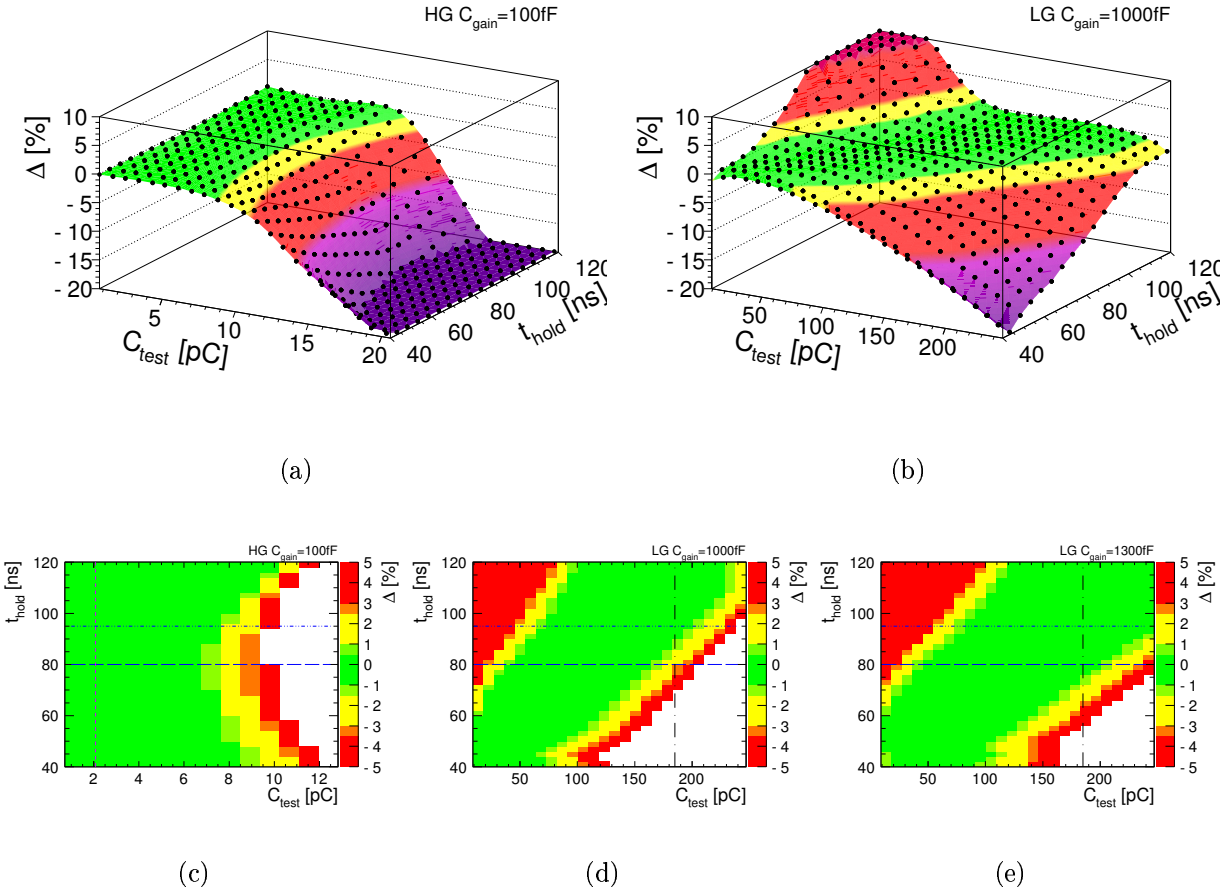

Figure 12.7: Residual versus input charge q_{in} and hold t_{hold}. Following colour scheme is used: Residuals up to ±1 % are coloured green; residuals in the range 1 % to 3 % are coloured yellow; residuals between 3 % and 10 % are coloured red; larger residuals are coloured violet.
(a) Three dimensional view for high gain path and C_{gain}=100 fF.
(b) Three dimensional view for low gain path and C_{gain}=1000 fF.
(c) Two dimensional view of the residual for the high gain path and C_{gain}=100 fF. The size of the residual is indicated with colours for the range of ±5 %. The blue dash-dotted line indicates the optimal hold for the high gain path. The blue broken line indicates the optimal hold for the low gain path. The vertical dashed line indicates the charge of 1 MIP for a SiPM with a gain of 10^6.
(d) Same as (c), but for the low gain path and C_{gain}=1000 fF. The vertical black dash-dotted line indicates the charge of a fully saturated SiPM with a gain of 10^6.
(e) Same as (d) but for C_{gain}=1300 fF.

12.3 Noise

The noise of a measurement setup can be influenced by many sources. Especially, if several devices with their own power supplies are used. The setup was tested for noise sources. Following sources have been identified:

- USB connection to the SPIROC test board.
- Trigger signal for the track and hold stage.
- Clock for the test-board micro controller.

The USB line can be disconnected and the micro controller clock can be disabled without influencing the operation of the SPIROC. But the SPIROC noise can be different with and without hold. There is no way to disentangle a noise increase from a change in bandwidth inside the SPIROC and external noise coupled into the system by the track and hold trigger. The noise measurement is performed without the track and hold trigger, as it is assumed that the external noise dominates. But, it has to be kept in mind that the measured value is a lower limit rather than the real noise of the SPIROC.

The noise is measured for the two signal paths and for different feedback capacitor settings C_{gain}. The measured signal follows a Gaussian distribution, therefore the width σ_{total} is calculated as the root mean square. The measured value contains both the noise of the SPIROC σ_{SPIROC} and the noise of the setup σ_{setup}. As both follow a Gaussian contribution and are uncorrelated, the total noise is given by equation 12.1. Accordingly, the SPIROC noise can be calculated by:

$$\sigma^2_{\text{total}} = \sigma^2_{\text{setup}} + \sigma^2_{\text{SPIROC}} \tag{12.1}$$

$$\sigma_{\text{SPIROC}} = \sqrt{\sigma^2_{\text{total}} - \sigma^2_{\text{setup}}}. \tag{12.2}$$

Error propagation leads to following error $\delta_{\sigma_{\text{SPIROC}}}$:

$$\delta_{\sigma_{\text{SPIROC}}} = \frac{1}{\sigma_{\text{SPIROC}}} \cdot \sqrt{\sigma^2_{\text{total}} \cdot \delta^2_{\sigma_{\text{total}}} + \sigma^2_{\text{setup}} \cdot \delta^2_{\sigma_{\text{setup}}}}. \tag{12.3}$$

The result of the noise measurement is displayed in figure 12.8(a). The strong dependence of the HG noise on the gain capacitance shows that the HG noise is dominated by noise in the input stage. The LG path shows a much smaller dependence on the amplification, which indicates that the noise is dominated by the shaper stage of the SPIROC. The setup noise, indicated as dashed blue line, is small enough to allow an accurate measurement. The noise at the highest gain setting is (1.251±0.008) mV. The two previously discussed SPIROC LG settings of C_{gain}=1000 fF and C_{gain}=1300 fF show a noise of (0.239±0.02) mV and (0.237±0.02) mV. The equivalent noise charge (ENC) is (10.76±0.07) fC for the highest SPIROC gain. The ENC for the low gain path with C_{gain}=1000 fF is (42.4±4) fC and with C_{gain}=1300 fF it is (48.3±0.04) fC.

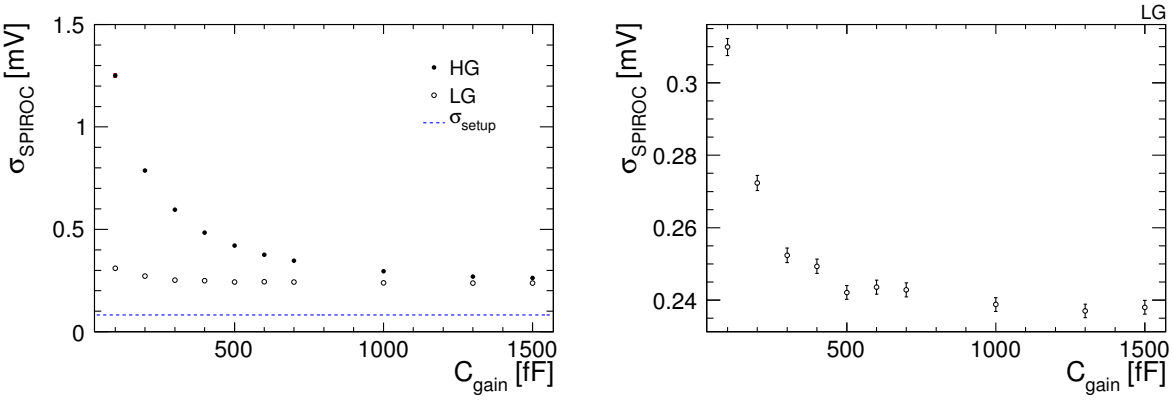

(a) (b)

Figure 12.8: (a) The SPIROC noise σ_{SPIROC} is plotted versus the gain capacitance C_{gain}. Open circles are the noise in the low gain chain of the SPIROC. Full circles are the noise in the high gain chain of the SPIROC. The noise level of the measurement setup is indicated as dashed blue line. (b) Zoom to the range of the low gain path noise.

12.4 Conclusions

The first SPIROC prototype suffers from a bug in the slow control of the chip. Several functionalities are not operational. Nevertheless, it is possible to do basic characterisation measurements of the analog amplifier chains.

The results for the SPIROC input DAC show some deficiencies compared to the design goal. The dynamic range is with 3.9 V approximately 20% smaller than the design range of 5 V. Also the differential non-linearity (DNL) and the integral non-linearity (INL) are larger than expected. The DNL has a mean variation of (31.9±0.2) mV with peak values up to 200 mV. The INL reaches up to 150 mV at the end of the DAC range. To achieve a 1 % SiPM response accuracy, DNL and INL are required to be smaller than 15 mV. With the current performance the uncertainties will be of the order of 10 %.

The response measurement showed an amplitude dependent hold value which is different for the high and low gain amplifier chain. As only one hold value can be selected, this implies that one of the two chains has to be run with an off peak hold setting. This introduces an increased sensitivity to trigger time fluctuations. The effect of a 5 ns jitter is more than 6 times stronger at the necessary shift of 15 ns. Before final conclusions can be drawn, the performance of the SPIROC trigger has to be evaluated.

The response measurements show a non-linearity at low amplitudes in the low gain path. It is assumed that this problem can be fixed in future versions of the SPIROC. Otherwise there is no possibility to run at the highest gain and match low and high gain path linearly. For the further discussions this non-linearity is neglected.

The best possible signal to noise ratio is achieved in the high gain path and with the highest gain setting. The equivalent noise charge is (10.76±0.07) fC which corresponds to a theoretical signal to noise ratio of 7.45±0.05 for a SiPM with a typical gain of 0.5 Me. This

measurement was performed without the trigger and hold stage, to avoid pickup noise. Therefore, this value has to be considered a best possible value and is likely to reduce when the SiPM is operated with signals. Therefore, a selection of a mode with smaller gain seems not advisable. Accordingly this mode is selected for the high gain path. This fixes also the hold to the optimum of the high gain path, as an off peak running could deteriorate the noise performance.

The experience with the AHCAL shows that the SiPM gain has a maximum around 0.5 Me, but values up to 1 Me are easily reached. To fit the signal of SiPMs with 1 Me gain into the linear range, a gain capacitance in the low gain path of 1000 fF or higher has to be chosen. The value is influenced by the off peak hold selection. With the optimal hold range a feedback capacitance of 1300 fF would be necessary.

Summarised, the suggested operation mode for SiPMs similar to the ones used in the AHCAL is: C_{HG}=100 fF and C_{LG}=1000 fF. The hold should be optimised for the high gain path. The measurements suggest a sufficient noise performance, but the values have to be confirmed in a more realistic operation mode of the SPIROC, especially as the hold cannot be optimised for both signal paths at the same time.

Summary and Conclusions

This work combines the development of the calorimeter technology for the planned International Linear Collider, the operation of a prototype calorimeter in a test-beam environment, the study of new hadron shower reconstruction methods, and the validation of different hadron shower simulations.

The Analogue Hadron Calorimeter Technology

The Analogue Hadron Calorimeter prototype (AHCAL) is a highly granular steel-scintillator sandwich calorimeter. It is equipped with small plastic scintillator tiles with sizes down to $3{\times}3\,\mathrm{cm}^2$. The photo-sensor is already integrated into the scintillator tiles. This is possible due to the use of the silicon photomultiplier (SiPM) technology. This work outlined the working principle of these sensors and their application in a calorimeter. A detailed description of the SiPM specific calibration procedure was given and the systematic calibration uncertainty has been derived.

The technological studies also included the characterisation of the readout electronics for a future analogue hadron calorimeter prototype. A test-bench setup for the characterisation of readout chips has been built. The setup was used to study the first prototype of a new readout chip for SiPMs (SPIROC). This chip integrates full signal processing from amplification to digitisation. Despite several problems with the slow control of the chip, it was possible to characterise the performance of the analogue part. The gain, linearity and noise performance of the chip were measured for both the low and the high gain signal chain. Also the performance of integrated SiPM operation voltage adjustment was analysed. The studies showed an unexpected non-linearity at low signals and a different peaking time in the two different signal chains of the chip. This issues were communicated to the designer and a fix in a future prototype is expected.

The currently achievable performance of the chip has been discussed assuming an operation with SiPMs similar to the ones used in the AHCAL. It was found that without a fix for the non-linearity it is not possible obtain the necessary linearity over the full dynamic range. Assuming a fix of the non-linearity, it is possible to find an operation parameter setting that guaranties an amplifier linearity better than 1 %. But, the mismatch of the two peaking times gives a factor 6 increase in timing jitter sensitivity for large signals. Further studies have to show if this results in a relevant degradation of the chip performance. The bare amplifier noise has been measured and a theoretical signal to noise ratio of $7.45{\pm}0.05$ seems achievable with a typical AHCAL SiPM. The SiPM operation voltage adjustment

showed larger differential and integral nonlinearities than expected. With the current performance the SiPM operation parameters can be set with an accuracy of approximately 10 %. Also the adjustable range was found to be 20 % smaller than the design value.

Meanwhile, a second SPIROC prototype has been produced and includes fixes that allow to also test the digital part of the chip. This prototype currently undergoes extensive tests. A third prototype is under development and should fix some of the problems identified by this study.

Hadron Shower Measurements

A comprehensive set of data has been collected with the AHCAL at the CERN hadron beam line. This work described the experimental setup at the test-beam including aspects of beam generation and quality. For the analysis of hadron showers, it is necessary to purify the event sample. This text outlined the event selection with the help of a threshold Cherenkov counter, a particle multiplicity counter, and calorimeter based event selections. The calibration of the particle multiplicity measurement has been described in detail. A comprehensive study of possible systematic dependencies showed that a maximum systematic uncertainty of 2 % can be reached when a run-wise calibration is used. Additionally, a method to identify muons by their geometrical signal distribution in the Tail Catcher and Muon Tracker (TCMT) has been developed. It could be verified that this method reaches a superior purity (>98%) and better energy stability compared to an energy and number of hit based cut.

The high granularity of the AHCAL allows to use new reconstruction methods. One example is the cluster based method to identify the position of the first hard interaction inside a hadron shower, which has been developed during these studies. The text describes the working principle and the optimisation of the algorithm. The method has been tested with different hadron shower simulation models, and a typical position resolution of 3.5 cm has been achieved. This corresponds to approximately the distance between two consecutive AHCAL layers. This newly developed algorithm is the basis for a measurement of hadron showers without the position fluctuations in the first interaction.

The AHCAL uses readout cells of three different sizes. To avoid artifacts from the cell geometry in the hadron shower profiles, a proper assignment of the cell energies to the spatial position is necessary. This becomes especially important if the impact angle of the particles is not perpendicular to the calorimeter front face. A technique has been developed to measure two dimensional shower profiles for arbitrary impact angles. This technique also offers a direct way to normalise the hadron shower profiles measured from the first hard interaction to the varying detector acceptance.

The knowledge about the position of the first hard interaction offers the possibility to correct the detector response for longitudinal leakage on an event by event basis. The maximum achievable improvement in linearity and resolution has been tested. It was found that the detector linearity can be improved from 5 % to 1 %. At the same time, the detector resolution was improved. The gain on resolution scales with the energy and reaches a relative improvement of more than 10 % at 80 GeV pion energy.

As the calorimeter depth is limited by costs, the leakage correction will be an important tool to improve the detector resolution. Studies are ongoing to further improve the leakage

correction. First promising results have been obtained, if in addition to the shower starting point also the shower shape is considered.

Validation of Simulation Models

The high granularity of the AHCAL makes it possible to record hadron showers with unprecedented details. This offers new possibilities to evaluate the performance of different simulation models for hadronic interactions. The existing Geant4 based simulation of the test-beam setup has been revised to reduce systematic uncertainties in the simulations. A more realistic description of the AHCAL material budget and the particle beam could be achieved. The simulation of detector effects and the assumptions on the reconstruction uncertainties have been verified with electromagnetic showers.

The differences between the various hadron shower models implement in Geant4 were outlined. A systematic confrontation of the predictions from different Geant4 physics lists with the test-beam measurements has been performed. The leakage corrected detector response and the two dimensional shower profiles proved as excellent differentiators in these tests.

None of the studied physics lists could fully describe the data within the systematic uncertainties. Significant deviations between simulation and measurements are observed in the shower maximum, especially for energies larger than 20 GeV. Also performance differences between the various list have been observed. While the Quark-Gluon-String (QGS) model based physics lists and the Fritiof (FTF) model based physics lists could give a reasonable description of the experiment in most aspects, the parametrised (LHEP) and Chiral Invariant Phase Space (CHIPS) physics lists showed substantial deficiencies. The agreement between data and simulation for FTF and QGS is sufficient for the ILD detector studies, but it is expected that the simulations can be further improved with the help of the CALICE test-beam data.

Outlook

The AHCAL detector development and test-beam studies are continuing. Currently, AHCAL data taken at the Fermilab meson test-beam are analysed and will extend the energy range to lower values. Additionally, the current AHCAL prototype will be modified to measure hadron showers in a tungsten absorber. Finally, the new AHCAL prototype with SPIROC readout will allow to measure the time development of hadron showers and the shower development inside a magnetic field.

The AHCAL studies will be complemented by the studies with the other CALICE hadron calorimeters. Several digital and semi-digital hadron calorimeter prototypes are currently under construction. Test-beams of similar scales are foreseen and will allow to compare gaseous readouts with scintillator readout.

List of Tables

List of Figures

Bibliography

[1] J. J. Thomson, *Carriers of Negative Electricity* (1906), http://nobelprize.org/nobel_prizes/physics/laureates/1906/thomson-lecture.html. 1

[2] E. Rutherford, *The scattering of α and β particles by matter and the structure of the atom*, Phil. Mag. **21**(1911) 669. 1

[3] Particle Data Group Collaboration, C. Amsler *et al.*, *Review of particle physics*, Phys. Lett. **B667**(2008) 1, and 2009 partial update for the 2010 edition. 2, 10, 11, 16, 52, 147

[4] N. Wattimena, *Calorimetry at the International Linear Collider: From simulation to reality*, Ph.D. thesis, Universität Hamburg, 2010, DESY-THESIS-2010-006. 2, 147

[5] N. Jarosik *et al.*, *Seven-Year Wilkinson Microwave Anisotropy Probe (WMAP) Observations: Sky Maps, Systematic Errors, and Basic Results* (2010), 1001.4744. 2

[6] J. Brau, (ed.) *et al.*, *International Linear Collider reference design report. 1: Executive summary. 2: Physics at the ILC. 3: Accelerator. 4: Detectors* (2007), ILC-REPORT-2007-001. 6, 147

[7] LDC Working Group Collaboration, D. Kisielewska *et al.*, *Detector Outline Document for the Large Detector Concept* (2006), http://www.ilcldc.org/documents/dod/. 7

[8] GLD Concept Study Group Collaboration, K. Abe *et al.*, *GLD detector outline document* (2006), physics/0607154. 7

[9] *IDAG Report on the Validation of Letters of Intent for ILC detectors*, 16. August 2009, http://ilcdoc.linearcollider.org/record/23970/files/IDAG_report_090816.pdf. 7

[10] ILD Concept Group - Linear Collider Collaboration, T. Abe *et al.*, *The International Large Detector: Letter of Intent* (2010), 1006.3396. 8

[11] SiD Collaboration, H. Aihara *et al.*, *SiD Letter of Intent* SLAC-R-944. 8

[12] M. Tantawy, M. El Mashad, S. Gamiel, and M. S. El-Nagdy, *Multiplicity distribution of heavy particles for hadron nucleus interactions*, Chaos Solitons Fractals **13**(2002) 919. 12

[13] C. Leroy and P. Rancoita, *Physics of cascading shower generation and propagation in matter: Principles of high-energy, ultrahigh-energy and compensating calorimetry*, Rept. Prog. Phys. **63**(2000) 505. 14

[14] R. Wigmans, *Calorimetry Energy Measurement in Particle Physics*, Oxford University Press, 2000, ISBN 0-19-850296-6. 14

[15] R. K. Bock, T. Hansl-Kozanecka, and T. P. Shah, *Parametrization of the Longitudinal Development of Hadronic Showers in Sampling Calorimeters*, Nucl. Instr. Meth. **186**(1981) 533. 16

[16] D. Beznosko, G. Blazey, A. Dyshkant, and V. Rykalin, *Effects of the 9-T magnetic field on MRS photodiode* (2005), FERMILAB-PUB-05-410. 17

[17] E. Garutti, M. Groll, A. Karakash, and S. Reiche, *Magnetic field dependence studies for silicon photomultiplier* (2004), LC-DET-2004-025. 17

[18] P. Buzhan *et al.*, *An advanced study of silicon photomultiplier*, ICFA Instrum. Bull. **23**(2001) 28. 20, 21

[19] Hamamatsu Photonics K.K., Solid State Devision, *MPPC Multi-Pixel Photon Counter*, April 2010, http://sales.hamamatsu.com/assets/pdf/catsandguides/mppc_kapd0002e07.pdf. 21

[20] N. Feege, *private communications*. 21

[21] D. Renker and E. Lorenz, *Advances in solid state photon detectors*, JINST **4**(2009) P04004. 21

[22] CALICE Collaboration, M. Danilov, *Scintillator tile hadron calorimeter with novel SiPM readout*, Nucl. Instrum. Meth. **A582**(2007) 451, 0704.3514. 21

[23] C. Adloff *et al.*, *Construction and Commissioning of the CALICE Analog Hadron Calorimeter Prototype*, JINST **5**(2010) P05004, 1003.2662. 25

[24] N. Meyer, *Absorber Thickness in the CALICE HCal Stack*, CALICE Internal Note **016**(2009). 25

[25] B. Lutz, *Commissioning of the readout electronics for the prototypes of a hadronic calorimeter and a tailcatcher and muon tracker*, Diplomarbeit, Universität Hamburg, May 2006, ISSN 1435-8085. 27, 29, 119

[26] N. Wattimena, *Comissioning of an LED Calibration & Monitoring System for the Prototype of a Hadronic Calorimter*, Diplomarbeit, Universität Hamburg, April 2006, ISSN 1435-8085. 27

[27] N. Feege, *Silicon photomultipliers: Properties and application in a highly granular calorimeter*, Diplomarbeit, Universität Hamburg, October 2008, ISSN 1435-8085. 30, 31, 36, 119, 129

[28] B. Bulanek, *Analysis of the CALICE AHCAL MIP calibration*, diploma thesis – in preparation, Charles Univesity in Prag – Institute of Particle and Nuclear Physics, April 2010. 35, 36

[29] CALICE Collaboration, J. Repond *et al.*, *Design and Electronics Commissioning of the Physics Prototype of a Si-W Electromagnetic Calorimeter for the International Linear Collider*, JINST **3**(2008) P08001, 0805.4833. 42

[30] C. Adloff *et al.*, *Study of the interactions of pions in the CALICE silicon-tungsten calorimeter prototype* (2010), 1004.4996. 42

[31] J. Spanggaard, *Delay Wire Chambers – A Users Guide* (1998), sl.web.cern.ch/SL/Publications/bi98-023.pdf. 44

[32] M. F. Gianelly, *Measuring the Higgs self-coupling at an electron-positron collider*, Ph.D. thesis, Royal Holloway University of London, November 2008, https://www.pp.rhul.ac.uk/twiki/pub/Public/GroupPublications/MFG_PHD_Thesis.pdf. 44

[33] L. Gatigon, *Some Information on Threshold Cerenkovs*, 15. November 1996, http://ab-div-atb-ea.web.cern.ch/ab-div-atb-ea/documentation/eqpmts/XCETinfo.html. 45

[34] H. W. Atherton *et al.*, *Precise Measurements of Particle Production by 400-GeV/c Protons on Beryllium Targets* (1980), CERN-80-07. 46

[35] *Short Introduction to the use of the H6 beam*, 2. May 2000, http://ab-div-atb-ea.web.cern.ch/ab-div-atb-ea/BeamsAndAreas/h6/H6manual.pdf. 47

[36] GEANT4 Collaboration, S. Agostinelli *et al.*, *GEANT4: A simulation toolkit*, Nucl. Instrum. Meth. **A506**(2003) 250. 49

[37] J. Allison *et al.*, *Geant4 developments and applications*, IEEE Trans. Nucl. Sci. **53**(2006) 270. 49

[38] P. Mora de Freitas and H. Videau, *Detector simulation with MOKKA / GEANT4: Present and future* (2002), Prepared for International Workshop on Linear Colliders (LCWS 2002), Jeju Island, Korea, 26-30 Aug 2002. 49, 56

[39] *Mokka homepage*, http://polzope.in2p3.fr:8081/MOKKA/. 49, 56

[40] H. Fesefeldt, *The Simulation of Hadronic Showers: Physics and Applications* (1985), PITHA-85-02. 50

[41] B. Andersson, G. Gustafson, and B. Nilsson-Almqvist, *A Model for Low-p_T Hadronic Reactions, with Generalizations to Hadron - Nucleus and Nucleus-Nucleus Collisions*, Nucl. Phys. **B281**(1987) 289. 50

[42] B. Andersson, *THE FRITIOF DYNAMICS* (1987), Prepared for Shandong Workshop on Multiparticle Production, Jinan, Shandong, China, 28 Jun - 6 Jul 1987. 50

[43] G. Folger and J. P. Wellisch, *String parton models in Geant4* (2003), nucl-th/0306007. 50

[44] *Geant4 Physics Reference Manual*, http://cern.ch/geant4/UserDocumentation/UsersGuides/PhysicsReferenceManual/fo/PhysicsReferenceManual.pdf. 50, 52

[45] A. B. Kaidalov and K. A. Ter-Martirosian, *Pomeron as Quark-Gluon Strings and Multiple Hadron Production at SPS Collider Energies*, Phys. Lett. **B117**(1982) 247. 50

[46] A. Heikkinen, N. Stepanov, and J. P. Wellisch, *Bertini intra-nuclear cascade implementation in Geant4* (2003), nucl-th/0306008. 51

[47] G. Folger, V. N. Ivanchenko, and J. P. Wellisch, *The Binary Cascade*, Eur. Phys. J. **A21**(2004) 407. 52

[48] P. V. Degtyarenko, M. V. Kosov, and H. P. Wellisch, *Chiral invariant phase space event generator. I: Nucleon antinucleon annihilation at rest*, Eur. Phys. J. **A8**(2000) 217. 52

[49] P. V. Degtyarenko, M. V. Kossov, and H. P. Wellisch, *Chiral invariant phase space event generator. II: Nuclear pion capture at rest and photonuclear reactions below the Δ(3,3) resonance*, Eur. Phys. J. **A9**(2000) 411. 52

[50] P. V. Degtyarenko, M. V. Kossov, and H. P. Wellisch, *Chiral invariant phase space event generator. III: Modeling of real and virtual photon interactions with nuclei below pion production threshold*, Eur. Phys. J. **A9**(2000) 421. 52

[51] J. Apostolakis, *et al.*, *GEANT4 Physics Lists for HEP*, in *Nuclear Science Symposium Conference Record, 2008. NSS '08. IEEE*, ISSN 1082-3654, 19-25 2008 833 –836. 52

[52] A. I. Lucaci-Timoce, *Transverse Profiles Analysis – Update –*, 7. December 2009, CALICE Analysis Meeting, http://ilcagenda.linearcollider.org/materialDisplay.py?contribId=9&materialId=slides&confId=4284. 55

[53] A. I. Lucaci-Timoce, *Transverse Profiles in Electromagnetic Showers with the CALICE AHCAL*, March 2010, CALICE Week at UT Arlington, http://ilcagenda.linearcollider.org/materialDisplay.py?contribId=9&sessionId=2&materialId=slides&confId=4391. 55

[54] A. I. Lucaci-Timoce, *Description of the Analog HCAL Prototype in Mokka* (2009), http://www.desy.de/~lucaci/Others/hcalTBeam.pdf. 56

[55] J. B. Birks, *The Theory and practice of scintillation counting* (1964), International series of Monographs on Electronics and Instrumentation, v. 27 Macmillan, New York. 57

[56] A. Nassalski, M. Moszynski, A. Syntfeld-Kazuch, T. Swiderski, and T. Szczeniak, *Non-Proportionality of Organic Scintillators and BGO*, Nuclear Science, IEEE Transactions on **55**(2008)(3) 1069 , ISSN 0018-9499. 57

[57] R. Brun and F. Rademakers, *ROOT – An object oriented data analysis framework*, Nuclear Instruments and Methods in Physics Research Section A: Accelerators, Spectrometers, Detectors and Associated Equipment

389(1997)(1-2) 81 , ISSN 0168-9002, New Computing Techniques in Physics Research V, http://www.sciencedirect.com/science/article/B6TJM-3SPKX96-1F/2/3aa2b2cb72c9a4316a842802541bf317. 69

[58] F. James and M. Roos, *Minuit: A System for Function Minimization and Analysis of the Parameter Errors and Correlations*, Comput. Phys. Commun. **10**(1975) 343. 69

[59] *Marlin Util – Marlin package with commonly used classes and functions*, February 2010, Version 00-14-01, http://ilcsoft.desy.de/portal/software_packages/marlinutil/. 74

[60] I. Marchesini, *A Simultaneous Measurement of TGCs and Beam Polarization at the ILC and a Study on Leakage and Energy Resolution Using the CALICE AHCAL Prototype*, Ph.D. thesis, University Hamburg, in preparation. 90

[61] A. I. Lucaci-Timoce, *private communications*. 111

[62] L. Raux, *SPIROC (SiPM Integrated Read Out Chip): Dedicated very front-end electronics for an ILC prototype hadronic calorimeter with SiPM readout* (2007), Prepared for Topical Workshop on Electronics for Particle Physics (TWEPP 07), Prague, Czech Republic, 3-7 Sep 2007. 115

[63] L. Raux, *et al.*, *DRAFT: H-Cal SiPM ASIC WORKING DOCUMENT*, IN2P3-CNRS - Université Paris-Sud, 28. March 2006, www.lal.in2p3.fr. 115

[64] R. Fabbri, B. Lutz, and W. Shen, *Overview of Studies on the SPIROC Chip Characterisation* (2009), 0911.1566. 118

[65] M. Groll, *Construction and commissioning of a hadronic test-beam calorimeter to validate the particle-flow concept at the ILC*, Ph.D. thesis, Universität Hamburg, 2007, DESY-THESIS-2007-018. 119

[66] Stanford Research Systems, Inc., *datasheet for DG535*, 2006, http://www.thinksrs.com/products/DG535.htm. 122

[67] CAEN S.p.A Costruzioni Apparecchiature Elettroniche Nucleari, *datasheet for CAEN V785N*, 2007, http://www.caen.it/nuclear/product.php?mod=V785N#. 123

[68] *222 NIM Dual Gate and Delay Generator*, http://www.lecroy.com/lrs/dsheets/222.htm. 123

[69] CAEN S.p.A Costruzioni Apparecchiature Elettroniche Nucleari, *VME - PCI Optical Link Bridge Manual Rev. 9*, 30. June 2009, http://www.caen.it/nuclear/product.php?mod=V2718&obj=mn&id=2250. 123

[70] Analog Devices, *AD8051/AD8052/AD8054 Rev. J*, July 2009, http://www.analog.com/static/imported-files/data_sheets/AD8051_8052_8054.pdf. 123

[71] Keithley Instruments, Inc., *Model 2001 Multimeter Specifications*, February 2009, http://www.keithley.com/data?asset=5379. 125

[72] P. Eckert, H.-C. Schultz-Coulon, W. Shen, R. Stamen, and A. Tadday, *Characterisation Studies of Silicon Photomultipliers*, Nucl. Instrum. Meth. **A620**(2010) 217, 1003.6071.

[73] A. Vogel, *Beam-induced backgrounds in detectors at the ILC*, Ph.D. thesis, Universität Hamburg, August 2008, DESY-THESIS-2008-036.

[74] L. Hallermann, *Analysis of GEM properties and development of a GEM support structure for the ILD Time Projection Chamber*, Ph.D. thesis, Universität Hamburg, March 2010, DESY-THESIS-2010-015.

[75] H. Spieler, *Semiconductor Detector Systems*, Oxford University Press Inc., 2005, ISBN 0-19-852784-5.

[76] *Memorandum of Agreement between the members of the CALICE Collaboration*, 19. July 2005, http://polywww.in2p3.fr/flc/MOA.pdf.

[77] W. W. M. Allison and P. R. S. Wright, *The Physics of Charged Particle Identification: dE/dx, Cherenkov and Transition Radiation* (1983), OXFORD-NP-35-83.

[78] M. Kossov, *Chiral invariant phase space event generator: Deep inelastic lepto-nucleon reactions*, Eur. Phys. J. **A34**(2007) 283.

[79] F. Gaede, *Marlin and LCCD: Software tools for the ILC*, Nucl. Instrum. Meth. **A559**(2006) 177.

[80] burster, *Hochpräzisions-Kalibrierquelle für Spannung, Strom und Thermoelemente – DIGISTANT Typ 4462*, December 2003.

[81] D. E. Groom, F. James, and R. Cousins, *Probability: in Review of Particle Physics (RPP 2000)*, Eur. Phys. J. **C15**(2000) 191.

[82] V. Andreev *et al.*, *A high granularity scintillator hadronic-calorimeter with SiPM readout for a linear collider detector*, Nucl. Instrum. Meth. **A540**(2005) 368.

[83] B. Dolgoshein *et al.*, *Status Report on Silicon Photomultiplier Development and its Apllications.*

[84] P. Buzhan *et al.*, *Silicon photomultiplier and its possible applications*, Nucl. Instrum. Meth. **A504**(2003) 48.

[85] CALICE Collaboration, P. D. Dauncey, *CALICE electromagnetic calorimeter readout status* (2004), hep-ex/0410001.

[86] CALICE-UK Collaboration, P. D. Dauncey, *Readout electronics for the CALICE ECAL and tile HCAL* (2002), hep-ex/0211052.

Acknowledgements

First I want to thank Prof. Rolf-Dieter Heuer, Prof. Johannes Haller, and Prof. Peter Schleper for the time they spent evaluating my work, especially considering their schedules. Similar credit goes to Dr. Georg Steinbrück for chairing the examinations. I also want to thank my supervisor Dr. Felix Sefkow for the interesting and challenging work, his clear explanations (both of physics and politics), and the creative freedom I enjoyed. To the same extent I want to thank Dr. Erika Garutti who was not only available for physics discussions at any time, but also cared more than anyone else about the well-being of us Ph.D.-students.

Special thanks go to Prof. David Ward and to Dr. Angela Isabella Lucaci-Timoce. Though I wasn't David's student, he was always willing to read and comment my work and I'm grateful for all his advice. I am deeply indebted to Angela for all her tireless assistance with software, no matter which acronym it was carrying. Furthermore, I enjoyed not only her open-hearted nature and her endless patience, but also her being the most reliable colleague I know. I also have to thank Dr. John Apostolakis for his personal introduction to Geant4 and his very valuable hints.

I had the luck to meet and work with many members of the CALICE collaboration. I gained a lot from this work and want to express my gratitude for the good team play not only but especially to Fabrizio, Kurt, Paul, Roman, Satoru, and Vishnu.

There are many more people that contributed to making the time I spent for this work interesting, exciting, and as enjoyable as possible. Firstly, I want to say thank you for the good time to my office colleagues and associated tea addicts: Hendrik, Ivan, Nanda, Niels, Nils, Sebastian and Sebastian. Equal thanks go to all the experts that shared the responsibility for the AHCAL with me: Alex, Karsten, Marius, Nils, and Sven. I also want to thank Christophe, Riccardo, and Stéphane for their dedication in understanding the operation of the SPIROC chip. Additionally, I want to thank Adrian, Christoph, Jörgen, Karsten, Lea, Ralf and Ramona for their many practical tips and Mark for his incredible spell checking capabilities.

Last but not least, I want to thank my family and friends: my parents for their support they provided me through all my life; my brother and his girlfriend for reminding me how German works; Christian, Stellan and Steffi for distracting my mind at least at some weekends; and most of all my girlfriend Olga who patiently supported me through the never ending process of writing.